Titre: Title:	Patterned Porous Carbon for Electrospray Ion Thrusters
Auteur: Author:	Ben George
Date:	2019
Type:	Mémoire ou thèse / Dissertation or Thesis
Référence: Citation:	George, B. (2019). Patterned Porous Carbon for Electrospray Ion Thrusters [Mémoire de maîtrise, Polytechnique Montréal]. PolyPublie. https://publications.polymtl.ca/4055/

POLYTECHNIQUE MONTRÉAL

affiliée à l'Université de Montréal

Patterned Porous Carbon for Electrospray Ion Thrusters

BEN GEORGE

Département de génie chimique

Mémoire présenté en vue de l'obtention du diplôme de *Maîtrise ès sciences appliquées*

Génie chimique

Octobre 2019

POLYTECHNIQUE MONTRÉAL

affiliée à l'Université de Montréal

Ce mémoire intitulé :

Patterned Porous Carbon for Electrospray Ion Thrusters

présenté par **Ben GEORGE**

en vue de l'obtention du diplôme de *Maîtrise ès sciences appliquées*

a été dûment accepté par le jury d'examen constitué de :

Daria Camilla BOFFITO, présidente
Fabio CICOIRA, membre et directeur de recherche
Clara SANTATO, membre et codirectrice de recherche
Giovanni BELTRAME, membre

ACKNOWLEDGEMENTS

The author would like to acknowledge the following persons for their input:

- Prof. Fabio Cicoira and Prof. Giovanni Beltrame for giving the opportunity to work on a fascinating topic, their constant encouragement, access to resources, and patience
- Dr. Sanyasi Rao Bobbara for his friendship, constant encouragement, advice, experience, insight, and hard work without which this project could not have proceeded. His input into the data and attention to detail have been the cornerstone of this project
- M. Steeve Rousselot of Université de Montréal for kindly pyrolyzing our samples and providing us the full facilities of his lab for our needs
- M. Christophe Clement for his friendship, and patient training in the microfabrication facilities and advice in developing procedures
- M. Jean-Sébastien Boisvert for his work in laser-ablating the xerogels
- Dr. Sergiy Patskovsky and Mme. Jennyfer Zapata-Farfan for their training on their laser system and Prof. Michel Meunier for providing access to this
- Mme. Marie-Hélène Bernier for her training in the clean-room and constant encouragement
- Dr. Philippe Plamondon for his time and co-operation in securing the best possible SEM images
- M. Robert Delisle for his kind assistance in creating the (to be used) force sensor
- M. Sebastien Chenard for his kind assistance in sample preparation and input into the project
- M. Daniel Pilon for his co-operation in providing the electrical components
- Summer interns Jeeyeon Yeu and Dhrumil Shah for their hard work with the literature review, generating the CAD drawings, and following up on the force sensor
- Ms. Yuting Ciou for her kind assistance with optical microscopy images

RÉSUMÉ

Les satellites miniatures gagnent en importance dans l'industrie spatiale. L'amélioration des mini-capteurs commerciaux, la diminution des coûts de fabrication et de lancement ainsi que l'apparition de nouvelles méthodes de déploiement ont permis au satellite miniature de réduire les coûts d'applications spatiales longtemps onéreuses. Celui-ci permet notamment de réaliser de la télédétection, de la surveillance météorologique ou encore de l'exploration sans pilote dans l'espace lointain. Cependant, son utilisation est conditionnée à l'apparition de systèmes de propulsions adéquat devant respecter des contraintes dimensionnelles et sécuritaires strictes au milieu spatial. Les systèmes de propulsion à fluide comprimé, comme les fusées et les systèmes à gaz froid, fourniraient une poussée suffisante et ont été miniaturisés avec succès, mais ils ne sont pas en mesure de propulser le satellite miniature pendant toute la durée d'une mission. Les systèmes électriques peuvent eux assurer la propulsion sur toute la durée d'une mission, mais ne fournissent pas une quantité de poussée suffisante. Néanmoins, ces derniers peuvent être miniaturisés et combinés ensemble pour assurer une propulsion du satellite homogène durant une mission prolongée. En utilisant un liquide ionique comme source d'ions, il est possible de développer un système électro-spray ionique compact, dans lequel le liquide est éjecté par le biais de tensions d'accélération élevées émises par un émetteur poreux ou capillaire.

Dans ce travail, le xérogel de carbone a été choisi comme matériau poreux car il est facile à traiter et ses propriétés peuvent être facilement adaptées en modifiant les proportions de réactifs et les conditions de réaction. Le xérogel est macroporeux, avec un réseau de pores en forme de cage, ce qui lui permet facilement d'absorber un liquide ionique. La mise au point de méthodes de microfabrication étaient nécessaires pour créer les émetteurs (de l'ordre du micron) à la surface du xérogel tout en évitant d'endommager les pores du matériau. Une scie à fil diamantée, optimisée pour les matériaux fragiles, a été adaptée pour créer rapidement des piliers émetteurs identiques à la surface du xérogel. D'autres méthodes telles que la gravure ionique réactive au plasma oxygène, l'ablation au laser ou encore l'utilisation d'un moule en élastomère pour pré-mouler le xérogel ont été infructueuses, car elles ont endommagé les pores et/ou laissées des résidus chimiques difficiles à éliminer à la surface du xérogel.

Des tests électriques sur des xérogels ioniques imbibés de liquide ont montré que, pour des conditions ambiantes et des tensions d'accélération comprises entre 250 et 450 V_{DC}, il y production d'electrospray, observée en tant que signaux électriques sur un oscilloscope. En général, une tension d'accélération plus élevée augmente le courant émis. Dans ce mémoire, pour les expériences de longue durée, on remarque qu'à partir d'une tension d'entrée de départ de 250 V_{DC}, les émissions diminuent progressivement dans le temps et la tension d'accélération doit être augmentée (maximum de 450 VDC à condition ambiante) pour maintenir les émissions. La majeure partie du liquide ionique reste dans la matrice de xérogel et ne peut être expulsée que sous des tensions d'accélération encore plus élevées (> 700 V_{DC}) qui peuvent uniquement être obtenues sous vide afin d'éliminer la possibilité d'arc de claquage. Des résidus ont été observés sur les pointes de l'émetteur, et il a été montré qu'ils provenaient de liquides ioniques.

La mise au point d'une méthode de microfabrication rapide, en une seule étape et sans masque, destinée à la micro-configuration de xérogel de carbone est la première étape vers la création d'un système de propulsion par électrospray fonctionnel. La tension d'accélération doit être optimisée à l'aide de la spectrométrie sur la durée de vol afin d'obtenir une émission ionique pure, et aussi le xérogel doit pouvoir être intégré dans un boîtier robuste, avant de pouvoir propulser un satellite miniature.

ABSTRACT

Miniature satellites are gaining importance in the space industry. With the increasing capability of miniaturized commercial-of-the-shelf sensors, low manufacturing and launch costs, and the release of new swarming methodologies, miniature satellites can lower costs for applications like remote sensing, weather monitoring, unmanned deep-space exploration, etc. One handicap to adoption and development has been the lack of propulsion systems, which must align with strict dimensional and safety constraints, and provide thrust for orbital maneuvers and propulsion. Compressed fluid propulsion systems, that include rockets and cold gas systems, provide thrust and have been successfully miniaturized, but are unable to propel the satellite over the entire mission. Electrical systems can provide propulsion over the entire mission duration, but do not provide the same amount of thrust as compressed fluids. However, electrostatic propulsion systems can be miniaturized and multiplexed to provide consistent satellite propulsion over an extended mission lifetime. By using ionic liquid as the ion source, a compact ionic electrospray system, where the liquid is ejected by high accelerating voltages from a porous or capillary emitter, can be developed.

In this work carbon xerogel was chosen as the porous material as it is easy to process and its properties can be easily tailored by altering the reagent proportions and reacting conditions. The xerogel is macro-porous, with a cage-like pore network, which can readily soak up ionic liquid. Microfabrication methods were required to create the micron-sized emitters on the xerogel surface; ideally, these would not damage the pores of the material. An automatic wafer dicing saw, optimized for brittle materials, was adapted to create emitter pillars on the xerogel surface; this did not damage the pores, provided consistent patterns and rapid turnover. Other methods like oxygen-plasma reactive ion etching, laser ablation and using an elastomeric stamp to pre-pattern the xerogel were unsuccessful, as they damaged the pores, or left chemical residues on the xerogel surface which are difficult to eliminate.

Electrical tests with ionic liquid-soaked xerogels in ambient conditions with accelerating voltages varying between 250 and 450 V_{DC} showed that electrospray readily occurs, measured as electrical signals on an oscilloscope. In general, higher accelerating voltage increases the emitted current, as

expected. In this Mémoire, For extended-duration experiments, from a starting input voltage of 250 V_{DC}, the emission gradually drops over time, and the accelerating voltage must be increased (maximum of 450 V_{DC} in ambient air) to maintain emissions; most of the ionic liquid remains in the xerogel matrix and may only be expelled at higher accelerating voltages (>700 V_{DC}), that can only be obtained in a vacuum chamber to eliminate the possibility of air-breakdown arcing. Residues were observed on the emitter tips, these were determined to originate from ionic liquids.

The development of a rapid, single-step, and maskless microfabrication method to micro-pattern carbon xerogels is the first step in the creation of a working electrospray propulsion system. The accelerating voltage must be optimized with the help of time-of-flight spectrometry to achieve pure ion emission, and the xerogel must be integrated into a robust package, before it can provide propulsion to a miniature satellite.

TABLE OF CONTENTS

LIST OF FIGURES

LIST OF SYMBOLS AND ABBREVIATIONS

[EMIM][TFSI] 1-Ethyl-3-methylimidazolium bis(trifluoromethylsulfonyl)imide

EDX Energy-dispersive X-ray spectroscopy

SEM Scanning electron microscope

FEEP Field effect electrospray

CNC computer numerical control

RIE reactive ion etching

DRIE deep reactive ion etching

LABE Low Angle Back-scattered Electron

PDMS Polydimethysiloxane

DC direct current

RF resorcinol-formaldehyde

sccm standard cubic centimeters per minute

MIP mercury intrusion porosimetry

MEMS Micro-Electro-Mechanical Systems

LMF Laboratoire de Microfabrication (at Polytechnique Montreal)

LIST OF APPENDICES

CHAPTER 1 INTRODUCTION

CubeSats are a miniature satellite platform consisting of cubical modules 10 cm per side and a weight of 1.33 kg per module (Figure 1.1, Figure 1.2). With increasing capabilities of miniature commercial of-the-shelf electronics, smaller satellites can perform many functions of larger, more expensive satellites at a fraction of the manufacturing and launching costs. Further, these don't require as stringent safety requirements as conventional satellites, which reduces costs even further [1]. Launch providers have incentivized this development by introducing free or lower cost secondary payload capacity; the National Aeronautics and Space Administration (NASA) and European Space Agency (ESA) now deploy miniature satellites from the International Space Station. Currently, these satellites are used to monitor natural resources and commercial activity. Anticipated applications include remote sensing, precision agriculture, environment damage, weather monitoring, navigation, and communication, which is possible due to the increasing capabilities of miniaturized electronics.

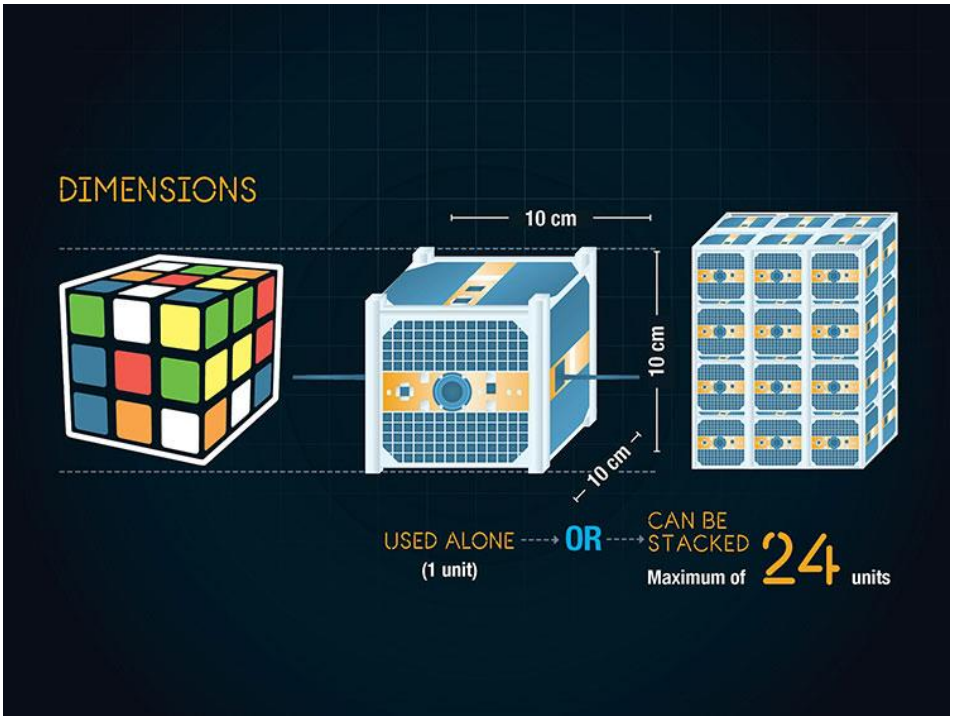

Figure 1.1 CubeSat specifications [2]

In the future, these satellites could reduce the costs associated with near- and deep-space exploration, as increasing autonomous capabilities are developed and incorporated. Future CubeSats will be able to swarm, hence able to combine the functionality of larger satellites with much greater resilience. Swarming technology can be applied to an individual CubeSats to endow them with greater resilience in case of system failure without the need for redundant systems. The success and development of miniature satellites like CubeSats have led to the proposal of a 'ChipSat' which consists of monolithic semiconductor chips between 0.1 g and 100 g, which could be grouped into a highly interactive network which could further replace some larger satellite functionality, while retaining the resilience of a distributed system [1].

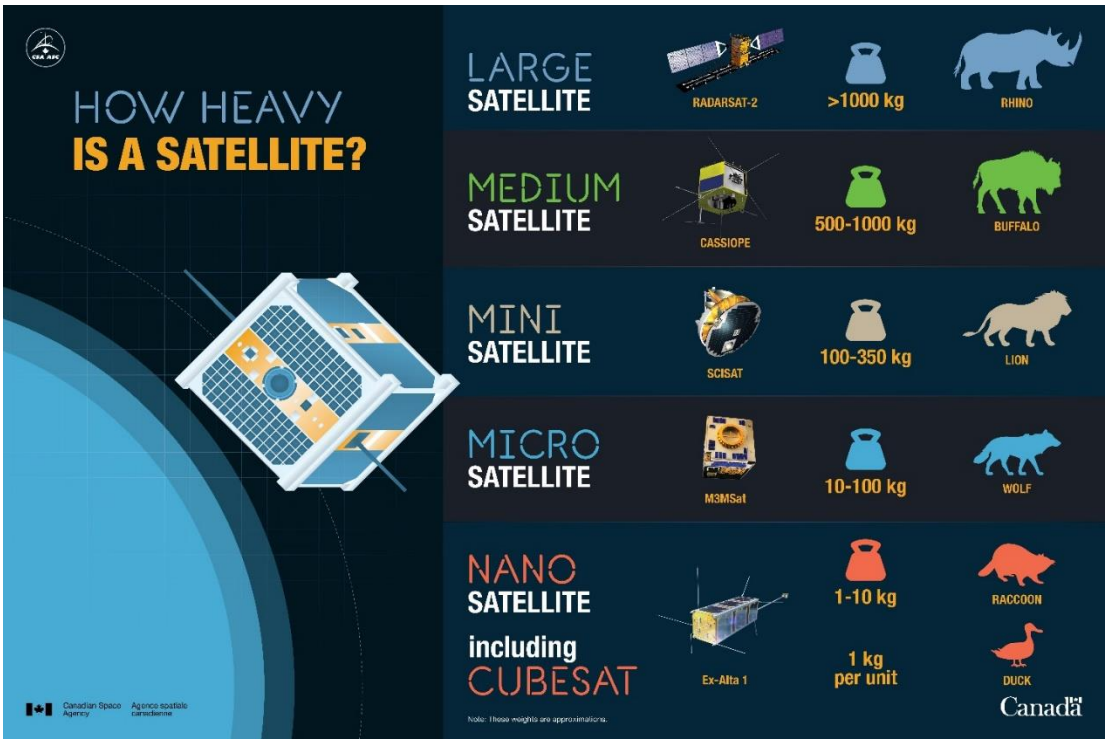

Figure 1.2 Satellite size chart[3]

Challenges to CubeSat development include developing compact power sources, and miniaturized propulsion systems. The latter is more of a challenge because these must provide sufficient thrust over the mission lifetime while also abiding by the safety restrictions imposed by the launch

providers [4]. Propulsion systems serve a variety of roles including orbital altitude change and correction, improving mission lifetimes, de-orbiting, formation flight and constellation formation (important for swarming), and near- and deep-space flight [1], [4].

1.1 Space Propulsion definitions [5]

Thrust is the reaction force where, by Newton's third law, a working fluid accelerating in one direction causes a corresponding acceleration in the opposite direction in the system expelling the working fluid. It is defined by:

$$T = \dot{m}c \tag{1}$$

Where T is the thrust generated by the system, $\dot{m}$ is the mass flow and c is the exhaust velocity. The specific impulse is defined as:

$$I_{sp} = \frac{\int_0^t T dt}{W_p} = \frac{\int_0^t \dot{m} c dt}{g \int_0^t \dot{m} dt} \tag{2}$$

Where W_p is the weight of the propellant. For constant exhaust velocity, we have:

$$I_{sp} = \frac{c}{g} = \frac{T}{\dot{m}g} \tag{3}$$

Specific impulse, I_{sp}, is the thrust generated by a unit of mass flow and is a measure of the total energy of the system and g is the gravitational acceleration. Hence, applying I_{sp} into the rocket equation:

$$\Delta v = c \ln \frac{m_0}{m_f} = I_{sp} g \ln \frac{m_0}{m_f} \tag{4}$$

Where Δv is the change in velocity of the satellite, m_0 is the initial total mass of the satellite including the propellant, and m_f is the final total mass of the satellite after all propellant has been discharged. In this case, the satellite is the CubeSat.

The efficiency, η, of the propulsion system is given by:

$$\eta = \frac{\frac{1}{2}\dot{m}c^2}{P} \tag{5}$$

Where P is the total input power, in the case of chemical propulsion from the energy stored in the reactants, and in the case of electrical propulsion from solar panels.

For constant P and η:

$$T = \frac{2P\eta}{gI_{sp}} \tag{6}$$

Which shows that thrust is inversely proportional to specific impulse for a given power input

1.2 Objectives

This thesis seeks to develop a CubeSat propulsion system that generates thrust for orbital maneuvers over the entire CubeSat mission lifetime. This thesis will contribute to this objective by:

1. Choosing an appropriate propulsion system concept by exploring the miniature satellite state-of-the-art
2. Selecting an appropriate methodology to fabricate propulsion system prototype iterations
3. Performing emission tests on prototypes

CHAPTER 2 LITERATURE REVIEW

2.1 CubeSat Propulsion State of the Art

There are 3 broad categories of miniature-satellite propulsion: compressed fluid, electrical and propellant-less.

2.1.1 Compressed fluid Propulsion

A compressed working fluid accelerates through a converging-diverging nozzle and expands into a lower density exhaust, generating directed kinetic energy. The compressed fluid can be a gas under pressure or be generated through chemical reactions (Figure 2.1). In warm and cold gas propulsion, the propellant is a gas under pressure (Figure 2.1 a, b), in chemical propulsion, the propellant may be gaseous or liquid (Figure 2.1 c, d) or solid (Figure 2.1 e) or a combination of solid and gaseous (Figure 2.1 f)

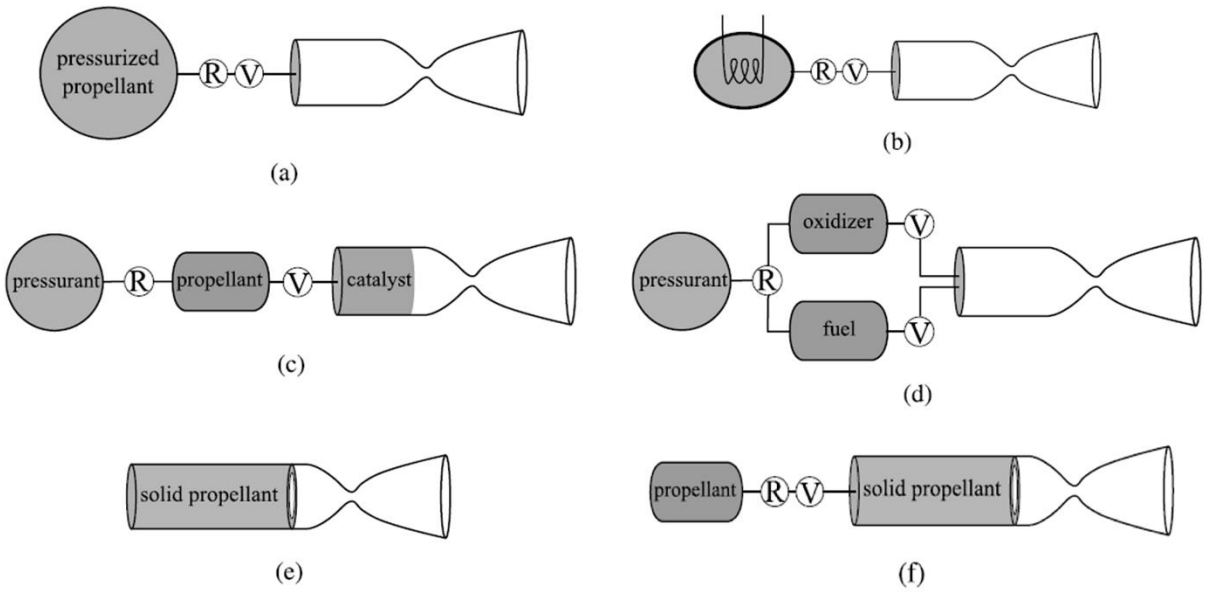

Figure 2.1 Compressed fluid propulsion schematics a) Cold gas b) Warm gas c) Monopropellant d) Bi-propellant e) solid propellant f) Hybrid [6]

2.1.1.1 Cold and warm gas propulsion

A high-pressure working gas expands through a converging-diverging nozzle to generate thrust, analogous to an inflated balloon from which the air can escape (Figure 2.1 a, b). Since thrust reduces as the gas pressure within the storage tank reduces over the mission lifetime, a pressure regulator is required to sustain a constant thrust, (Figure 2.2). In warm gas propulsion, the gas is heated prior to expansion using electrical power, typically from solar panels, generating higher thrust compared to cold gas (Figure 2.1 b). Alternatively, a steady arc discharge across the throat of the exhaust nozzle increases the temperature at the exhaust, higher than can be generated with conventional warm gas propulsion systems, hence increasing performance over warm gas propulsion. However, these require complex and power-intensive subsystems which limit their application [6]. Variations of this principle include exploiting phase changes of gases by storing them as compressed liquids and heating them prior to expansion (Figure 2.2) [7].

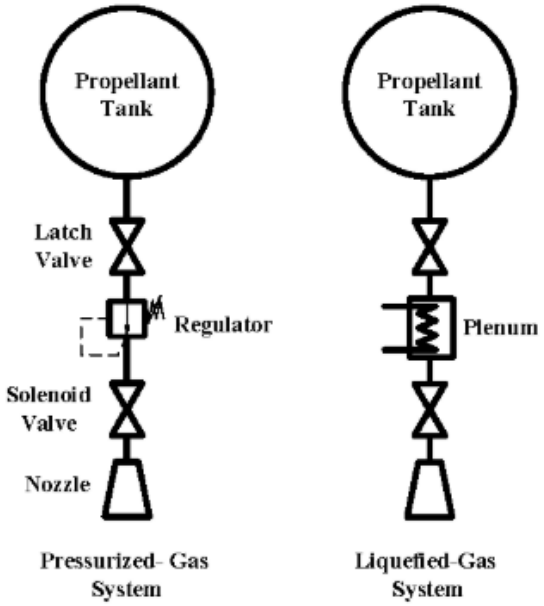

Figure 2.2 Cold gas propulsion systems [7]

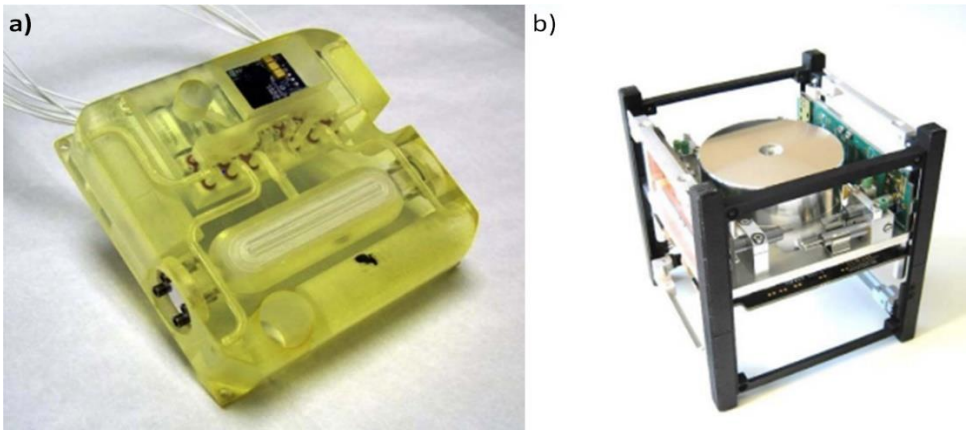

Figure 2.3 MEMS gas propulsion modules a) Cold gas propulsion b) Warm gas propulsion [4]

While cold gas systems require valves and other components to separate the high-pressure gas from the thruster nozzle and regulate fluid flow, the overall simplicity of the concept permits miniaturization into Micro-Electro-Mechanical Systems (MEMS); a cold gas system from Aerospace Corporation and a warm gas 1 U unit from NanoSpace are ready for use in CubeSats (Figure 2.3 a, b). MEMS thrusters based on cold gas propulsion have been commercialized and used in multiple CubeSat missions. These include the CanX-2 and CanX-5 satellites from the University of Toronto, MEPSI from the Aerospace Corporation, POPSAT-H1P1 from Microspace Rapid Pte. Ltd., Delfi-n3xt from TU Delft. Warm gas propulsion can be found in the CubeSat TW-1 from Shanghai Engineering Center for Microsatellites. Research groups and companies like Busek and CU Aerospace have developed launch-ready warm-gas propulsion modules [4]. Limitations of these systems include reduced thrust over the mission lifetime with reducing gas quantities, limited fuel capacity, cavitation effects caused by liquid sloshing in the tank, and the need for strong tanks that can withstand high gas pressures [8].

2.1.1.2 Chemical propulsion

In chemical propulsion systems, solid, liquid or gaseous reagents react or decompose into gaseous, high temperature working fluids that provide thrust when they are expanded through a converging-diverging nozzle into a higher temperature and lower pressure exhaust, hence providing thrust (Figure 2.1 c, d, e, f). With monopropellant thrusters, gases like hydrazine (N_2H_4), nitrous oxide

(N_2O), and liquids like highly concentrated hydrogen peroxide (H_2O_2) decompose exothermically in the presence of a catalyst into gaseous by-products. Companies like Busek have developed propulsion modules optimized for CubeSats (Figure 2.4).

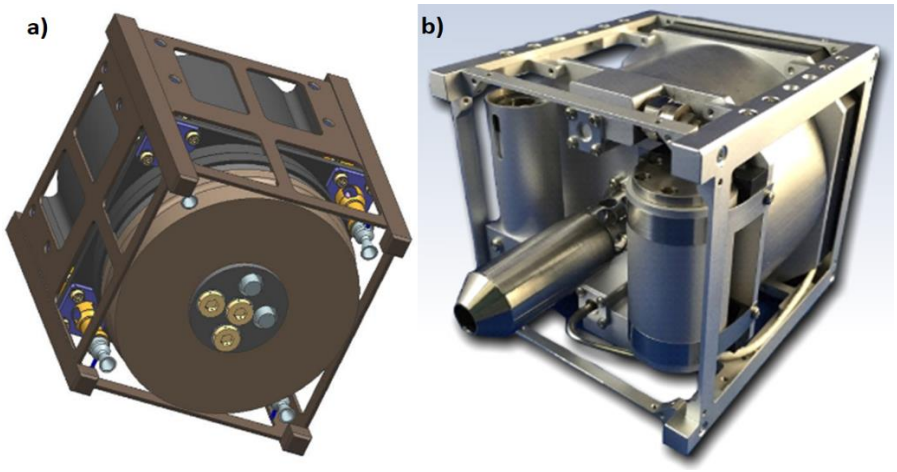

Figure 2.4 Busek hydrazine micropropulsion system a) CAD drawing b) Commercial system [9]

More advanced monopropellants like ammonium dinitramide (ADN) and hydroxylammonium nitrate (HAN) provide higher thrust than traditional monopropellants and combust at higher temperatures, generating higher specific impulse. However, they require far higher temperatures to ignite, and hence significantly more power is needed to achieve thrust [4]. Monopropellant combustion does not generate high temperatures, therefore standard materials can be used for the combustion chamber. However, these monopropellants are relatively unstable and require special handling.

Bipropellants require a reactant mixture of fuel and oxidizer, which generates gaseous products providing thrust when exhausted through a converging-diverging nozzle. Bipropellant systems have energy to perform orbital changes, however these require complex propellant feed systems with separate storage tanks and valves. Furthermore, the temperatures in the combustion chambers require the use of refractory materials, which could conduct heat by radiation to the other satellite components. Examples of such mixtures include classic mixtures like hydrogen and oxygen,

methane and H_2O_2, and advanced fuels like monomethylhydrazine (MMH), unsymmetrical dimethylhydrazine (UDMH) and oxidizers like dinitrogen tetroxide, MON-1, MON-3 [4], [6].

Solid propellant systems do not require complex valves. However, they cannot be restarted, i.e. once combustion commences, the reaction doesn't stop until all the fuel is consumed. Hence, these systems are used in de-orbiting maneuvers at the end of mission lifetime. Alternatively, some restarting capability is possible with solid propellant micro-thrusters, where hundreds of miniature microthrusters can provide thrust over the mission lifetime by sequential firing of individual or multiple thrusters (Figure 2.5). Restarting ability is possible in hybrid propellant systems, where the (solid) propellant is liquefied and transported to a separate combustion chamber; however, this comes at the cost of extra valve systems. Digital Solid Space Propulsion (DSSP) has the CDM-1 microthruster that uses a mixture of modified butadiene as fuel and ammonium perchlorate and/or aluminum as oxidizer [4].

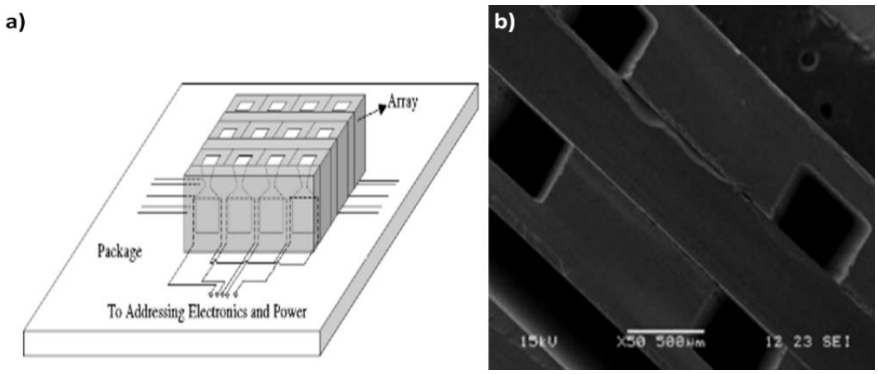

Figure 2.5 Example of solid propulsion system a) schematic of overall device b) SEM image of individual thruster units [10]

2.1.2 Electrical propulsion

In electrical propulsion, electrical power from solar radiation is used to generate thrust. There are three broad groups of electrical propulsion systems (Figure 2.6):

a) Electrothermal propulsion or warm gas propulsion has been discussed in section 2.1.1.1.

b) Electrodynamic: magnetoplasmadynamic (MPD), Pulsed Plasma Thruster (PPT) and Vacuum Arc Thruster (VAT)

c) Electrostatic: ion thrusters, Hall-effect thrusters and electrospray systems

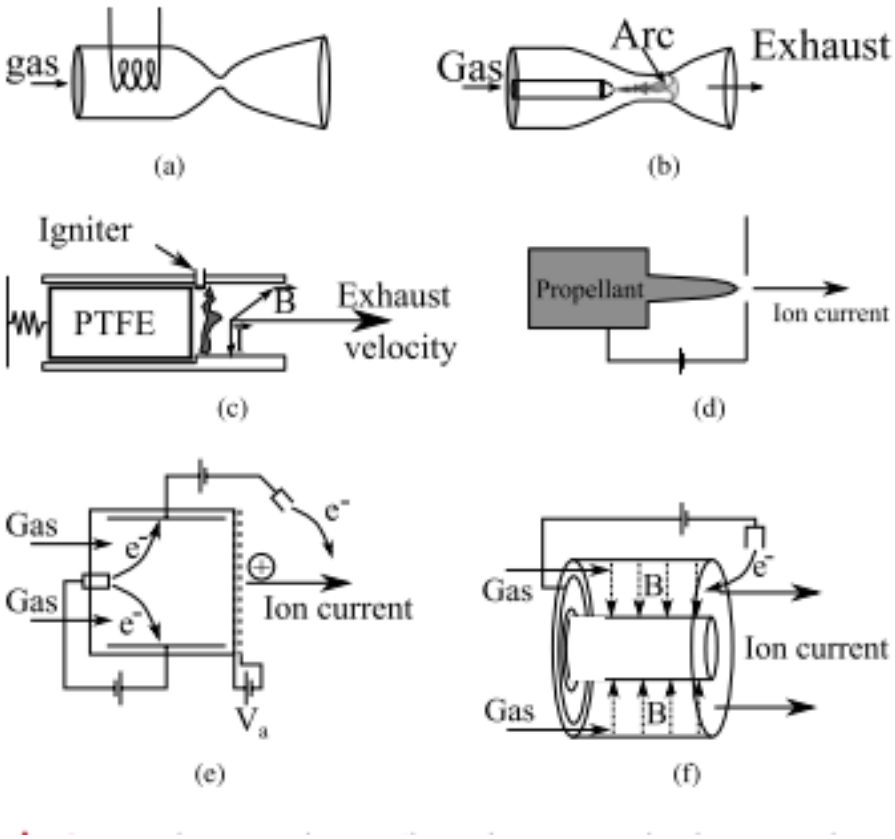

Figure 2.6 Electrical propulsion systems a) warm gas b) vacuum arc thruster c) pulsed plasma thruster d) field effect electrospray e) Ion engine f) Hall effect [11]

2.1.2.1 **Electrodynamic propulsion** [4], [6]

Also called electromagnetic propulsion, magnetic fields accelerate particle beams through a nozzle to provide thrust.

In MPD, an ionized gas is propelled by a Lorentz force, which is the result of an interaction between the electromagnetic field and a point charge, out of a nozzle, generating thrust. Lorentz forces are the combination of electrical and magnetic forces acting on a point charge within an electromagnetic field. The electromagnetic field is generated by an external power source, which consumes more power than can be generated by a CubeSat [6].

In PPT, a charged capacitor discharges and, in the presence of an ignitor, produces an electrical arc that vaporizes and partially ionizes a solid propellant like polytetrafluoroethylene (PTFE) (Figure 2.7 a). Under the influence of Lorenz forces from perpendicular magnetic fields around the acceleration chamber, the propellant is accelerated out of the nozzle, producing thrust. In general, liquid and gas propellants require more charge from the capacitor per pulse than solid propellants. However the former offers greater velocity changes than the latter. The mechanical simplicity, small velocity changes required by miniature satellites, use of solid and non-toxic PTFE, and pulsed nature of the capacitive discharge lends to the ease of miniaturization of this system. Due to these advantages, this system has been tested in manufactured CubeSats. However, the thrust efficiency is very low.

VATs are very similar in principle to PPTs. An arc simultaneously ablates and ionizes a propellant, which is propelled by Lorentz forces out of the nozzle to generate thrust (Figure 2.7 b). Here, an arc is formed between two electrodes under vacuum, which then ablates one of the electrodes, and ionizes, producing a plasma, which may be accelerated by the Lorentz force alone or combined with an acceleration potential to produce even higher thrust. This has been tested in the BRICSat, a United States Navy 1.5U CubeSat. VATs cannot perform orbital changes but can reduce the rotation or ‘tumbling’ of the satellite by 1 order of magnitude in 48h.

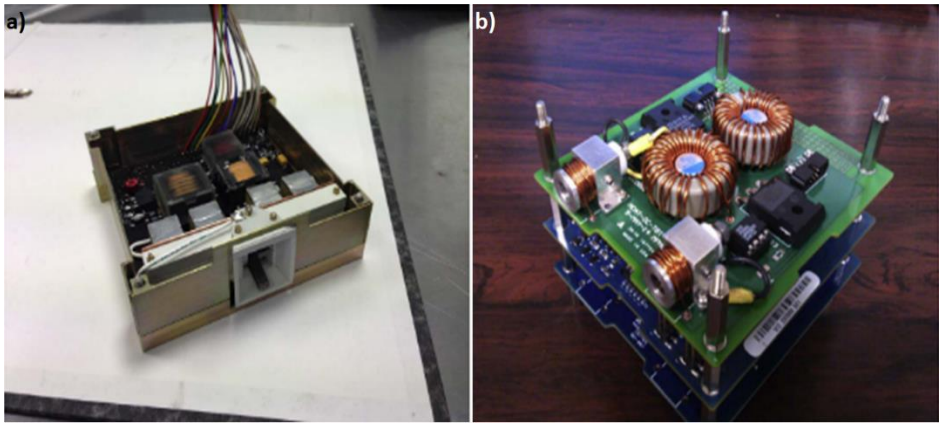

Figure 2.7 Electrodynamic propulsion a) PTFE PPT b) Arc thruster VAT [4]

2.1.2.2 Electrostatic propulsion

In electrostatic propulsion a potential difference between electrodes accelerates charged particles, typically ions, which generate thrust through momentum transfer.

Conventional ion thrusters, or Kaufman engines generate ions from inlet gases through collisions with injected electrons, interactions with microwaves and radio-frequency waves, or contact ionization, where particles become ionized upon contact with charged species. The ions are accelerated by a grid and the expelled ones are neutralized by an electron emitter. Disadvantages in microthruster applications include limited residence time of gases in the ionization chamber, which limits ion generation efficiency, lack of a durable miniature cathode for electron generation and accelerating grid erosion due to friction from accelerating ions, and limited gas supply [4].

The Hall-effect thruster exploits the Hall effect to ionize an inlet gas and accelerate the ions (Figure 2.8). Here, the ionization chamber is an annulus around a central rod or spike that serves as one pole of an electromagnet, the other pole being the outer wall of the annulus. Neutral gas flows into the annulus from a storage tank at the chamber upstream. Further downstream, close to the discharge part of the thruster, a cathode generates electrons, which are attracted to an anode in the chamber upstream. The anode also serves as a gas distributor. Under the influence of a

perpendicular magnetic field, the electrons are induced into a helical flight path, increasing their residence time within the chamber and hence probability of collision with incoming neutral gas molecules. Upon collision, the gas molecules become cations that are now attracted to the cathode at the chamber downstream due to the potential difference between the cathode and the anode. Upon exit from the chamber, the cations collide with some of the generated electrons, hence generating a neutral gas plume that generates thrust through momentum transfer. These systems have only been used in conventional satellites like the SMART-1 mission, and have been proposed for use in the miniature Iodine SAT (iSAT), which has not been launched to date [12].

Figure 2.8 Busek BHT-200 Hall Effect Thruster [13]

In electrospray thrusters, a conducting liquid forms into a Taylor cone, due to a high accelerating potential balancing the liquid surface tension, and ejects ions or liquid droplets, generating thrust. Electrospray thrusters may use an ionic liquid, electrolyte or a liquified metal, as propellant. When ions only are ejected, this is referred to as Field Effect Electrospray Thruster (FEEP), whereas if droplets are ejected, as in ionic liquids, this is a colloid thruster. In general, liquid metal sources emit higher current, however these require additional energy to liquefy the metal, whereas with

liquid sources, there is no need to include a heating element to liquefy the propellant, at the cost of lower ion emission and hence thrust. Since electrospray thrusters do not require generation of plasma discharge and hundreds of emitters can be fabricated on a single thruster, these are ideal for miniaturization and application in CubeSats. Busek has developed a liquid metal electrospray system (Figure 2.9 a).

In the case of electrospray thruster utilizing ionic liquids as propellants, no separate ionization is required, due to the intrinsic ionic nature of the liquids. By varying the polarity of the accelerating potential, the charge neutrality is maintained, and hence there is no need to include a charge neutralization circuit, further lending itself to miniaturization. A group at Massachusetts Institute of Technology (MIT) has developed a platform utilizing electrospray thrusters with ionic liquid as propellant, called scalable ion electrospray propulsion system (SiEPS) (Figure 2.9 b). This has been utilized in the Aerocube-8 mission. The initial testing indicated a 74 μN thrust. However, in-flight data is unavailable.

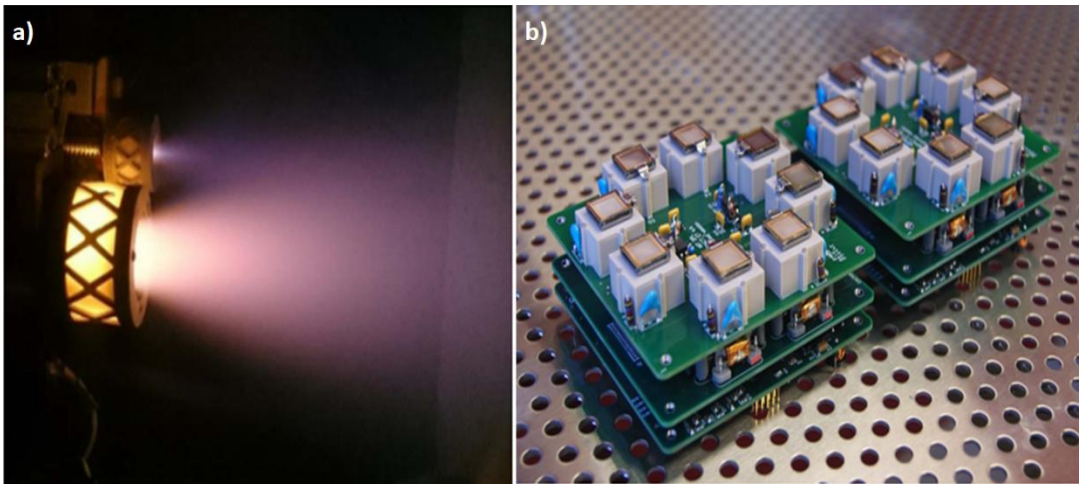

Figure 2.9 Electrospray propulsion a) Busek BIT-3 FEEP [4] b) sIEPS [14]

2.1.3 Propellant-less propulsion

2.1.3.1 Solar sail

Solar photons transmit momentum to a large surface area sail structure, for example in the LightSail-A about 32m^2, generating propulsion to CubeSats. In satellite missions like NanoSail D-2, the sail structure increased atmospheric drag for low-orbit missions, reducing de-orbiting time at mission end. As both these missions were proof-of-concept to demonstrate the deployment of solar sails, neither generated thrust to propel the satellite. A variation of this concept is photonic propulsion, where a laser beam that is amplified in a passive resonator, provides the photons that transfer momentum. While this is still at the laboratory stage, it can generate sufficient thrust to propel satellites to a fraction of the speed of light in vacuum. This can potentially be used in formation flying between satellites [4].

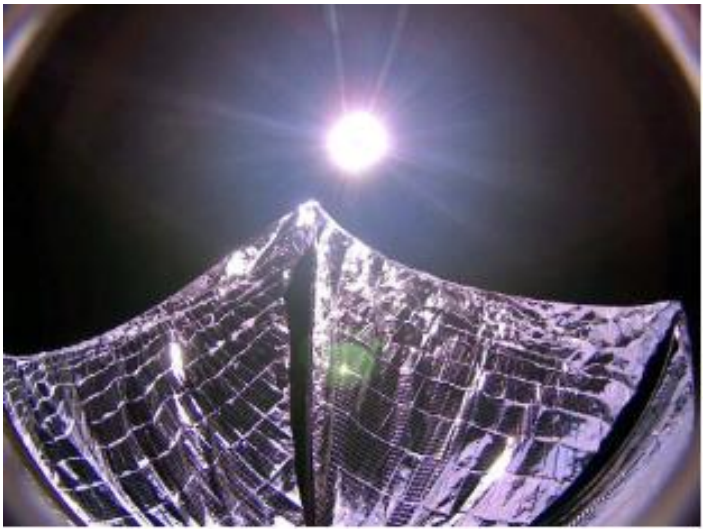

Figure 2.10 Solar sail [4]

2.1.3.2 Electrodynamic tether

This propulsion method is only suitable for orbits around earth at an altitude of less than 2000 km (low earth orbit). Two satellites are connected by a conductive wire of high tensile strength.

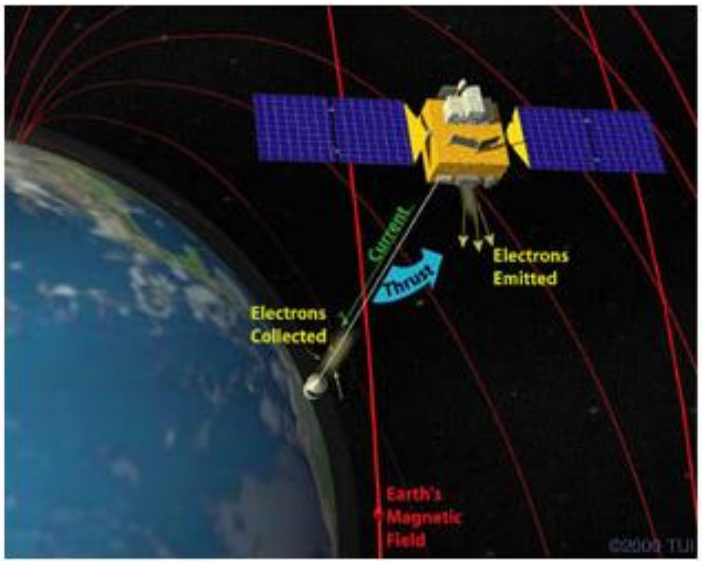

Figure 2.11 Electrodynamic tether [15]

In orbit, under the influence of the Earth's magnetic field a potential drop is generated in the conducting wire and hence current begins to flow through the wire, according to Faraday's law of induction:

$$V_{emf} = \int_0^L \left(\vec{v}_{orb} \times \vec{B}\right) d\vec{L} \tag{7}$$

Hence, a Lorentz force is generated:

$$\vec{F} = \int_0^L I(L)\overrightarrow{dL} \times \vec{B} \tag{8}$$

In self-propulsion mode, this force de-orbits the satellite. In order to provide propulsion, an on-board power supply provides an opposing potential difference and helps maintain orbit. This has not been successfully deployed from CubeSats, however, Tethers Unlimited Inc. have released the CubeSat Termination Tape with a mass of 83 g and a volume of 100 mm × 83 mm × 6.5 mm [4], [16].

2.1.4 Comparing propulsion system options

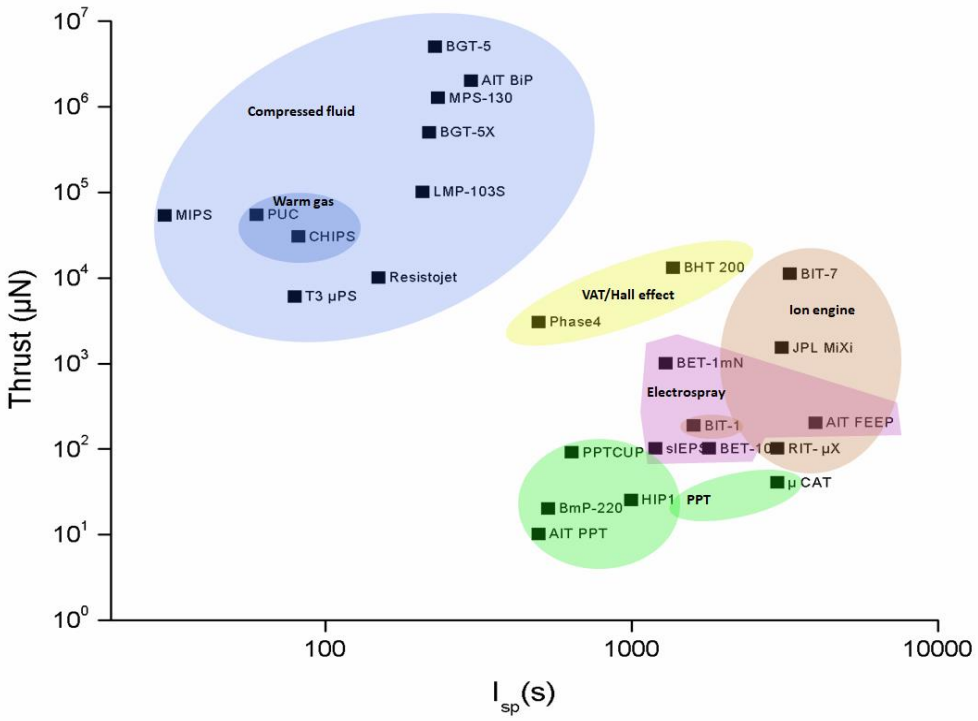

Figure 2.12 Comparison of microthrusters

Comparing the various alternatives, different systems have different applications (Figure 2.12). The thrust metric is the power provided, and the specific impulse is analogous to the total energy stored. Hence, while chemical and physical propulsion provide high thrust, it comes at the expense of lower total energy stored. While Hall thrusters and ion engines provide a good balance between energy stored and thrust provided, neither of these systems have been incorporated into miniature satellites, and hence require further development. Pulsed plasma and vacuum arc thrusters have significant flight heritage on miniature satellites, owing to their relative simplicity, however, these do not provide sufficient thrust, but do have high energy stored. Electrospray devices like FEEP and colloid thrusters provide a good balance between high energy stored and thrust, while lending

itself well to miniaturization and ease of manufacture. Hence, in this project, an electrospray device will be fabricated.

2.2 The Electrospray Thruster

Charged particle emission is induced by applying an accelerating electrostatic potential to a liquid ionic conductor, e.g. an ionic liquid or electrolyte. Zeleny performed an experiment where a dilute hydrochloric acid solution flowing through a glass capillary demonstrates electrospray under the influence of a several-thousand volt accelerating potential applied between the liquid and a ground electrode placed about 1.5 cm below the glass capillary tip (Figure 2.13) [17].

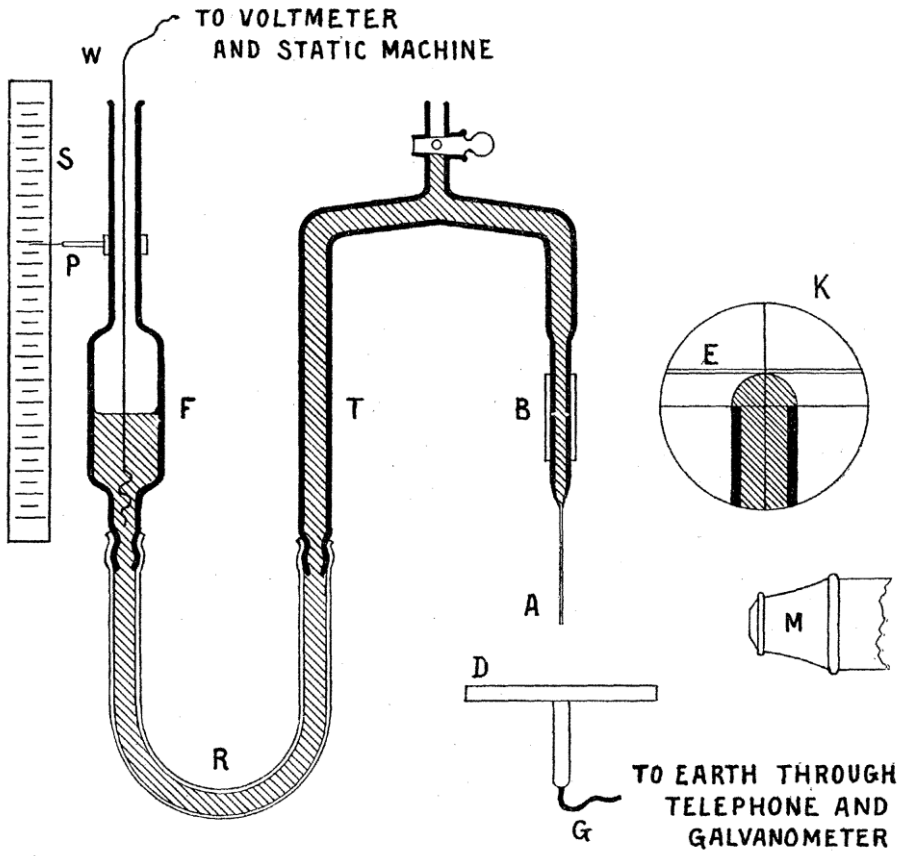

Figure 2.13 Zeleny's electrospray apparatus [17]

The central concept is the Taylor cone, which is a static conical meniscus formed by a conducting liquid in the presence of a strong electrical field; this occurs when the liquid surface tension is balanced by a high accelerating potential. At this point, a cone with a half angle of 49.3° forms and at the apex strong electric fields induce emission of charged species (Figure 2.14).

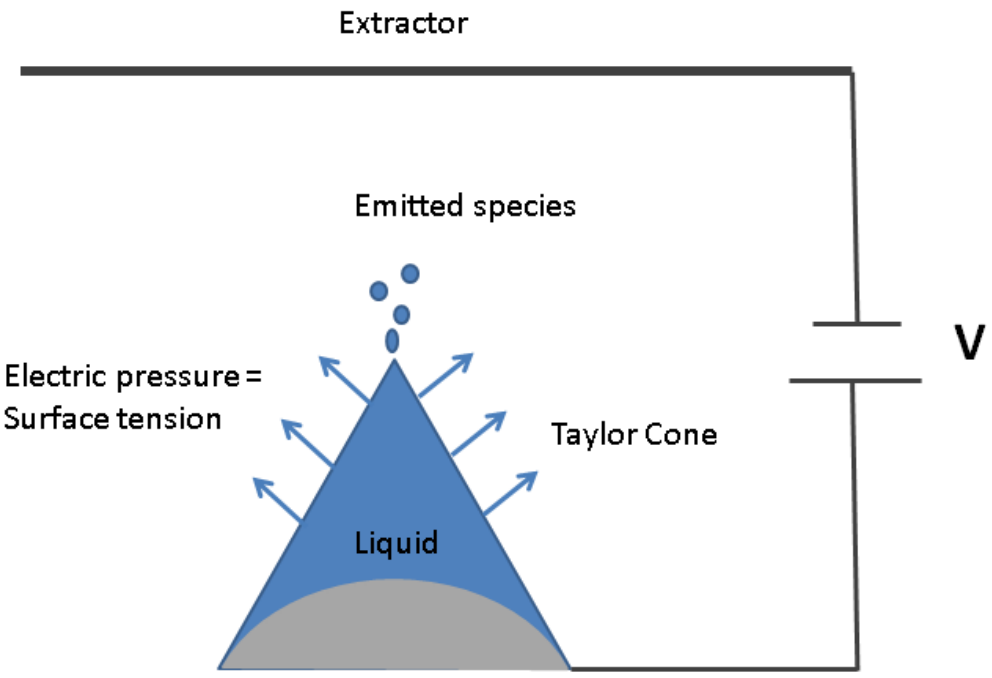

Figure 2.14 Taylor cone [18]

The governing equation for Taylor cone formation is given by:

$$\frac{1}{2}\epsilon_0 E_n^2 \cong \frac{2\gamma}{R} \tag{9}$$

Where E_n is the normal component of the electric field, R is the radius of curvature of the substrate at each emission point, γ is the liquid surface tension, and ϵ_0 is the vacuum permittivity.

The starting voltage, which is the voltage beyond which emissions commence, is given by:

$$V_{start} = \sqrt{\frac{\gamma R}{\epsilon_0}} \ln\left(\frac{4d}{R}\right) \tag{10}$$

Where *d* is the distance of the emitter tip from the accelerating electrode. An electrospray system would consist of a substrate with emitters, either cones or prisms with sharp tips, patterned on the substrate surface. Courtenay mentioned the possibility of each emitter tip supporting multiple Taylor cones or ion emission sites (Figure 2.15) [5].

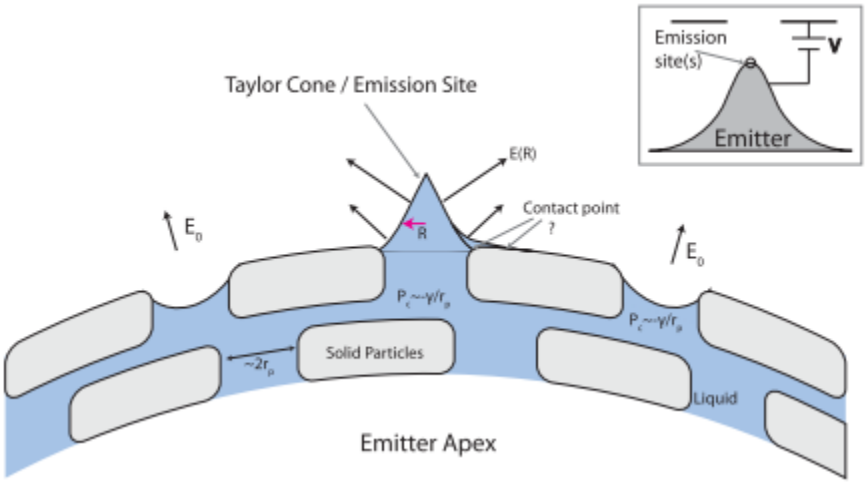

Figure 2.15 Multiple emitter sites on a single emitter tip [5], [18]

There are two types of electrospray systems:

- Externally wetted (Figure 2.16 a): A conducting liquid wets the exterior of a non-porous emitter tip
- Passive feed: liquid from a reservoir is transported by capillary action through a porous substrate patterned into a emitter tip (Figure 2.16 b), or through a capillary etched into a monolithic emitter tip (Figure 2.16 c).

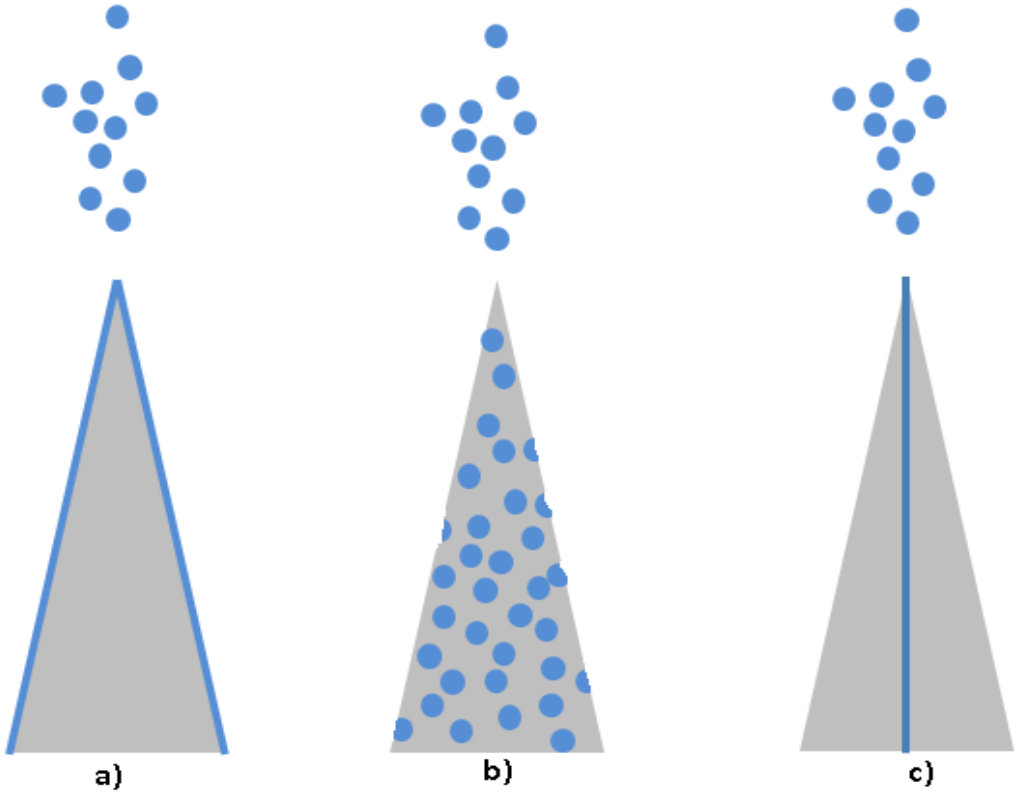

Figure 2.16 Modes of electrospray a) externally wetted b) porous passive feed c) capillary passive feed [18]

2.2.1 Externally wetted devices

Nakagawa et al have fabricated externally wetted microthrusters from silicon, utilizing conventional microfabrication (Figure 2.17 b). Here, an array of hundreds of thrusters, each in the form of a cylinder with a conical lid was etched into a silicon substrate by conventional photolithography followed by Bosch-process Deep Reactive Ion Etching (Figure 2.17 a). The ionic liquid was stored in a reservoir in the spaces between the thrusters. A stainless-steel emitter grid with openings corresponding to the individual thrusters was fabricated and placed 0.5mm above the thrusters (Figure 2.17 c). When high voltage is applied through the emitter grid, the ionic liquid is attracted to the emitter tip and dissociates into ions; based on the polarity of the high voltage, the oppositely charged ions are emitted through the openings. This system is susceptible to short circuiting if the ionic liquid is over-filled in the reservoir [19].

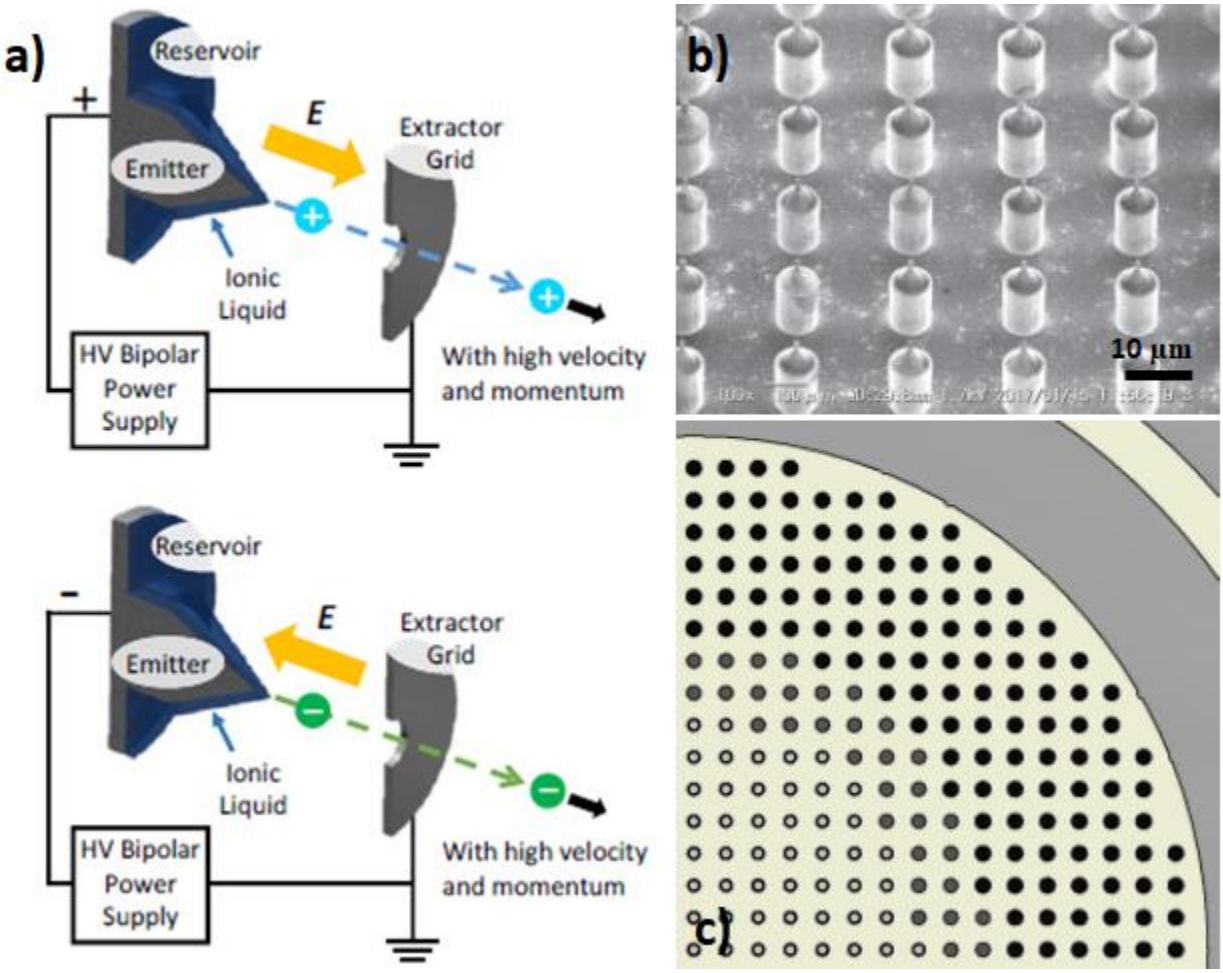

Figure 2.17 Externally wetted electrospray device a) schematic of working principle b) SEM image of emitter tips c) mask layout to etch emitters [19]

Externally wetted devices have not been researched beyond this work. While attractive in its simplicity, this technology requires development. Alternatively, it has been proposed to incorporate an active feed system that will feed ionic liquid on to the emitter tips. However, this may add unwanted bulk to the device.

2.2.2 Passive feed devices

Passive feed devices rely on capillary action to transport the ionic liquid from the reservoir to the emitter tips. This is achieved by capillary tubes within each emitter or fabricating the emitters from a porous substrate. Since fuel transport relies on capillary action, complicated and bulky fuel feed systems and piping are not required. This enables compact and light thruster systems, which are easy to accommodate within miniature satellites. While these share the disadvantages of other electrical systems, i.e. low thrust output, devices can be multiplexed together to provide sufficient thrust.

The liquid flow can be approximated by Darcy's law which describes fuel flow through a porous medium:

$$Q = -\frac{\kappa}{\mu}\nabla P \tag{11}$$

Where Q is the fluid flow per unit area, κ is the cross-sectional area to flow, μ is the liquid viscosity, and ∇P is the pressure gradient.

In the absence of active feed mechanisms, the accelerating potential provides the pressure difference: $\Delta P = ZQ$ where Z is the liquid resistance. Hence equation (10) for minimum starting voltage must be modified to account for the complex pore structure;

$$V_{start} = \sqrt{\frac{4\gamma R_c}{\epsilon_0}}\sqrt{\frac{R_c}{r_p}}\ln\left(\frac{4d}{R_c}\right) \tag{12}$$

Where the emitter is approximated as a paraboloid of radius R_c, and r_p is the length of the pore.

For a pore structure that is approximated as a tall cylinder, the pressure gradient ∇P can be approximated as:

$$\nabla P = \frac{\mu Q r_p}{\pi \kappa R_c^2} \tag{13}$$

The ion beam velocity can be approximated by:

$$c_i = \sqrt{2V\frac{q_i}{m_i}} \tag{14}$$

Where V is the accelerating voltage and q_i/m_i is the charge to mass ratio of the individual ions [5].

Fabricating capillary emitters required high precision. Previous research has focussed on creating capillaries in photoactive polymers. Henning et. al. photolithographically created holes into 35-80 µm SU-8 photoresist spin-coated onto a 2" silicon wafer. After this, the silicon wafer was dissolved in a warm potassium hydroxide bath, and the released photoresist was cut and glued onto a vacuum-compatible material prior to charging the capillaries with ionic liquid and testing in a vacuum chamber. The authors also used a Nano-Scribe™ maskless lithography tool, which uses a two-photon femtosecond laser to expose a thick photoresist in 3-D, reducing the complexity of photolithography [20].

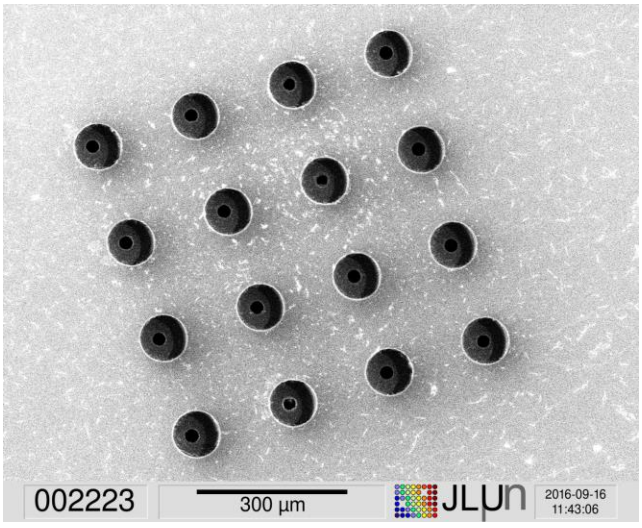

Figure 2.18 SEM of capillary emitters with 30 µm diameter capillaries [20]

Fabricating emitters from porous substrates is an attractive option, because of the wide variety of candidate materials available and intrinsic capillary ability of these materials, hence not requiring a separate etching process to create capillaries. The challenge is to adapt patterning techniques that will not damage the existing pores must be chosen.

Candidates include sintered metals, borosilicate glass and carbon xerogels. Metals can be patterned by electrochemical etching using a moving electrode, while glass can be patterned with lasers and CNC machining [21], [22]. Pores in sintered metals can be damaged by electrochemical processes, while glass particles from machining steps can easily damage sensitive equipment and machine parts, which is not viable for facilities at Polytechnique.

Carbon xerogels are dehydrated gels that are easily manufactured from carbonaceous materials; depending on the choice of initial raw material, their porosity and pore type can be easily tuned. Resorcinol-formaldehyde is a common precursor, the porosity and pore size can be manipulated depending on the pH of the catalyst, concentration of reactants and curing temperature. Hence, for this project carbon xerogels will be investigated and patterned with multiple microfabrication processes, including laser ablation, reactive ion etching (RIE), pre-patterning prior to pyrolysis, and dicing [23].

2.3 Carbon xerogel

The IUPAC states that a gel is a non-fluid colloidal network or polymer network that is expanded throughout its whole volume by a fluid [24]. A gel is made up of liquid confined within a three-dimensional matrix of cross-linked molecules. Hence, elimination of the liquid will yield a solid that is highly porous and possesses large surface area, i.e. aerogels and xerogels. Conversely, in xerogels the pores collapse, increasing the density and decreasing the volume (Figure 2.19).

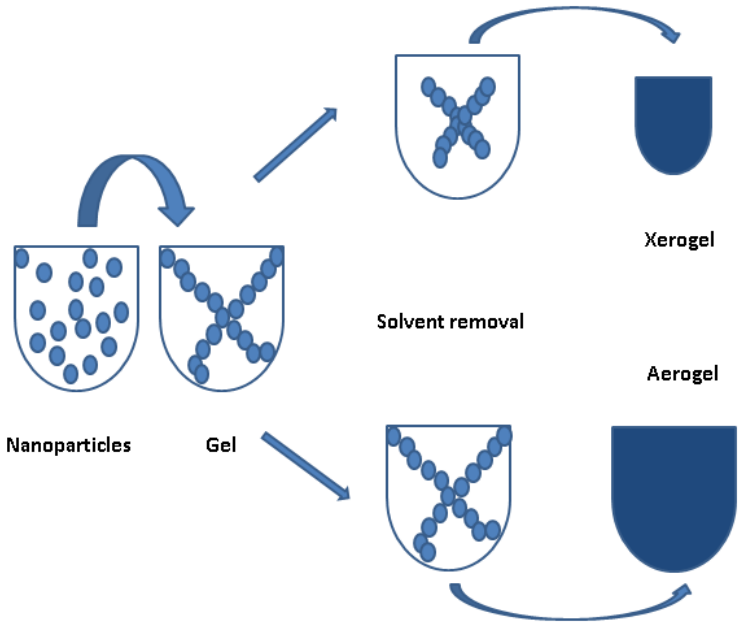

Figure 2.19 Xerogel vs. Aerogel [18]

Aerogels retain the original volume and are less dense than the original gel when the solvent is driven out. However, these are difficult to produce because without precaution, the pores will collapse due to surface tension as the solvents are eliminated. Hence, drying methods center around solvent exchange, CO_2 in the case of supercritical drying and acetone in the case of ambient drying, or changing the drying conditions, vacuum drying gels with low catalyst concentrations in the case of subcritical drying and below-freezing temperatures and low pressures to facilitate solvent sublimation in the case of freeze drying. Supercritical and freeze drying are prohibitively expensive and hard to handle, and all methods add to the complexity of production [25].

In comparison, xerogels are far easier to produce, using methods like pyrolysis to eliminate the liquid, yielding a porous and dense solid. Carbon xerogels are also conductive.

The precursor gel is synthesized in an acid-catalyzed condensation between resorcinol and formaldehyde. The acid protonates the formaldehyde, which reacts with resorcinol to form methylene-bridged resorcinol resin. The hydroxyl group is attacked by protonated formaldehyde to form a resorcinolic unit with a R-H_2O^+ sidechain, which reacts with a new resorcinol unit with release of water. This reaction continues resulting in the creation of a matrix structure with water trapped in the voids , forming a gel (Figure 2.20). Either acidic or basic catalyst can be used. However, reducing the pH results in larger pore size gels with lower volumetric shrinkage upon drying. Increasing catalyst concentrations reduce gelation times, surface area and pore volumes; increasing the temperature reduces the reaction duration and facilitates drying in ambient air [26], [27].

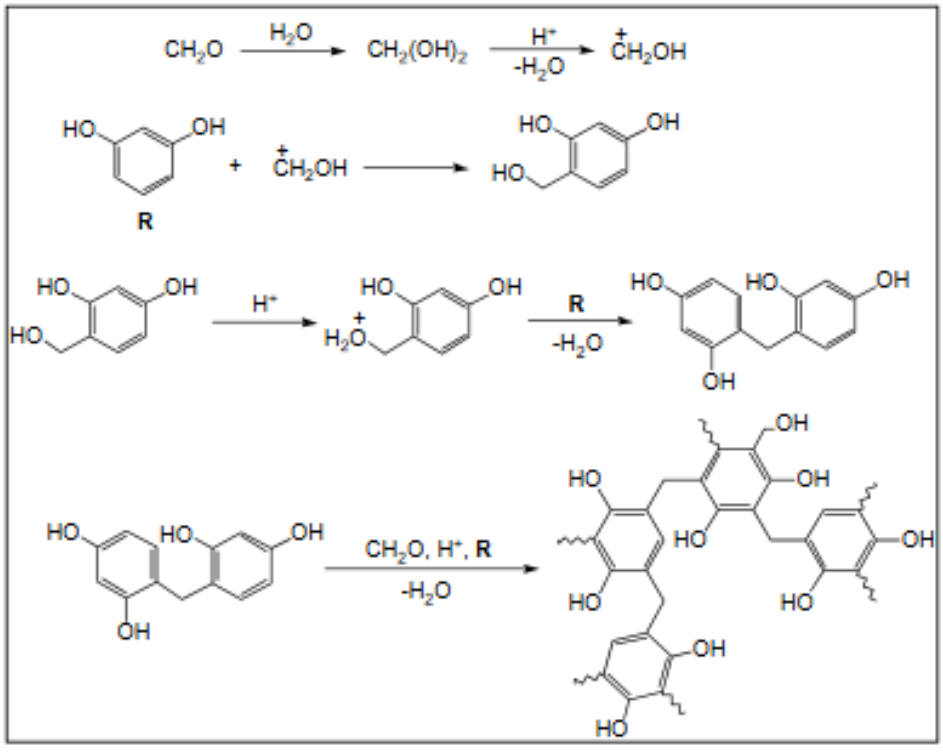

Figure 2.20 Resorcinol-formaldehyde proposed gelation mechanism [28]

Upon evaporation of excess solvent, a brown gel is obtained. Upon pyrolysis, where the material is heated at elevated temperatures (500°C<T<1000°C) in an inert atmosphere to break down chemical bonds and drive out solvent, the volatile molecules are driven out leaving almost pure carbon, resulting in a porous solid with a lower bulk volume, a carbon xerogel.

2.3.1 Xerogel porosity

Lawrence and Jiang reviewed various methods of porosity determination (Figure 2.21) [29]. Pycnometry and water immersion porosimetry offers the widest range of pore size determination, from micropores all the way to macropores. However, from SEM images, it's clear to see that such a wide range of pore sizes is not present. Mercury Intrusion Porosimetry (MIP) permits the determination of a wide range of pore sizes, especially macropores. MIP was chosen to determine the pore size distribution; for carbon xerogels, two scanning regimes were carried out, low pressure for the larger pores and high pressure for the smaller ones.

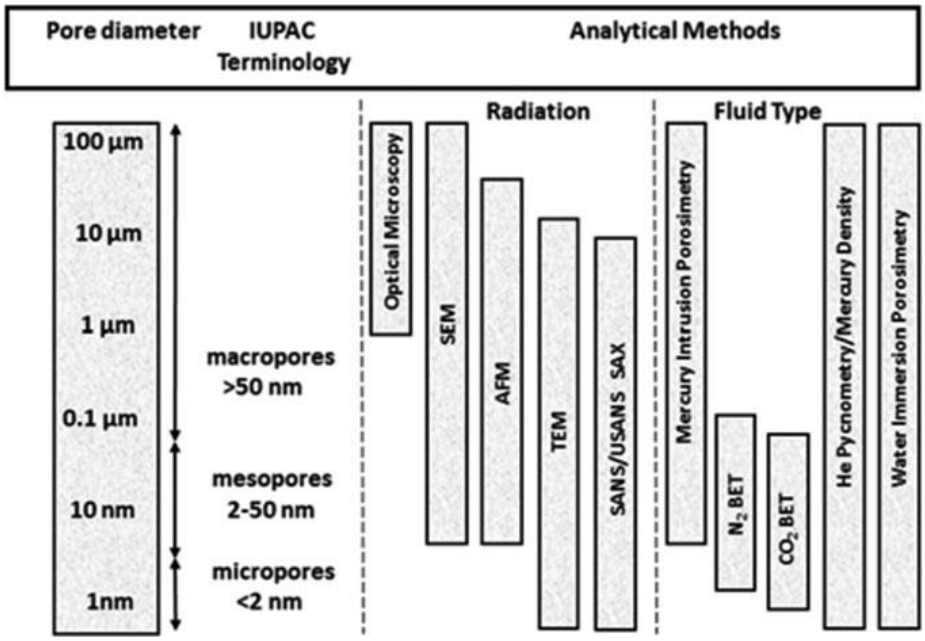

Figure 2.21 Methods to determine pore size distribution [29]

In MIP, the sample is placed into the testing container, which is evacuated to eliminate water vapour, and is filled with mercury; the sample needs to be broken up into powder to fit into the container. The pressure is increased gradually in steps in two stages, a low-pressure mode, allowing the mercury to intrude, into the larger pores, and a high-pressure mode, where the mercury intrudes into the smaller pores. The Washburn equation for cylindrical pores can be applied here:

$$D_P = \frac{-4\gamma \cos\theta}{P_L} \tag{15}$$

Where D_P is the pore diameter, γ is the surface tension of mercury which is 480 mN/m under evacuation, θ is the mercury contact angle about 140° and P_L is the liquid mercury pressure. The pore size distribution by pore size is obtained from the difference between the cumulative intrusion volumes at each pressure step [30].

2.4 Microfabrication

Microfabrication is the process of fabricating micron-scale structures or patterns on substrates, typically on silicon dioxide or semiconductors like silicon. Four microfabrication strategies, were explored in this thesis:

1. Reactive Ion Etching (RIE)
2. Femtosecond laser Ablation
3. Pre-patterning using an elastomeric stamp
4. Using an automated dicing saw to cut patterns into the substrate

2.4.1 Oxygen Plasma Reactive Ion Etching (RIE)

Oxygen Plasma RIE is a chemical etching method that uses radio frequency to convert oxygen into plasma, a gas of oxygen ions that are more reactive than oxygen gas. Conventionally, this is used to strip away trace quantities of photoresist after development in photolithography. In conventional silicon-based microfabrication, the oxygen species react readily with organic materials while

reacting much more slowly with the silicon substrate to create hydrophilic silane groups (Figure 2.22). Typically, this is used with thicker photo-resists (> 2 μm) where the developer may not have completely washed away the de-polymerized resist, leaving behind a very thin film (typically nanometres thick), that may then interfere with subsequent microfabrication processes like lift-off after metal deposition or deep-reactive ion etching (DRIE), etc. RIE is a way of rapidly and precisely removing these thin films.

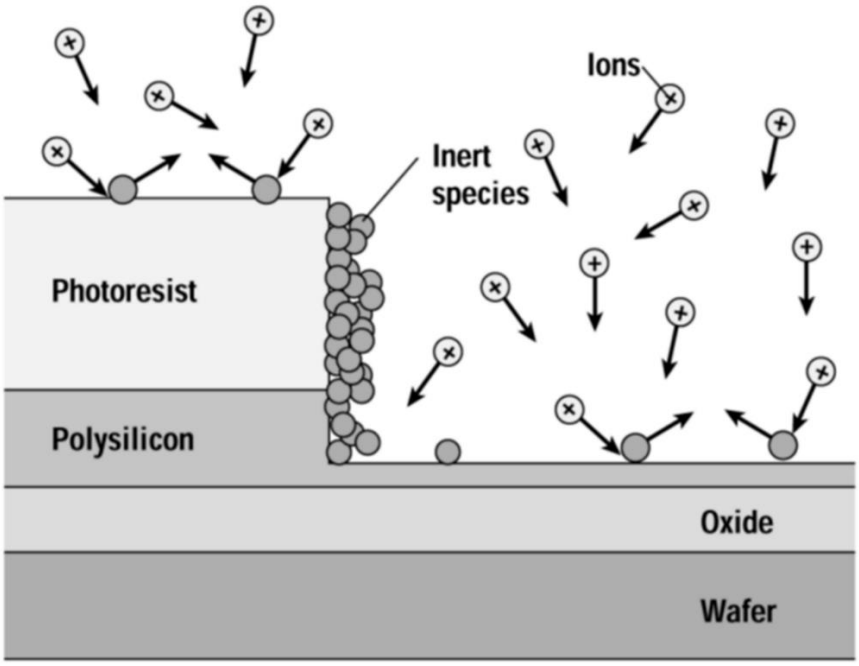

Figure 2.22 Reactive Ion Etching schematic [29]

2.4.2 Laser ablation

Rojas-Herrera et al. used a UV-wavelength picosecond laser with a 20 μm-beam to raster-scan across a xerogel surface that was previously bonded on a device housing, and created 300 μm high emitter tips (Figure 2.23). Prior to emission testing, the xerogel was soaked with ionic liquid 1-Ethyl-3-methylimidazolium tetrafluoroborate (EMIM-BF_4) and outgassed in the testing vacuum chamber to eliminate volatile species. Scanning the potential between ±1000 V gave a maximum current output of 180 μA [23].

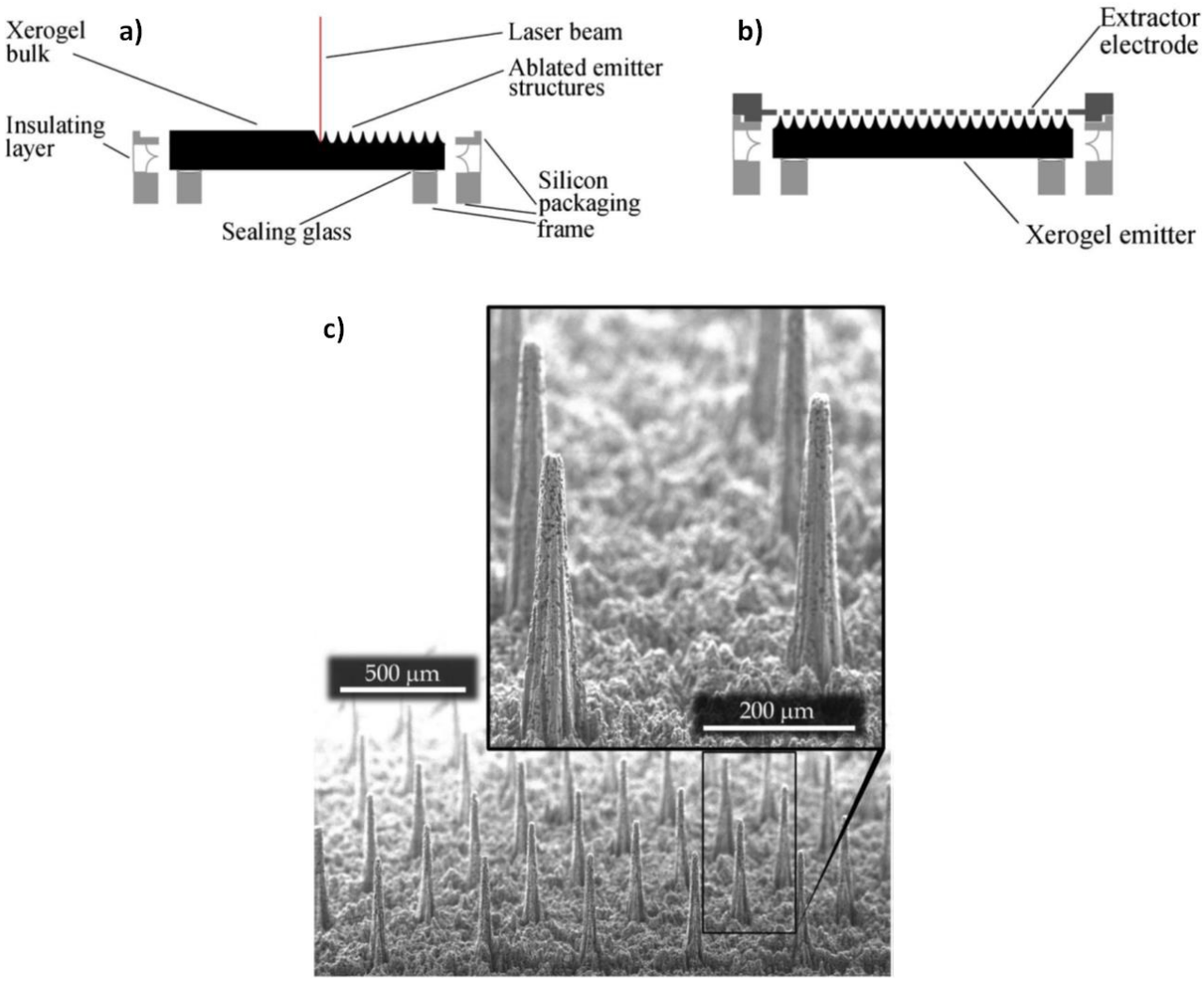

Figure 2.23 Picosecond laser ablation a) ablation schematic b) side-view of patterned xerogel c) microstructures [23]

2.4.3 Pattern transfer using an elastomeric stamp

Sharma et al. reported micron-scale pattern transfer from an elastomeric stamp to carbon xerogels. They generated a polydimethysiloxane (PDMS) stamp from a master pattern, which was then used as a negative to transfer the master pattern onto a liquid RF sol, which after curing and pyrolysis maintained the intended pattern (Figure 2.24). The master pattern was created by spin-coating SU-

8, a negative photoresist, onto a SiO_2/Si substrate, patterning by conventional photolithography and pyrolyzing to create a (non-porous) glassy carbon master pattern. Successively smaller patterns can be created by using the elastomeric stamp to pattern SU-8, and repeating the pattern transfer multiple times [31].

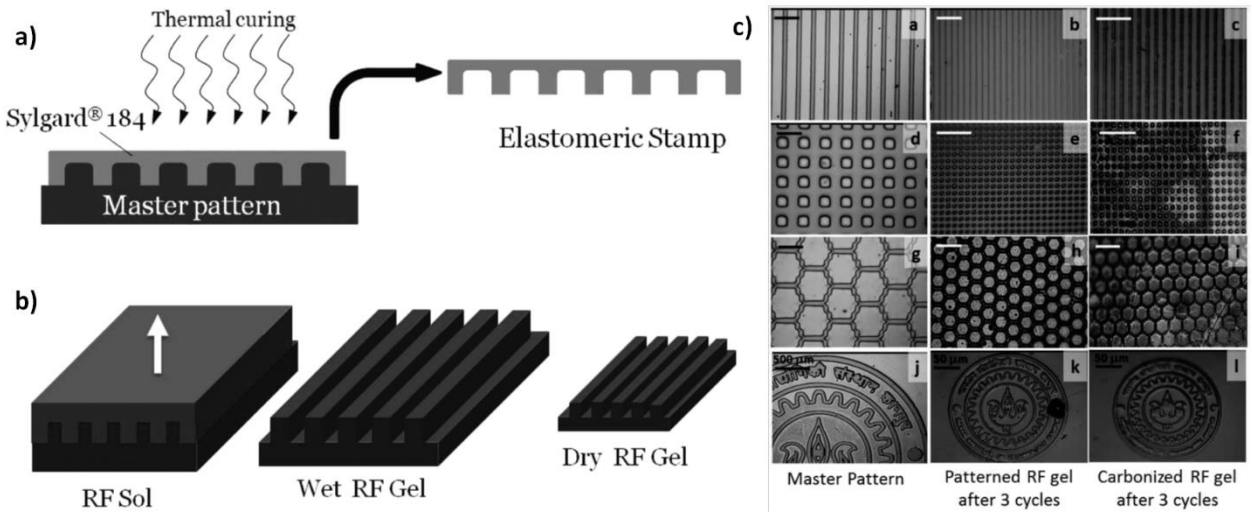

Figure 2.24 Pattern transfer from glassy carbon master a) PDMS stamp creation from master pattern b) Transfer to resorcinol-formaldehyde sol followed by curing, removal of stamp and gel pyrolysis c) various patterns created [31]

2.4.4 Dicing

Bhandari et al. used an automated silicon wafer dicing machine to create saddle-shaped silicon micro-electrode arrays for prosthetics (Figure 2.25). A 150 µm thick blade cut grooves into the silicon into the different heights required by the design. From the schematic, the blade is run through each groove twice, implying that a comparable dicing machine has more than sufficient accuracy to obtain clean-cut grooves on the substrate [32].

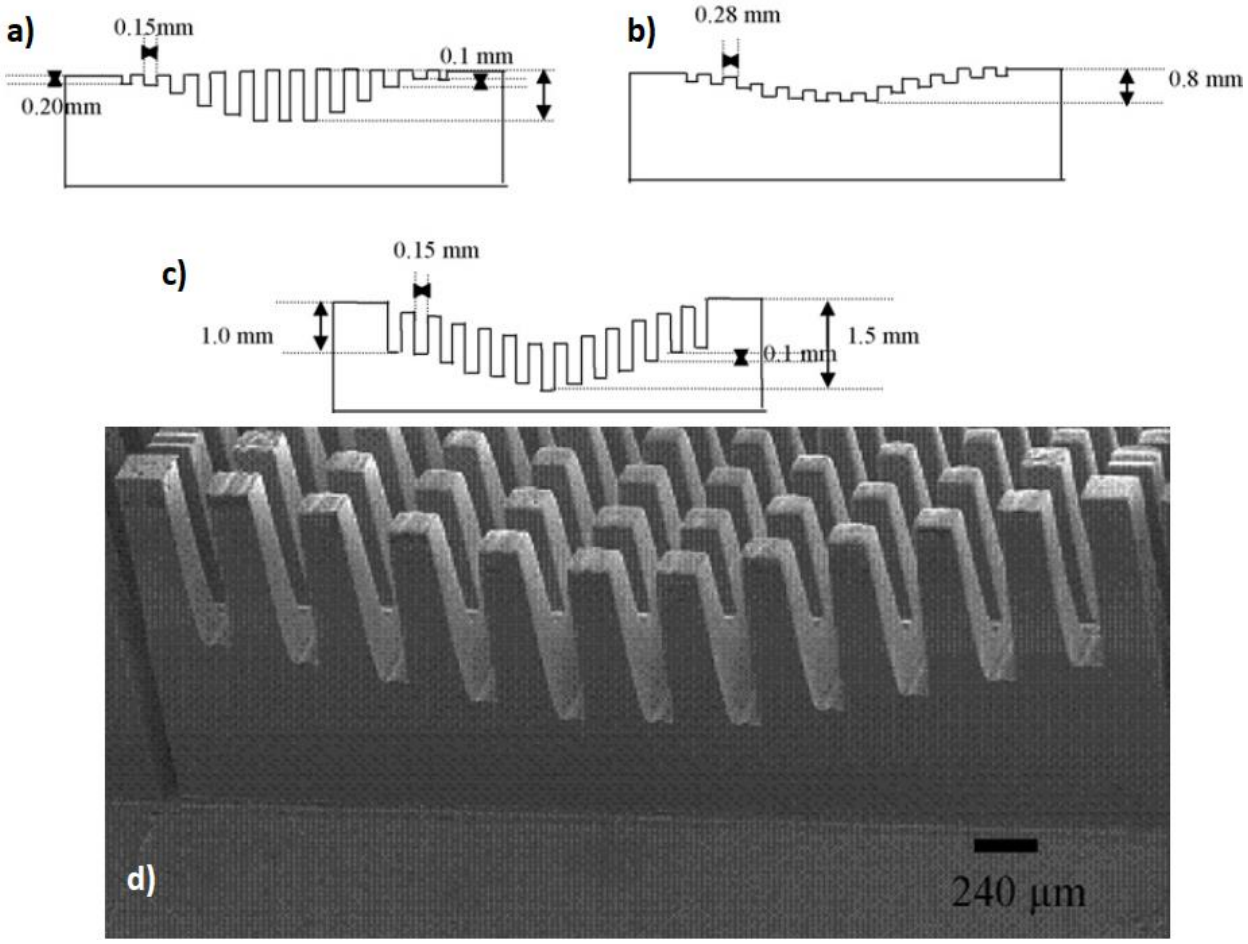

Figure 2.25 Silicon saddle-shape patterning by dicing a) initial dicing b) DRIE etching of pillars c) dicing in the same grooves d) SEM image of wafer [32]

CHAPTER 3 MATERIALS AND METHODS

3.1 Chemicals

Isopropanol (IPA, C_3H_8O, 70%) and acetone (C_3H_6O, 90%) were purchased from Honeywell Research Chemicals and used for cleaning glassware. Water purified in an EMD Millipore MilliQ water purification, resorcinol (Sigma Aldrich, # 398047), 37% formaldehyde solution (Sigma Aldrich, #252549) and glacial acetic acid (Sigma Aldrich, #338826) were used to synthesize resorcinol-formaldehyde gels. Microposit 1165 and AZ 900 MIR was purchased from Dow Chemicals and Microchemicals GmbH respectively. All chemicals were used as received.

3.2 Xerogel synthesis

For this project, a resorcinol:formaldehyde:acetic acid molar ratio of 15:30:1 was used. First, 28 g resorcinol was dissolved in 34 g MilliQ water, using an ultrasonication bath to break up the resorcinol flakes and speed up dissolution. Then, 41 g of formaldehyde was added and the mixture stirred gently to dissolve all reagents together. Finally, 1 g glacial acetic acid was added to the resorcinol-formaldehyde mixture with a dropper and agitated in an ultrasonication bath for 60 s. The mixture was poured into a steel mould and covered with Parafilm and allowed to gel for 24 h in a fume hood. The mould is then transferred to a 40°C oven (DX 300) for 24 h, then the temperature is increased and maintained at 60°C for 24 h. The temperature is again ramped to 80°C and maintained for 72 h. At the end of this period, the oven is switched off and the mould cooled to room temperature over 24 hours. The mould is then returned to an 80°C oven for 72 h [18].

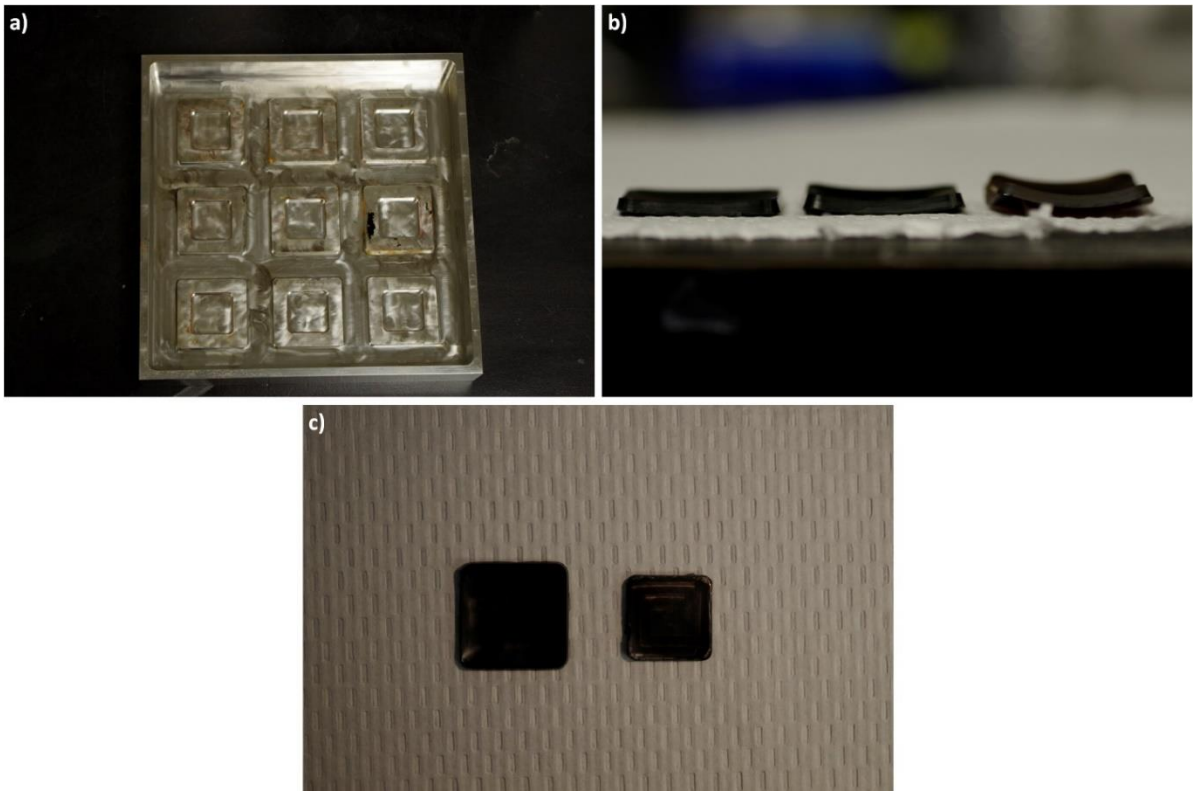

Figure 3.1 Initial xerogel moulding process a) Stainless steel mould b) Increased bowing with wearing of mould finish c) RF gel before pyrolysis (left) and xerogel (right)

At first, samples were flat, but as the mould surface was slowly eroded from the manufacturer's finish, the samples became more bowed (Figure 3.1 a and b). Another reason for the bowing could be that the heat transfer between the cooling gel and air, and the cooling gel and metal surface was too rapid, not allowing for the material to retain its flat shape, only possible through gradual cooling. Hence, one strategy that can be followed would be to restore the finish with a polishing operation on a computer numerical control (CNC) machine. Another strategy to allow for a more gradual cooling involved gelling and curing the organic precursor using the same protocol in a glass beaker, slicing the resulting solid into pieces into pieces with a table saw prior to pyrolysis; this strategy, being simpler, was adopted.

The samples were pyrolyzed in a tube furnace under argon atmosphere ramped to 900°C at 2°C/min, soaked for 3 h and cooled within the cooling furnace. The xerogel volume was smaller than the pre-pyrolyzed gel (Figure 3.1 c). The finished xerogel had a shiny 'skin' that was patterned with the finish of the mould. Xerogels were polished with a 6 μm grit carbide pad prior to further experimentation

3.2.1 Mercury Intrusion Porosimetry (MIP)

The xerogel pore size distribution was studied with MIP (Figure 4.3). Here, mercury, a non-wetting liquid, is forced under pressure into the pores of the material. Based on the pressure required to overcome the liquid surface tension, and hence force mercury into the pores, the pore size can be estimated. The higher the pressure required, the smaller the pore diameter.

3.3 Microfabrication

3.3.1 Reactive ion etching (RIE)

A xerogel is covered with a protective resist, patterned, and exposed to a 300 W radio-frequency plasma under 10 sccm oxygen flow (Figure 3.2).

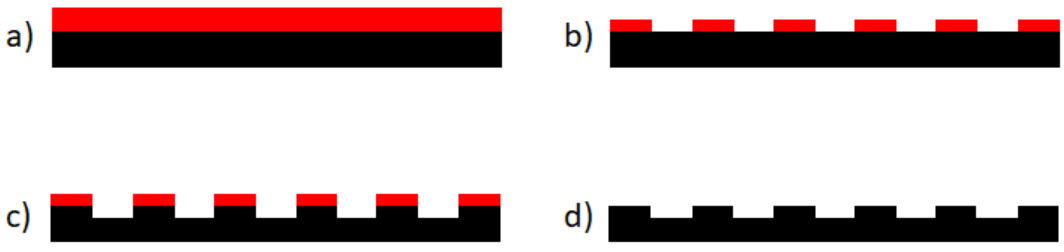

Figure 3.2 Initial RIE process a) depositing photoresist b) patterned photoresist c) xerogel RIE d) photoresist stripped

In metal masking RIE, a 2.5 µm thick positive photoresist, AZ900 MIR, was spin-coated onto xerogel and patterned by a conventional photolithography process using a negative photomask. In the now exposed xerogel, a 100 nm titanium layer was deposited by e-beam deposition; the photoresist is eliminated with Microposit 1165 remover. At the end of the process, the metal can be removed by acid treatment or metal etchants (Figure 3.3).

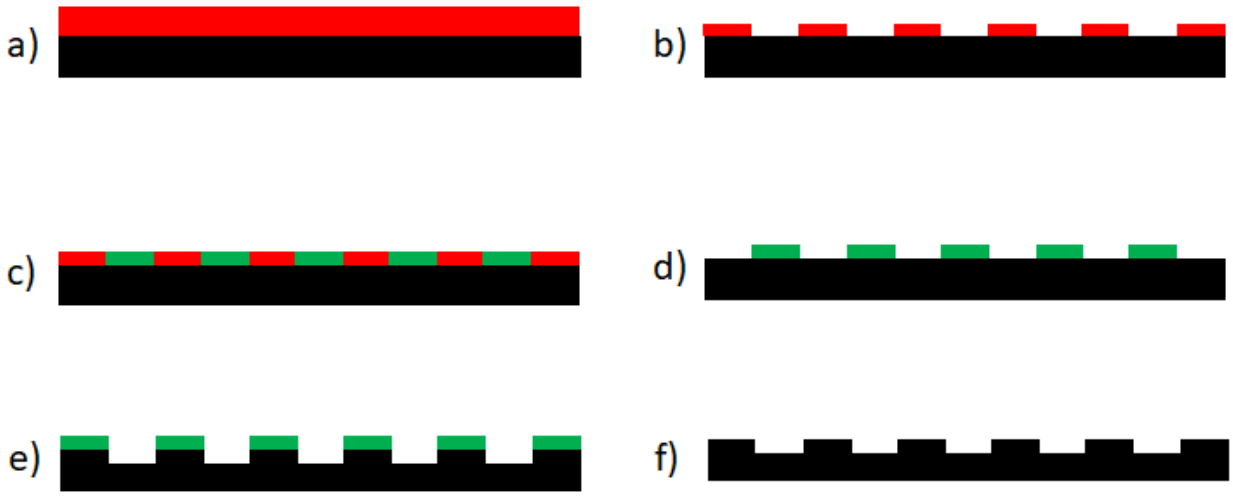

Figure 3.3 Modified RIE process a) depositing photoresist b) patterning photoresist c) Ti e-beam deposition d) photoresist stripping e) RIE etching f) Stripping away Ti

3.3.2 Laser ablation

A green-spectrum laser was scanned across a carbon xerogel to create parallel trenches. At each trench the laser was scanned multiple times until the desired trench depth was obtained. The laser used was a PHAROS 1030 nm laser with a second harmonic generation (SHG) module that converted the emitted beam to 515 nm (Figure 3.4). The pulse duration was for 250 fs, and the scan speed was set to 10 mm/s. The repetition rate was 606 kHz and the average power at the lens was 200 mW; the lens' numerical aperture was 0.4.

Figure 3.4 PHAROS femtosecond laser (Image courtesy: Light Conversion)

3.3.3 Pattern transfer using an elastomeric stamp

First, a master micro-pattern of rows of pillars was created in a SiO_2/Si substrate by dicing , creating pillars with ~25 µm broad tops, spaced at 250 µm intervals using the protocol from section **Error! Reference source not found.**. This was then coated in a 0.01 N solution of CTAB (which improves delamination of PDMS from SiO_2/Si), followed by spin-coating PDMS (Sylgard 184) in a 10:1 PDMS-oil to cross-linker ratio, cured at 90°C, then de-laminated to release the new PDMS elastomeric stamp. The PDMS is then treated with UV-ozone for 60 minutes to create surface siloxane groups, making the PDMS surface hydrophilic. This was then used to transfer the pattern to RF gel. First, the RF sol is prepared using the protocol in 3.2. Prior to curing, the stamp is then floated on the sol surface, with the pattern side in direct contact with the sol. Upon curing, the PDMS is delaminated and the RF gel is pyrolyzed (Figure 3.5).

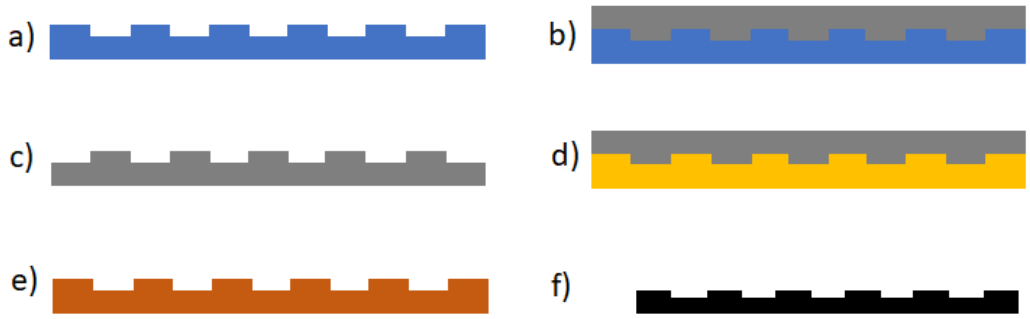

Figure 3.5 Pattern transfer schematic a) Diced SiO_2/Si wafer b) Spin-coating PDMS c) Cured PDMS stamp d) floating stamp on RF sol e) De-laminated RF gel f) Pyrolyzed pre-patterned xerogel

To eliminate the surface 'skin', the resulting xerogel was exposed to oxygen-plasma RIE at 300 W RF-power, 200 mTorr working pressure and 10 sccm O_2 flow rate, for 5 minutes.

3.3.4 Dicing saw

The ADT 7100 Provectus dicing saw can cut features in the 10s of microns range automatically based on the input parameters (Figure 3.6**Error! Reference source not found.**). As the blade rotor rotates at 30,000 RPM and the blade itself is impregnated with abrasives, the cutting is very smooth and consistent, hence brittle materials like Si, SiO_2 and carbon can be cut or patterned without fear of breaking.

Figure 3.6 ADT 7100 dicing machine (Image courtesy: University of Michigan)

In this thesis blades with ~200 µm width (ADT 00777-8006 QKP Opt Si), which can cut into the substrate up to 300 µm depth were chosen. The feed rate was 1.3 mm/s to ensure smooth and even cuts, and the trenches were cut to a depth of 150 µm. Unless otherwise mentioned, the substrate was fed in one direction to create parallel prisms. The index (distance between cuts) was chosen to ensure a prism width of 25-30 µm.

3.4 Material characterization

Optical microscope images were obtained using an Olympus SZX7 stereo microscope. Scanning Electron Microscopy was carried out using a Scanning Electron Microscope equipped with a Field Emission Gun (SEM-FEG) (JEOL JSM7600F). Energy-dispersive X-ray spectroscopy was performed with the SEM-FEG EDX module. Xerogels were outgassed under 10^{-3} Torr vacuum overnight prior to SEM imaging. Profilometry was carried out with a Dektak 150 stylus profiler with a 12 µm probe.

3.4.1 SEM detectors used

Three detectors were used: the SEI detector provides better resolution and images to greater depths in the xerogel substrate. The LEI detector provides a topographical view of the substrate, typically lower incident voltages are used (2 kV). The Low Angle Back-scattered Electron (LABE) detector module where the higher molecular weight components appear brighter than the lower molecular weight components. The LABE detector detects the low-angled back-scattered electrons, which are low angle electrons produced by elastic scattering of the incident electron beam due to interaction with the sample atom; since the degree of scattering is correlated with the atomic number of the specimen, this permits a topographical chemical analysis of the sample [33].

3.5 Emission testing

The xerogel was prepared prior to emission testing by outgassing in a 10^{-3} Torr vacuum and 1-Ethyl-3-methylimidazolium bis(trifluoromethylsulfonyl)imide ([EMIM] [TFSI]) was dropped until no more could be absorbed into the pores.

The emission testing setup used a Bio-Rad high voltage power supply providing DC accelerating voltage (henceforth referred to as V_{input} or input voltage) connected in series to the xerogel-accelerating plate system and a 50 kΩ sensing resistor (actually 2 100 kΩ resistors connected in parallel to increase the power rating) (Figure 3.7 a). An oscilloscope (Agilent Infiniium, shown in the circuit diagram as a voltmeter) was connected in parallel to the sensing resistor using a 100:1 sensing probe rated to 2000 V_{DC}. The xerogel setup consists of a xerogel separated from an accelerating electrode using a 130-170 μm glass cover slip. The accelerating electrode may be a bare copper plate, referred to as Xerogel Setup A (Figure 3.7 b), or a bare, unpatterned, and polished xerogel in contact with a bare copper plate, referred to as Xerogel Setup B (Figure 3.7 c).

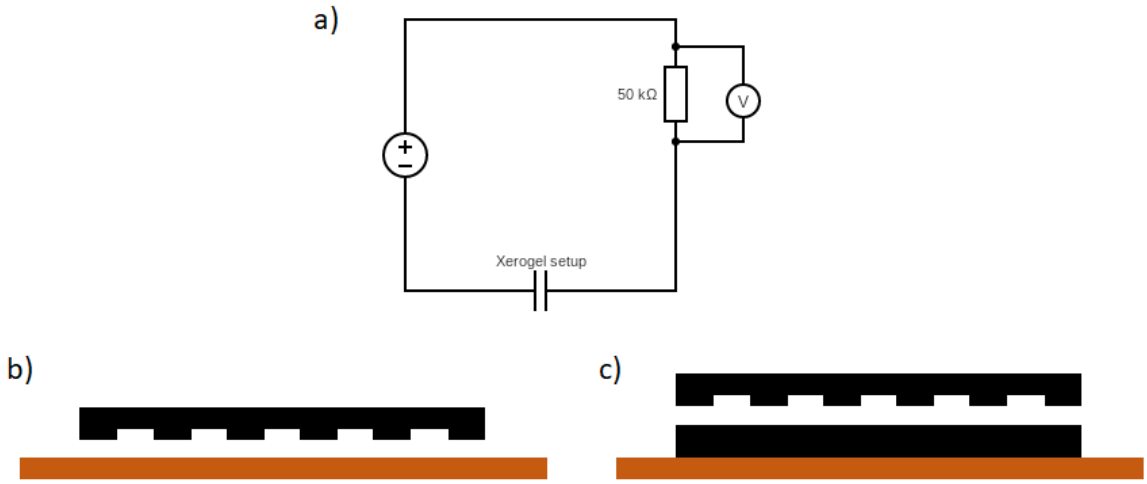

Figure 3.7 Electrical testing setup a) circuit diagram b) initial xerogel setup using only copper plate as accelerating electrode (Xerogel Setup A) c) improved xerogel setup using xerogel with no ionic liquid in contact with copper plate as ionic liquid (Xerogel Setup B); the xerogels are in black, while the copper plate is in orange. Spacing between the patterned xerogel and accelerating electrode is maintained with a 130-170 μm cover-slip (not shown in schematic)

CHAPTER 4 RESULTS AND DISCUSSION

4.1 Xerogel porosity

Polishing with a 6 µm grit diamond polishing pad removes the surface skin, yielding a jet-black coloured surface (Figure 4.1 e). Upon visualization under SEM, the polished substrate looks porous, with most pores appearing to be in the 5 µm diameter range; the 'skin' is not as porous and must be eliminated prior to patterning. Under SEM imaging, the skin appears to have nanometer-size pores, which are not as ideal for ionic liquid emission as the micropores that are revealed once the skin has been polished away (Figure 4.1 a, b, c vs d)

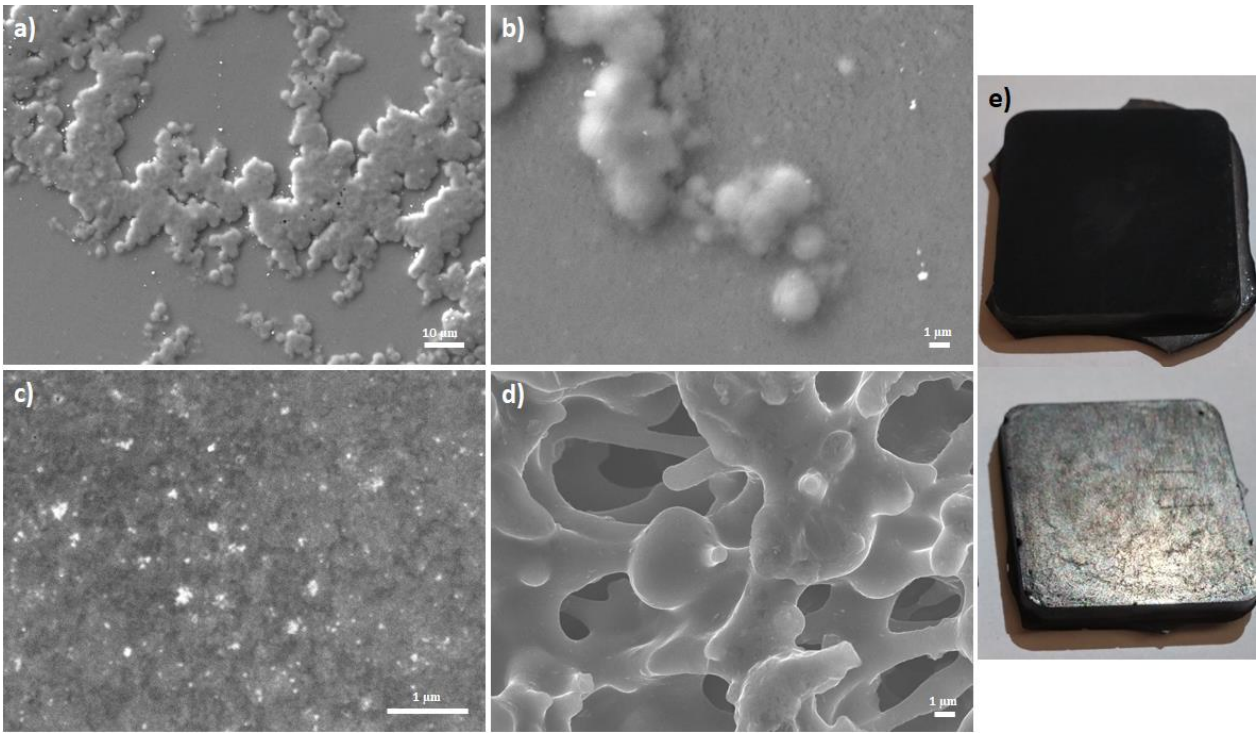

Figure 4.1 Unpolished vs. polished xerogels a) unpolished (scale bar 10 µm) b) unpolished close-up (scale bar 1 µm) c) unpolished high magnification (scale bar 1 µm) d) polished (scale bar 1 µm) e) polished vs. unpolished xerogel

The dust collected after polishing was imaged to see if the individual particles were also porous, for application in carbon electrodes or supercapacitors, as a replacement for activated carbon

electrodes. Xerogels are attractive for this purpose because porosity can be tuned by changing the chemistry. From inspection of SEM images, the powder does not appear to be porous, and the surface area is close to the geometric area (Figure 4.2 a, b).

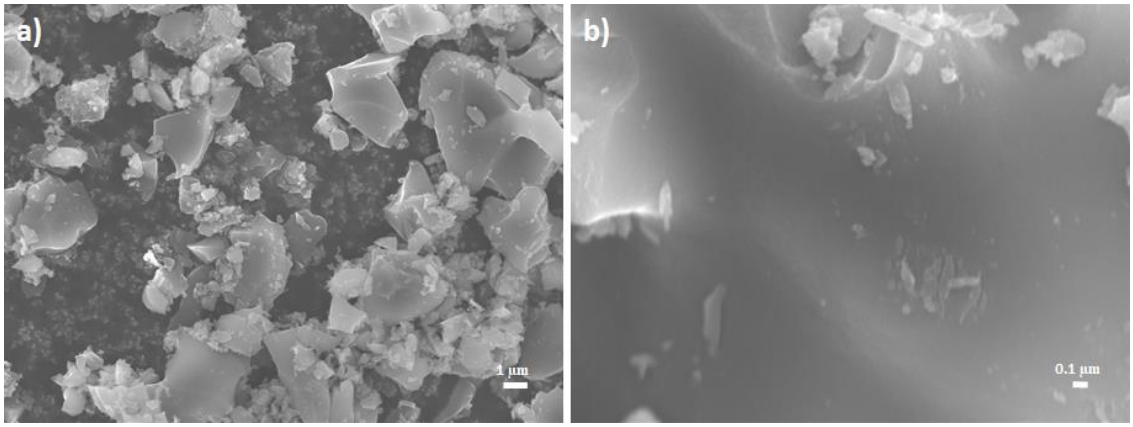

Figure 4.2 Xerogel powder a) overview (scale bar 1 µm) b) close-up of single fragment (scale bar 0.1 µm)

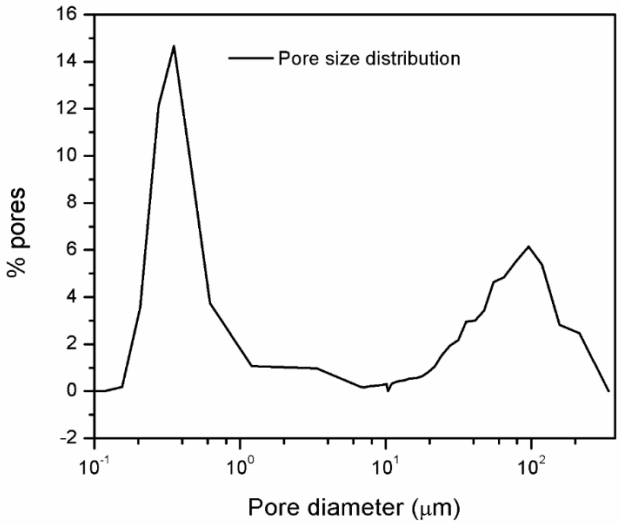

Figure 4.3 MIP of xerogel, showing macroporous nature of xerogel

From MIP, the xerogel is macro-porous, with 2 peaks; 40% of the pores are in the relatively narrow range of 200-600 nm whereas 45% are in the range of 30-215 μm (Figure 4.3). However, SEM images (Figure 4.1 d), show a cage-like structure with pores in the 2-5 μm range. Therefore, on the one hand, while the MIP confirms the macro-porous nature of the material, the anomalous results show the limitations of this method. Reasons for the anomaly include the assumption that the pore volume is cylindrical, the need to pulverize the material prior to testing, which may cause the pores to collapse. The large pore volumes could come from the spaces between the individual particles.

In conclusion, the material is in fact porous and ideal as a conductive emitter material for electrospray micro-thrusters.

4.2 Microfabrication results

4.2.1 Reactive ion etching

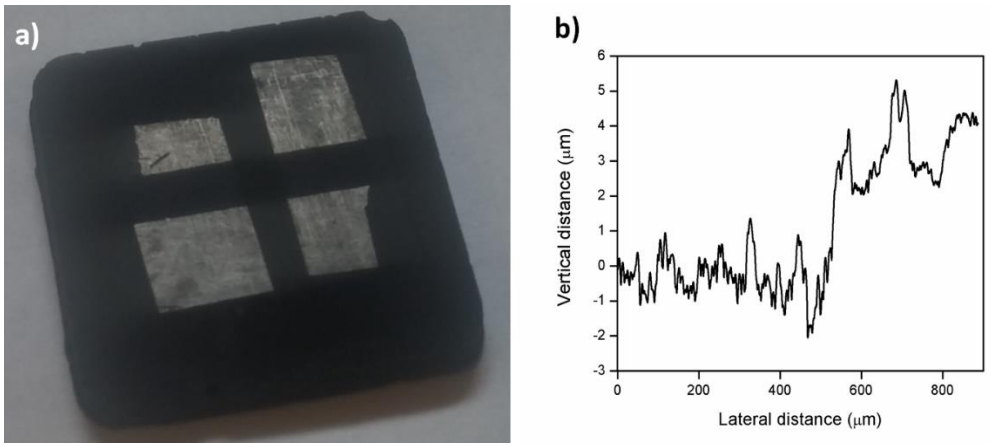

Figure 4.4 RIE xerogel a) picture of unetched (shiny) vs. etched areas b) profilometry of etched vs. non etched regions (4 μm depth)

In carbon xerogels, plasma likely reacts with carbon and create carbon dioxide or carbon monoxide, etching away material in the process. After 10 minutes, the plasma etches away about 4 μm material (Figure 4.4). This etch rate can change depending on the exposed surface. This looked promising, as multiple xerogels can be patterned simultaneously, even though the etch rate is only 400 nm/min. Hence, to pattern carbon xerogels, a pattern from a photomask was transferred to a 2.5 μm thick photoresist that was spin-coated onto the xerogel surface, which was then developed. Upon exposure to plasma, the photoresist etches away quicker than carbon, hence a target depth of 100 μm is unfeasible. Even using a polyimide tape as a rough mask does not work, as after 45 minutes of etching (or 17 μm etched away) the tape is etched away.

Hence the metal masking strategy was explored (Figure 3.3). For the first attempt the liftoff was carried out; however, from a visual inspection, it seemed that all metal was stripped away. However, under SEM imaging there appear to be metal particles, both on the metal mask and on

the exposed xerogel (Figure 4.5 a, c). Within the exposed xerogel, there are filaments of material which could correspond to the metal adhering to the walls of the xerogel micropores, whereas on the metal mask, due to the greater concentration of metal, the metal appears as spherical particles superimposed on structures which follow the topography of the bare xerogel (Figure 4.5 b, d). The LABE detector shows the metal to be localized to the surface of the xerogel (Figure 4.5 d).

However, from the EDX spectroscopy, it appears that the liftoff process was indeed successful, as no titanium is detected (Figure 4.5 b). The major components are carbon and oxygen with significant iron and fluorine contamination from the RIE chamber. The metal mask area is mostly composed of titanium, with some oxygen and carbon, with fluorine contamination. The latter result is expected, many RIE processes use fluorine-containing gases as etchants; the former result requires some explanation for the white filamentation seen in Figure 4.5 c and d).

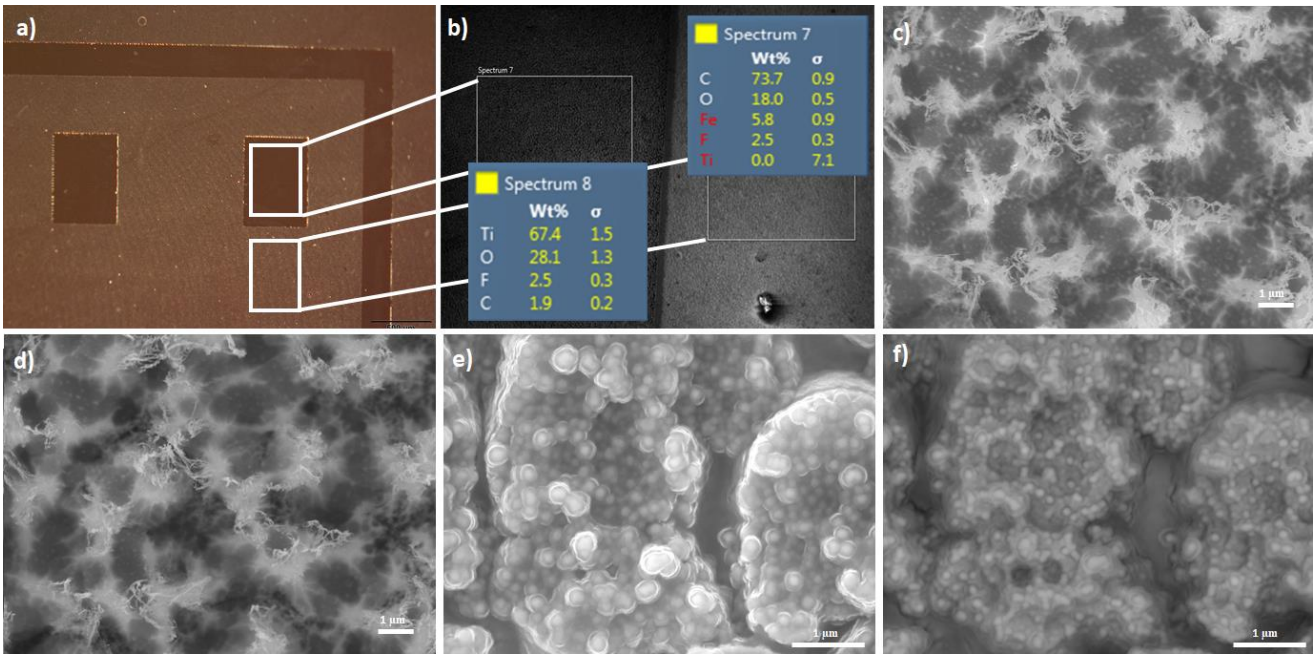

Figure 4.5 Post-liftoff metal masked RIE a) optical image b) EDX of inside pattern (left) and metal mask (right) c) inside square (scale bar 1 µm) d) Inside square LABE (scale bar 1 µm) e) Outside square (scale bar 1 µm) f) Outside square LABE (scale bar 1 µm)

In the second attempt, the liftoff was not performed after metal deposition and the xerogel was subjected to O_2-plasma etching. The metal on the bare xerogel turned green and under SEM imaging appears very similar to the aggregates formed in the liftoff process (Figure 4.6 e, f, d; Figure 4.5 e, f). The metal on the square pattern is a silvery colour, and under SEM imaging appears as solid chunks with circular aggregates at points (Figure 4.6 a, c, d).

The explanation for the green colour is not obvious, because EDX analysis shows that both the silvery and green colour areas are composed of titanium and oxygen (from the reaction with oxygen radicals produced by the O_2 plasma) (Figure 4.6 b). One possible explanation could be that on the bare xerogel, due to the metal being deposited within the carbon pores, the amount of metal available for oxidation is much lower than on the photoresist, and hence the thickness of the oxide is lower as well. Alternatively, all titanium may have been oxidized and only a thin layer of oxide is visible on the surface. The fluorine is most probably due to contamination from the other fluorine-based etching processes within the RIE chamber.

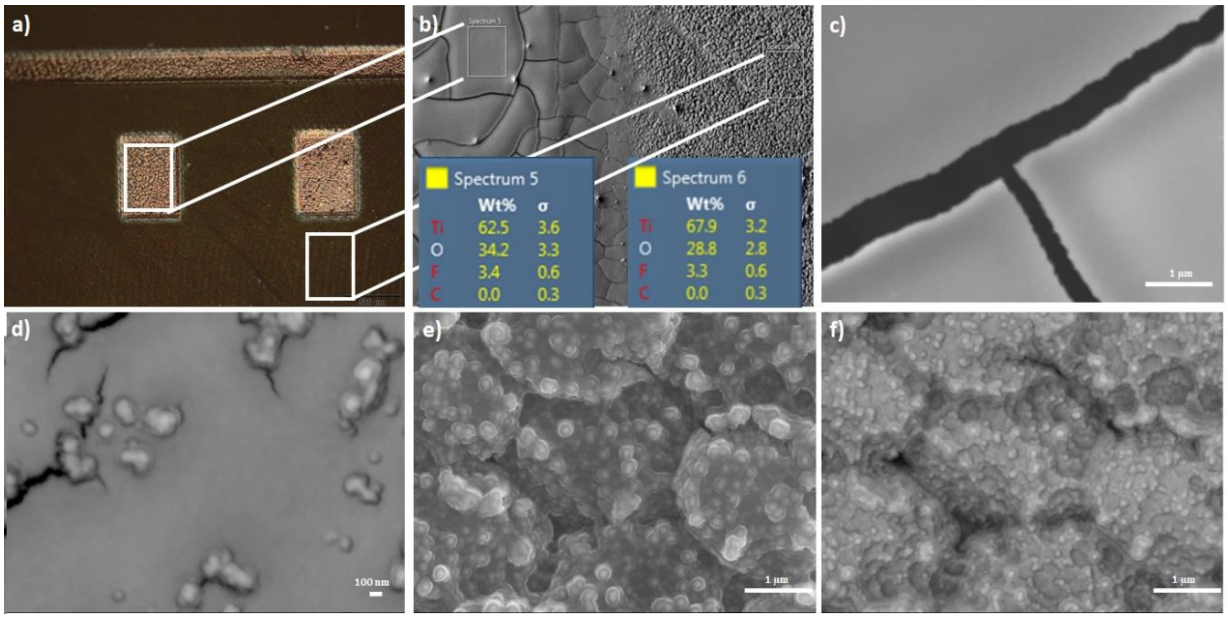

Figure 4.6 Non-liftoff metal masked RIE a) optical image b) EDX of inside pattern (left) and metal mask (right) c) inside square (scale bar 1 µm) d) Inside square LABE (scale bar 1 µm) e) Outside square (scale bar 1 µm) f) Outside square LABE (scale bar 1 µm)

4.2.2 Laser ablation

Profilometry indicates that the laser etched 20 away pillars of 20 µm height in 50 µm lateral distance intervals (Figure 4.7 f) measured by profilometry, which is lower than the peaks from Lozano's group. However, the profilometry needle tip is 12 µm in diameter, potentially wider than the trench bottom, which could imply that the bottom of the trench hasn't been reached, and it could be deeper than measured. This can be mitigated by increasing the spacing between the pillars. This will also permit the creation of pillars with tapering sides that will support taller pillars. SEM imaging appears to confirm the pillar depth measured by profilometry; even high magnification cannot reveal the bottom of the trench.

Of greater concern is the reduction in the porosity. Whereas the un-patterned, polished substrate had pores ranging from 100s of nm to 10s of µm, the ablated sample has maximum pore size on the surface of 100s of nm (Figure 4.7 b, c, d and e). This may indicate that the laser fused the pores in the xerogel such that the sizes have reduced, or the carbon dust from the ablation process may have re-deposited on the sample. Evidence for the latter could be seen in the 1000x view where the pillar on the right appears to have overhangs on the left side. (Figure 4.7 a). One possible explanation could be that the vaporized carbon particle redeposited and because of insufficient heat dissipation from the material sintered into a relatively non-porous material.

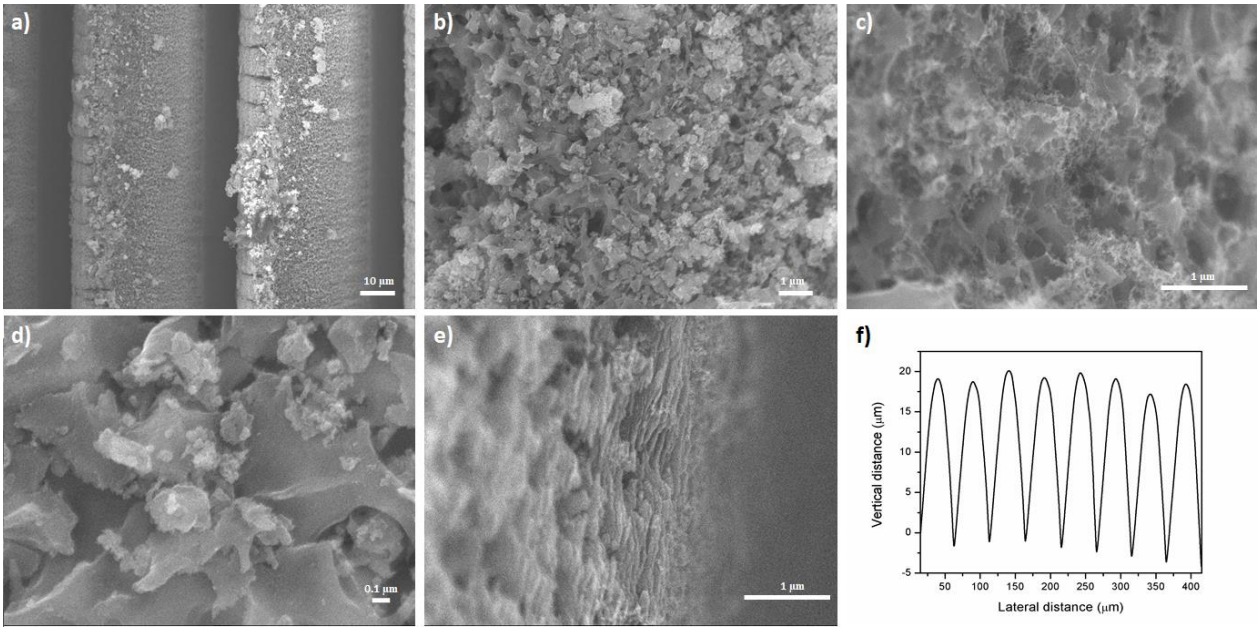

Figure 4.7 Femtosecond laser ablation (a) Overview (scale bar 10 µm) (b) pillar top (scale bar 1 µm) (c) trench wall (scale bar 1 µm) (d) pillar top close-up (scale bar 0.1 µm) (e) second trench wall (scale bar 1 µm) (f) Profilometry of ablated trenches

4.2.3 Pattern transfer using an elastomeric stamp

The samples were imaged under SEM (Figure 4.8). The images show that the porosity of the material is preserved, the non-porous material is PDMS residues from imperfect de-moulding. This latter is clear from the non-charging nature of the residues, appearing as bright particles against a dark-non charging carbon matrix. Dahiya et. al. proposed using a quaternary ammonium fluoride in a hydrophobic and aprotic solvent to completely eliminate the residues [34]. This may be a useful strategy for future research.

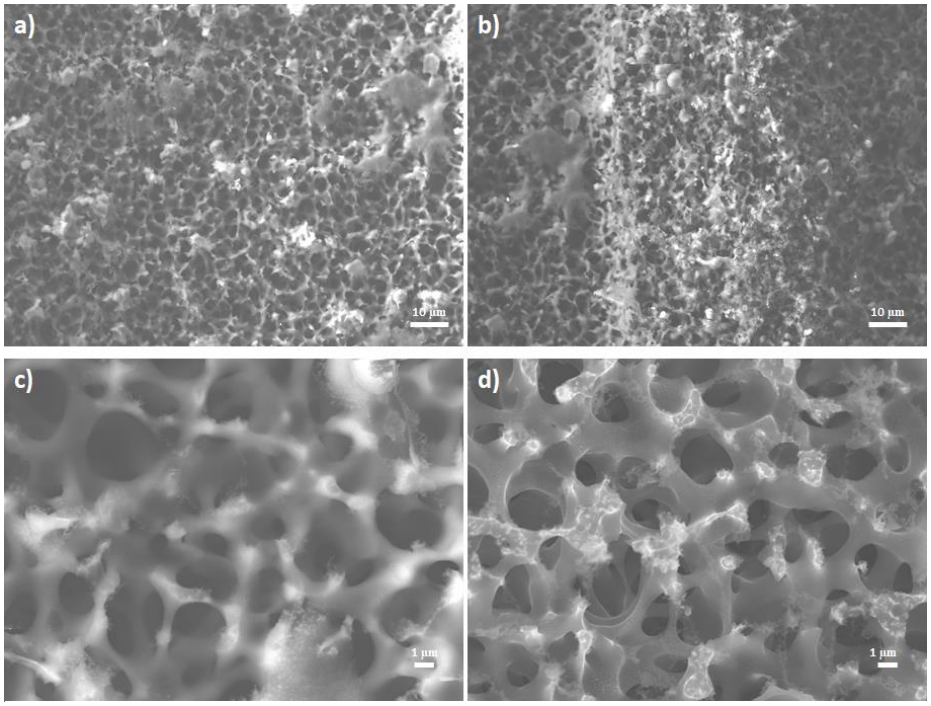

Figure 4.8 SEM of pre-patterned emitter prisms a) pillar top (scale bar 10 µm) b) groove bottom (scale bar 10 µm) c) pillar top close-up (scale bar 1 µm) d) pillar top close-up with SEI detector (scale bar 1 µm)

For micro-thruster applications, compared to experiments with dicing in section 4.2.4, it was clear that this method does not confer any added benefit in terms of speed or resolution but may be useful where pattern miniaturization that takes advantage of the volume reduction due to pyrolysis is required. Due to the predictable shrinking of the xerogel precursor during pyrolysis, this could enable the fabrication of smaller features than is possible from dicing alone.

4.2.4 Dicing

From SEM images, the pores in the xerogel appear as voids in a carbon framework, which is consistent over the entire xerogel. The pore sizes are in the 1-5 µm range. As expected, the carbon bulk material is not charging, except for the edges of most walls, and in some cases the entire material surface. This implies that the material is conductive, due to the ready absorption of electrons into the material, this is confirmed by checking the resistance, which is in the 1-4 Ω range.

Contrasting this with the laser ablated material (Figure 4.9 e), the latter does not show any sign of charging at the ablated regions, seen from the absence of bright charging regions, caused by electrons scattering from non-conducting regions.

This methodology was attractive compared to laser ablation because the process is rapid (~15 minute per wafer after process optimization compared to more than 1 hour for laser ablation) and from the SEM images, does not damage the pores, because the heat transferred between the blade and carbon xerogel is insufficient to cause the pores to close up (Figure 4.9 b, c, d).Comparing xerogels without and with ionic liquid, the ionic liquid clearly occupies the pores (Figure 4.9 e and f). The bright edges appear to be the xerogel walls; under incident potential, the ionic liquid appears to be flowing (Figure 4.9 f). Hence, for emission testing, all xerogels were patterned with the dicing saw to create parallel prisms, spaced 250 µm apart with a peak width of 25-30 µm (Figure 4.9 a), unless otherwise mentioned.

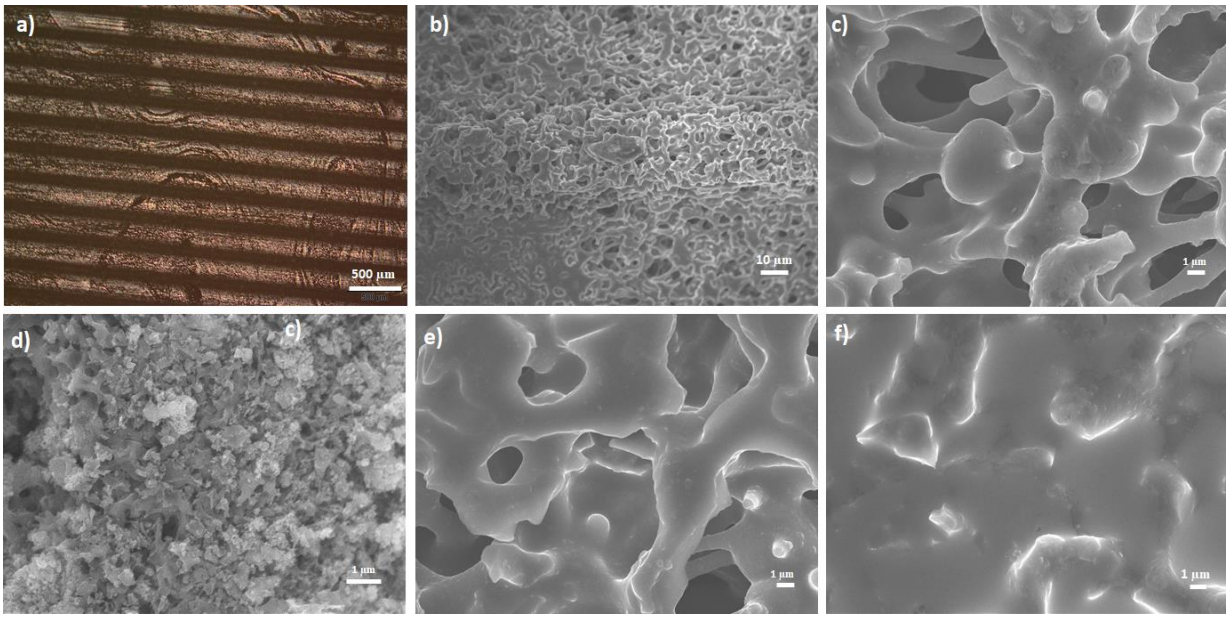

Figure 4.9 Diced overview a) optical microscopy b) pillar top (scale bar 10 µm) c) pillar top close-up (scale bar 1 µm) d) pillar top laser ablated for comparison (scale bar 1 µm) e) trench bottom close-up (scale bar 1 µm) f) xerogel loaded with ionic liquids [EMIM][TFSI] (scale bar 1 µm)

4.3 Emission testing of patterned xerogels

The patterned xerogels were incorporated into the emission setup (described in section 3.5). The goal of these experiments is to observe the electrospray of the ionic liquid from the carbon xerogel, seen as current on an oscilloscope.

4.3.1 Determining 'safe' maximum V_{input}

To determine the maximum V_{input} in ambient air before air breakdown arcing events occur, a polished and unpatterned xerogel with no ionic liquid was assembled into Xerogel Setup A (Figure 3.7 a). The input voltage was ramped to 300, 350, 500, 700 and 900 V_{DC} and oscilloscope measurements recorded. For each measurement, input voltage was returned to 0 V_{DC} before proceeding with the next measurement.

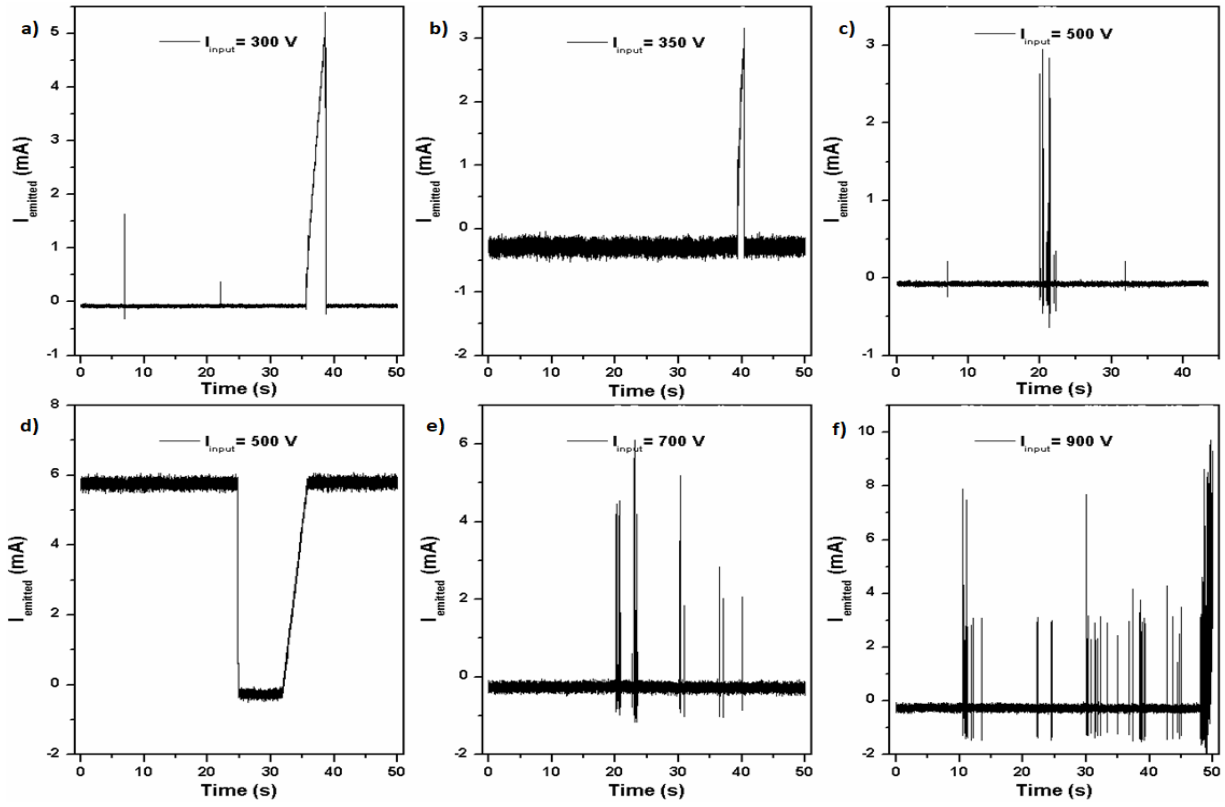

Figure 4.10 Emission scans on unloaded xerogels at V_{input} a) 300 V b) 350 V c) 500 V d) 500 V with short circuit e) 700 V f) 900 V.

At 300 V_{DC} and 350 V_{DC}, there are random breakdown peaks, spaced widely apart, however, for the most part, there is no detected current, as expected (Figure 4.10 a, b). At 500 V_{DC} some arcing spikes begin to appear, which seem to indicate the air breakdown beginning (Figure 4.10 c). There seems to be a short circuit event during the test at 500 V_{DC}, seen as a continuous 6 mA current, which was later discovered to be due to carbon debris from the air breakdown event, which deposited on the copper plate, gradually bridging the gap between the xerogel and copper plate and hence a low-resistance path for the current (Figure 4.10 d). Finally, at voltages greater than 700 $V_{DC,}$ the arcing events become more frequent and air discharge can be visually observed as arcs. Hence, the experiments were carried out at V_{input} below 500 V_{DC} (450 V_{DC} for safety).

4.3.2 Xerogel Setup A

A patterned xerogel, outgassed and loaded with ionic liquid was assembled into Xerogel Setup A and incorporated into the emission testing circuit (Figure 3.7 a, b). An input voltage of 280 V_{DC} was applied with a 2 mA and 1 W safety constraint. It was observed that initial emission spikes occurred a few minutes from the start of the experiment (Figure 4.11 a). Compared to the arcing spikes, which are in the mA range, emission spikes due ionic liquid ejection are in the μA range; further, the latter occur at much lower input voltages.

The spikes continuously occur over the next 80 minutes; however, the ionic liquid on the copper accelerating plate begins to accumulate over a 15-minute period, causing the distance between the electrodes to reduce, causing air breakdown arcs and ultimately a short circuit as the ionic liquid layer is as thick as the xerogel-copper place spacing. Hence, the experiment must be paused, and the copper plate must be cleaned, and if necessary, lightly sanded, wherever there is decomposed ionic liquid from the breakdown events.

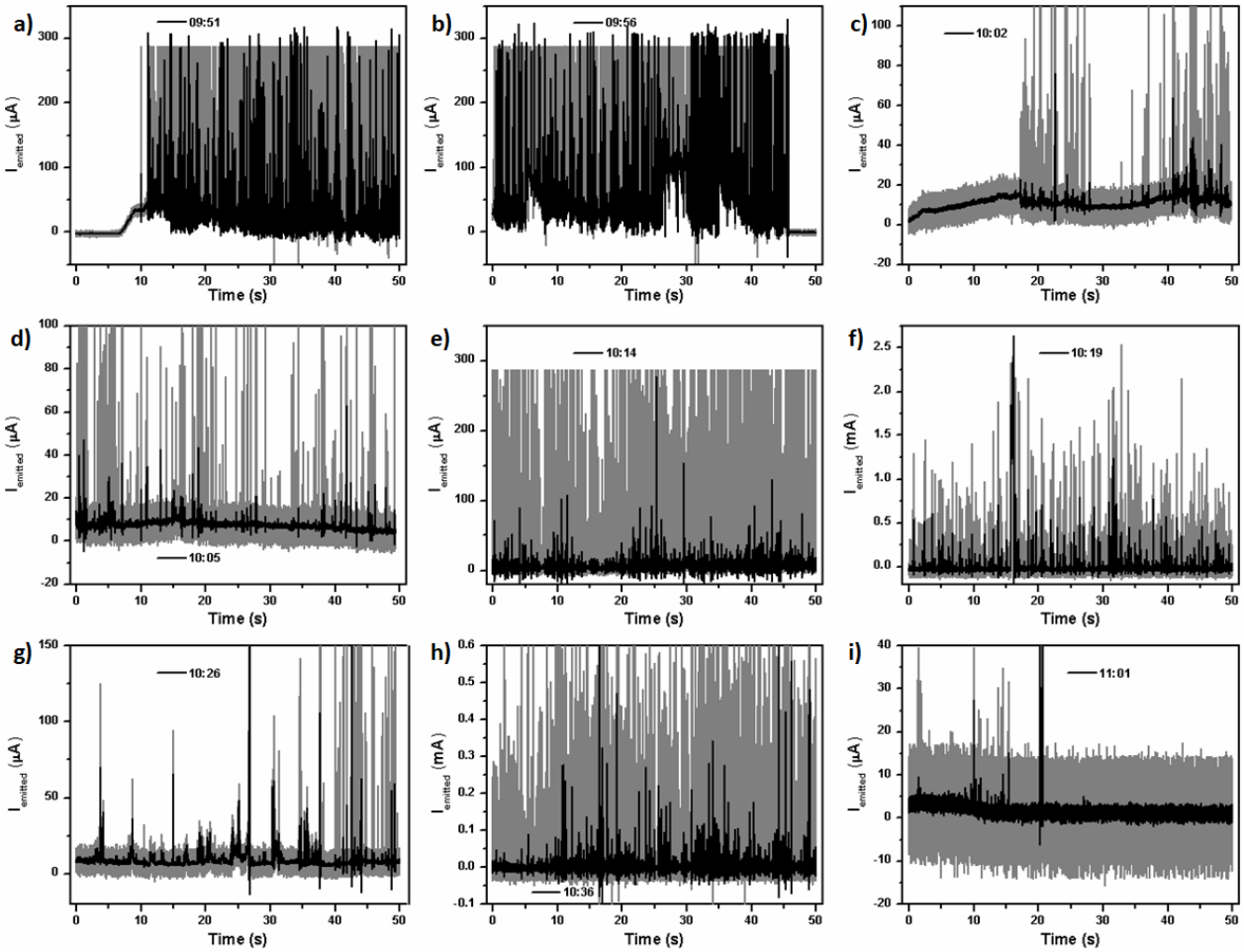

Figure 4.11 Initial oscilloscope experiments at input voltage of 280 V_{DC} at times (hh:mm) indicated in legend using Xerogel Setup A. The grey-shaded area is the raw signal from the oscilloscope, and the black-shaded curve is the signal processed with a smoothing function.

The emission peak frequency reduces (Figure 4.11 c, d), only to pick up a few minutes later (Figure 4.11 e, f). However, after 80 minutes the emission spikes reduce and stop completely (Figure 4.11 i). Courtney indicates that the emission spikes are analogous to noise and consist of random emissions of species from the porous material, as opposed to continuous emission, seen as a gradual increase in the baseline current over time [5].

The grey-shaded area in the plots is the raw data from the oscilloscope, which must be processed by averaging out the points to eliminate noise from the voltage source. By processing the input signal with a smoothing function that reduces noise, like the Savitzky-Golay filter over 50 points, a more coherent and meaningful result can be observed: the black curves in the plots. The Savitzky-Golay filter relies on a method called convolution, where one function (in our case the raw data) is modified by the addition of a second function. This other function is obtained by using the least-squares method over 50 data points to fit these into a low-order polynomial. As the second function is applied on the raw data, a new (convoluted) curve is formed which is (relatively) free of noise. Hence, unless otherwise mentioned, all further oscilloscope data in the thesis is presented after signal processing.

This confirms that due to the constant reducing of the inter-electrode distance over 15-minute intervals, the continuous output is very low, close to 0 μA, and the emissions mostly are in the form of discontinuous ionic liquid ejection or ‘noise’.

To estimate the damage to the pore structure during electrical testing, the input voltage was increased to 700 V_{DC} where breakdown events were observed. The SEM images before and after input voltage was applied appears to show that the electrical testing has fragmented the pore walls (Figure 4.12, Figure 4.13). The damage is a bit more clear in the xerogel pillar (Figure 4.12 c, d vs. Figure 4.13 c, d). As ionic liquids cannot be easily eliminated from the gel besides complete exhaustion of the liquid, it is hard to determine the exact nature of the damage to the pores.

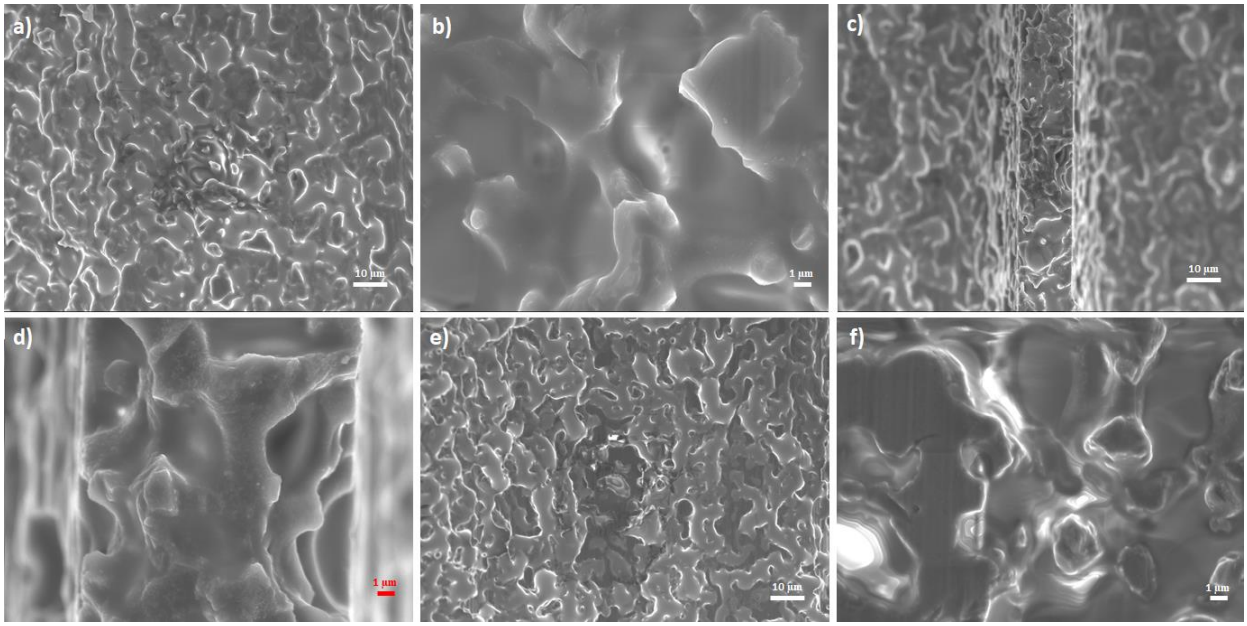

Figure 4.12 Pre-electric test diced with [EMIM][TFSI] trench bottom a) overview (scale bar 10 µm) b) close-up (scale bar 1 µm); pillar top c) overview (scale bar 10 µm) d) close-up (scale bar 1 µm); trench bottom at 5 kV e) overview (scale bar 10 µm) f) close-up (scale bar 1 µm)

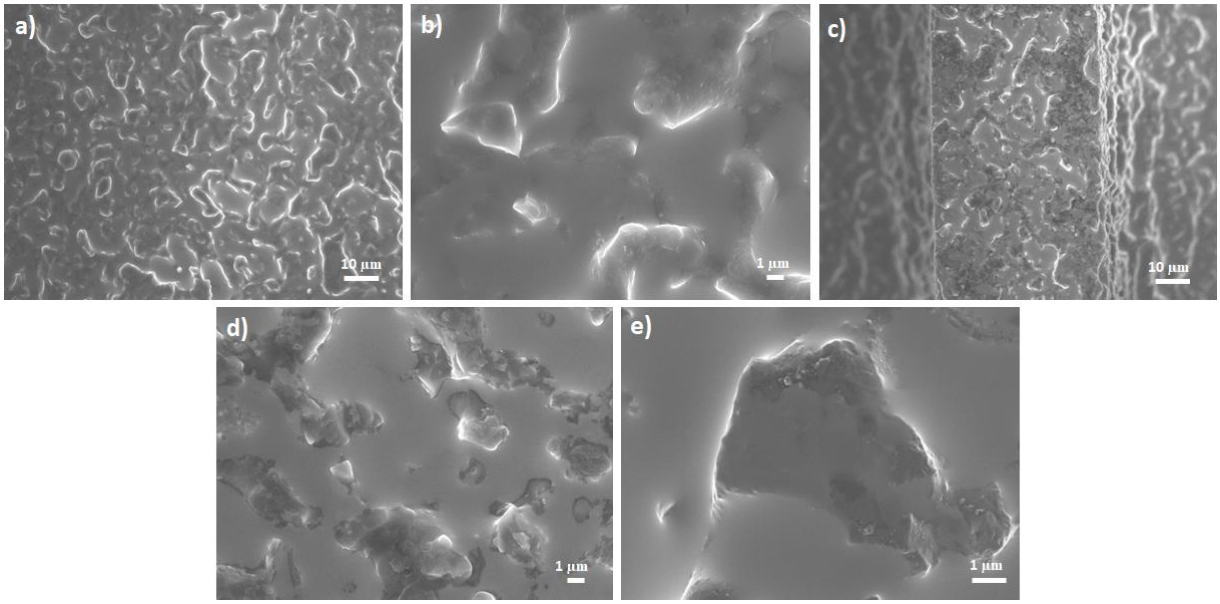

Figure 4.13 Post-electric test diced with [EMIM][TFSI] trench bottom a) overview (scale bar 10 µm) b) close-up (scale bar 1 µm); pillar top c) overview (scale bar 10 µm) d) close-up (scale bar 1 µm) e) at 2 kV (scale bar 1 µm)

4.3.3 Xerogel Setup B

To reduce the down-time from cleaning the copper plate, it was decided to use a bare, un-patterned xerogel as an accelerating electrode that can readily absorb ionic liquid, hence maintaining a constant xerogel-accelerating electrode distance for longer time periods, A patterned xerogel, outgassed and loaded with ionic liquid was assembled into Xerogel Setup A and incorporated into the emission testing circuit (Figure 3.7 a, b). This experiment was of much longer duration, about 100 minutes, where the emission spikes continued, and the baseline current kept increasing. This latter fluctuated between 100-300 μA, indicating that the inter-electrode distance is maintained throughout the experimental duration, and that the emissions are seen as the desired baseline current or continuous emission, as opposed to the undesired emission spike 'noise' (Figure 4.14). Hence, all further emission tests will be carried out using Xerogel Setup B.

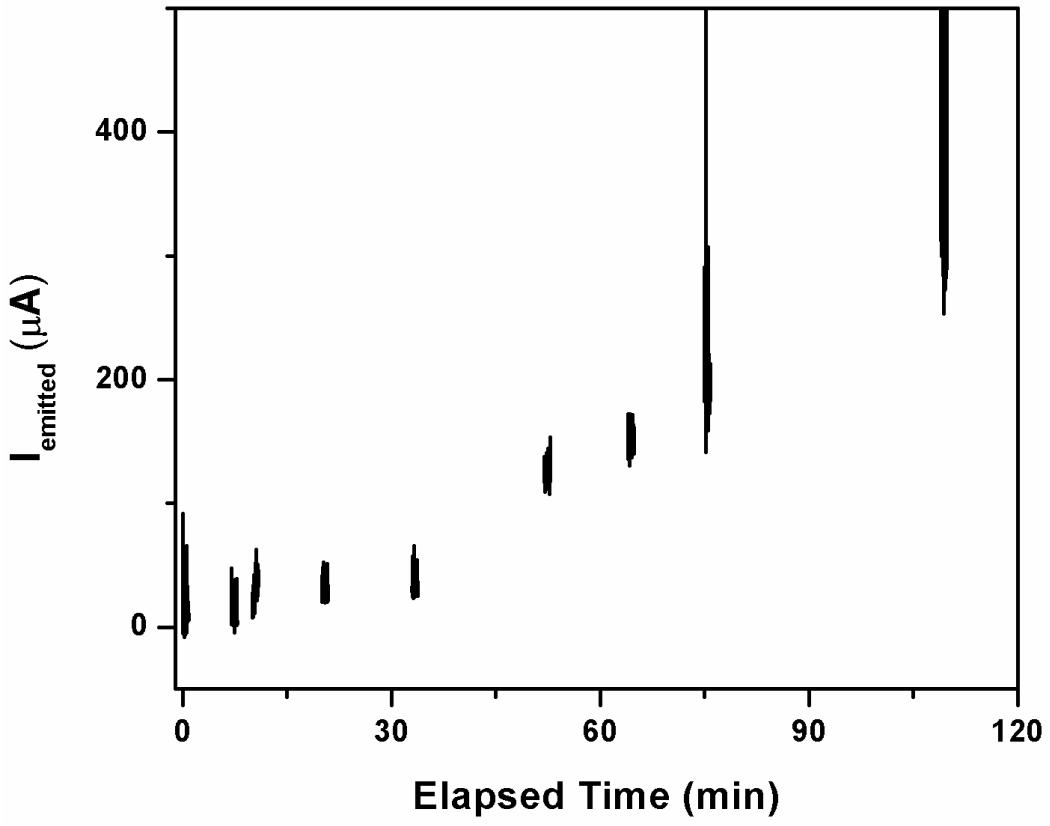

Figure 4.14 Initial oscilloscope experiments at input voltage 280 V_{DC} using unloaded xerogels as accelerating electrodes to wick away ejected ionic liquid, i.e. Xerogel Setup B

4.3.4 Grid patterned xerogel

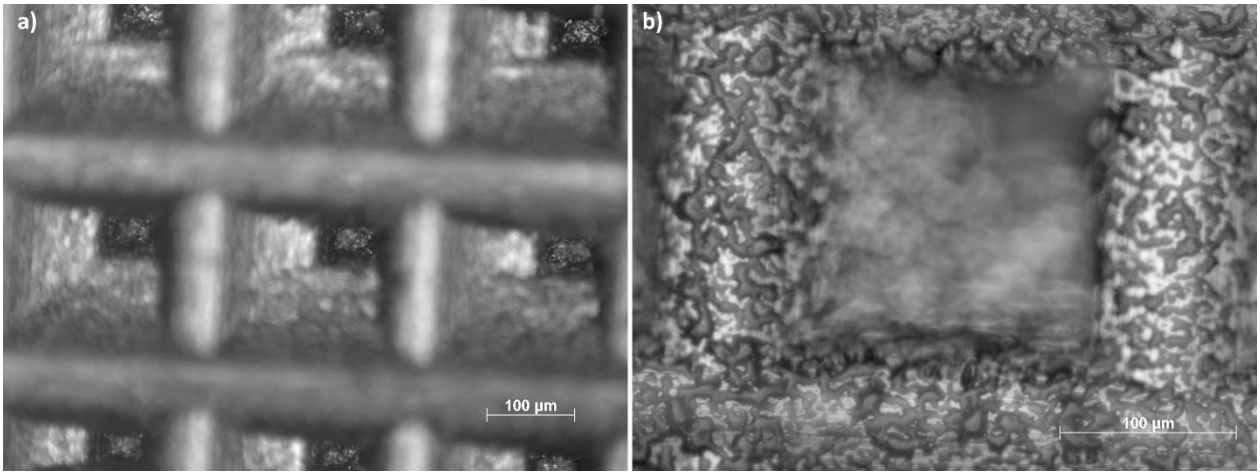

Figure 4.15 2-D grid patterned xerogel a) xerogel tips (scale bar 100 µm) b) xerogel bottom (scale bar 100 µm)

To understand the impact of different patterns on the emission characteristics, a grid patterned xerogel, was loaded with ionic liquid, assembled into Xerogel Setup B, and incorporated into the electrical circuit. The grid patterning was achieved by dicing the xerogel in one direction and then rotating the gel and dicing it in the 90° angle, achieving a grid pattern at the intersection of the two dicing processes (Figure 4.15). The tips are pyramid-shaped, tapering to tips with widths of 40 µm, (Figure 4.15 a), while the pyramids are spaced about 250 µm apart, measured from one side of the bottom of a pyramid to the next (Figure 4.15 b). The emission testing was carried out an 8.5-hour period split between 3 days. After assembling the electrical setup, the voltage source was set to the desired voltage level with 2 mA and 1 W safety constraints; the input voltage was maintained for a minimum of 10 minutes before increasing, to permit initial ionic liquid emissions (if any) to commence.

Unlike the prior experiment in section 4.3.3, emissions only began at 420 V_{DC}. This may be because the second dicing process damaged some of the tips of the first dicing process, hence subtly increasing the distance between the emitter tips and the accelerating electrode. The summary of the

emission characteristics is presented in Figure 4.16. After about 50 minutes, the accelerating voltage was reduced to 280 V_{DC} due to the appearance of breakdown spikes (Figure 4.16 d), possibly indicating that the ionic liquid has reached the surface of the xerogel, enabling the emission to proceed as usual. During the experiment, the baseline current gradually decreased from a peak of 300 μA on Day 2 to 20 μA on Day 3 while the accelerating voltage was gradually increased from 280 V_{DC} to 450 V_{DC}. This indicates that the ionic liquid is gradually being exhausted and that higher accelerating voltages are required to force the ionic liquid from the bulk to the emitter tips.

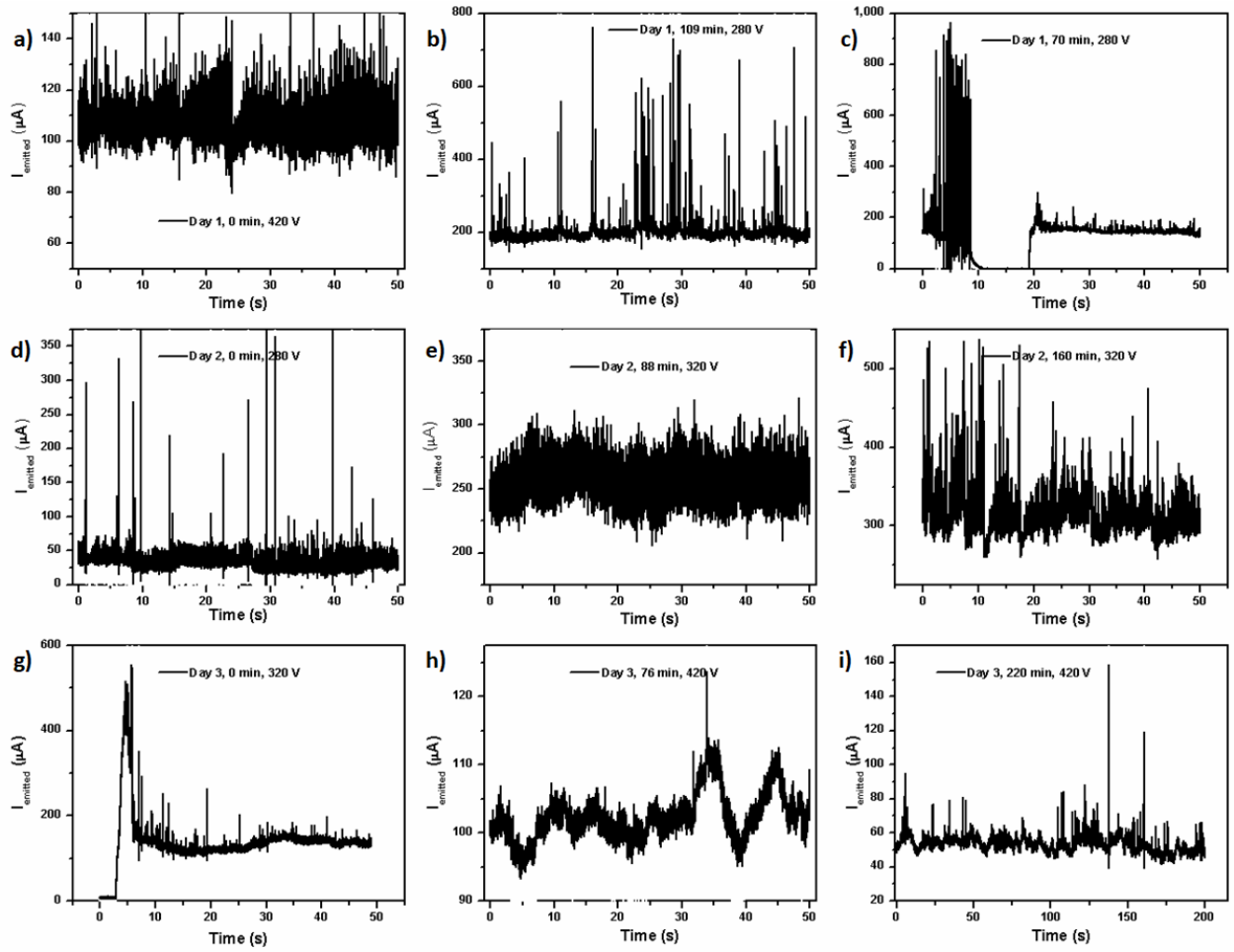

Figure 4.16 2-D emission characteristics, the legend in each figure shows the day, time in minutes and input DC voltage.

While emitter-tip damage was not studied at this point, SEM images of the 2-D grid patterned tips post-emission taken at a 45° substrate inclination showed the presence of bright regions where charging occurs at the tip peak; the SEI detector was able to contrast the regions better than the LEI detector, which shows the overall surface topography better (Figure 4.17 a, c vs. b, d respectively). However, comparing the SEI and LEI images, especially at lower magnifications, reveals the presence of particulates close to the charging region in the topographical image (Figure 4.17 b). These appear to be visually different from the substrate material.

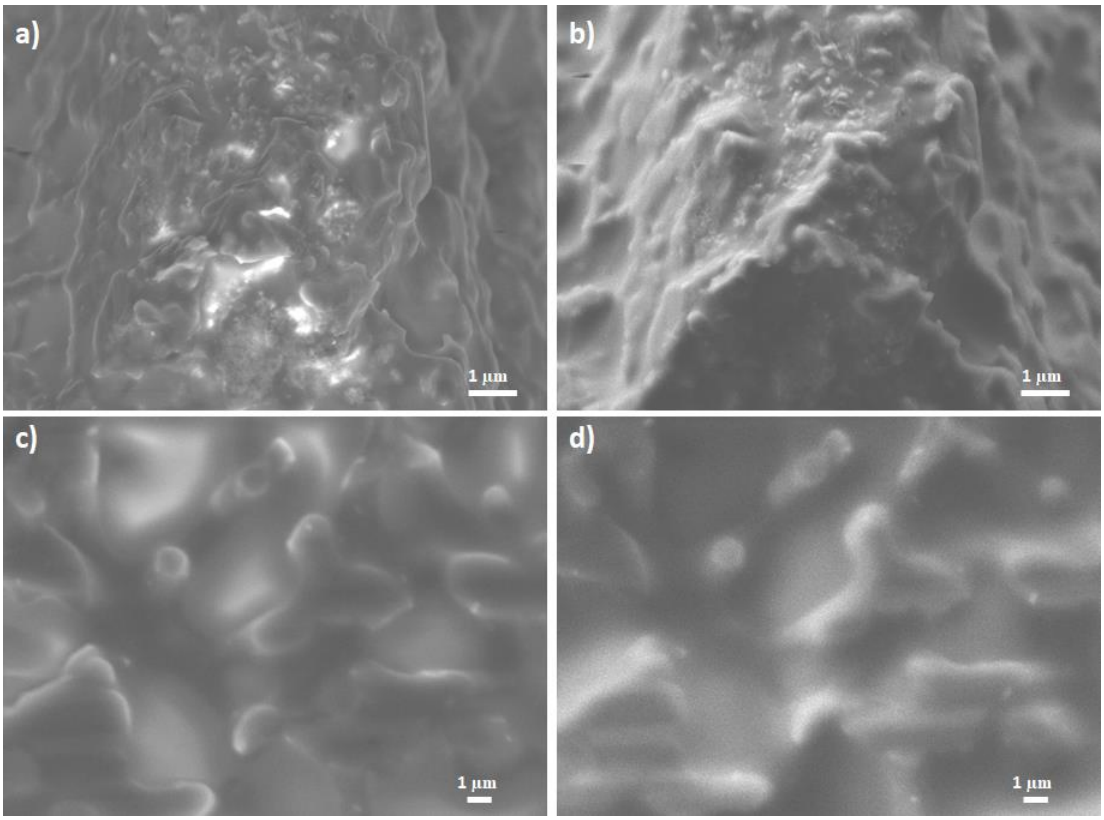

Figure 4.17 Tip of 2-D grid patterned xerogel after emission a) SEI detector (scale bar 10 µm) b) topographical image (scale bar 10 µm) c) SEI detector close-up (scale bar 10 µm) d) topographical close-up (scale bar 10 µm)

The contrast is especially visible with the LABE detector, which shows that the charging region is more widespread than can be detected with the LEI detector (Figure 4.18 a and b vs. c). The

charging is spread out across the peak, and a close-up of the LABE image shows that the bright region is a ‘field’ of bright charging particulates, surrounded by a charging region, probably extremely fine particulates, of electrochemical reaction breakdown products (Figure 4.18 b). The chemical analysis of the bright charging regions shows the presence of materials other than carbon, including nitrogen, oxygen, calcium and zinc (Figure 4.18 d comparing Spectrum 3 vs. Spectrum 4 and 5). The nitrogen and oxygen could be from the ionic liquid, whereas the metal content may be contamination from the environment. SEM of a different tips in Appendix B shows similar results, with breakdown products from unwanted electrochemical reactions.

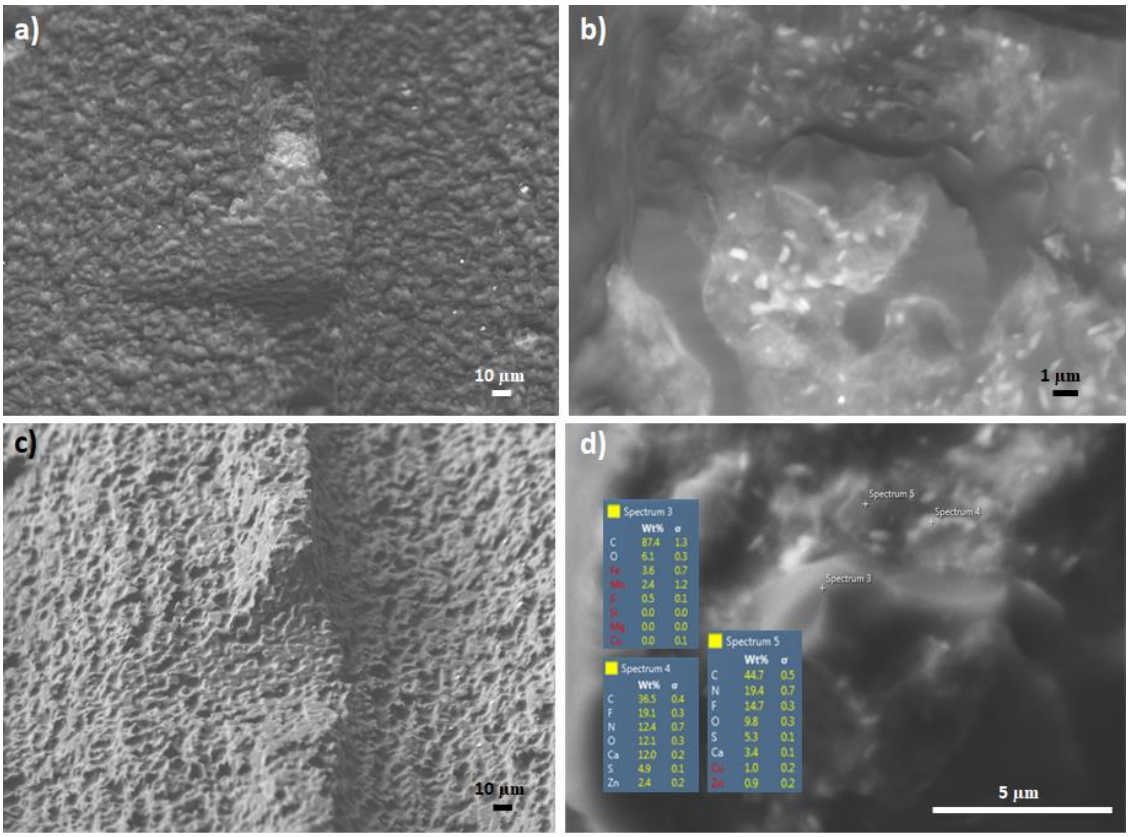

Figure 4.18 2-D patterned post-emission SEM, site 1 a) LABE detector (scale bar 10 µm) b) LABE detector close-up (scale bar 1 µm) c) topographical image with LEI detector (scale bar 10 µm) d) EDS chemical analysis (scale bar 5 µm)

Brikner and Lozano indicated that electrochemical reactions could occur at the tip surfaces, which could produce electrochemical breakdown products and damage emitter tips.[35] This is because of the formation of an electrochemical double layer (EDL) at the liquid-emitter interface, which under applied potential is destabilized, leading to the accumulation of ions on the emitter tips, leading to potentially damaging reactions between the reactive species and the emitter material. Hence, Brikner and Lozano propose an upstream ‘distal’ electrode, exclusively in contact with the ionic liquid that neutralize the newly generated ions on the emitter tip, to mitigate these reactions. They were able to demonstrate this principle, in the case of tungsten emitters, where the material showed far less degradation after firing versus a control where visible degradation was observed. They also propose an alternate solution, where electrochemical reactions can be minimized by ensuring that the voltage drop across the ionic liquid path between the emitter and the accelerating electrode is within the electrochemical stability window of the ionic liquid or using insulating emitter substrates, like porous borosilicate glass filters.

4.3.5 Determining the time to exhaust given volume of ionic liquid

To test the length of time before the ionic liquid is exhausted, ionic liquid was added in known increments to a patterned xerogel substrate tested with multiple input voltages, starting at 500 V_{DC} and if emissions/emission spikes observed, the input voltage was reduced in a step-wise manner until no emissions are seen. For each ionic liquid addition and input voltage change, the experiment was paused before the ionic liquid was added or voltage changed. As with other experiments a 2mA and 1W safety constraint was applied. It was observed that no emissions were observed even at the highest input voltages until 300 μL of ionic liquid ([EMIM][TFSI]) was added.

The emission test re-started with this quantity of ionic liquid at input voltage of 280 V_{DC}. Emissions were constant for the first hour at 300 μA. However, at 50 minutes, 'noise' or random ionic liquid emissions observed as large current spikes were observed. The current gradually dropped over the next 100 minutes, until the emissions reached 1 μA of current, at which point the experiment was paused. The input voltage was then increased to 450 V_{DC}. The experiment was then continued; over the next 8 hours, the emissions fluctuated in the 50-100 μA range. Even at the end of this time period, emissions continued and hence the experiment was halted after 10 hours for the purpose of this thesis (Figure 4.19).

The amount of ionic liquid is very high, considering the total charge expelled over the experiment time period. 300 μL is equivalent to 3.5×10^{20} C ([EMIM][TFSI] density is 1.52 g/cm^3 and molecular weight is 391.31 g/mol), from positive or negatively charged species, whereas the total charge expelled, considering an average current emission of 70μA is 2.52 C. Hence, in order to completely expel more charges, higher input voltages, only possible in a vacuum chamber without causing electrode arcing are required, whereas in ambient conditions, only voltages below the breakdown voltage of 500 V_{DC} is possible. This could indicate as long as emissions are in the ionic regime, this system can continue to provide propulsion for months; however, this assumption does not take into account substrate degradation, electrochemical breakdown of ionic liquid at the emitter tips, or inadvertent colloidal electrospray emission, which could cause the current to fluctuate. Further, complete ionic liquid exhaustion has not been explored at this time, due to the

large timescales involved, and hence, it is not possible to state if in fact the emissions can continue over the entire anticipated miniature-satellite mission time.

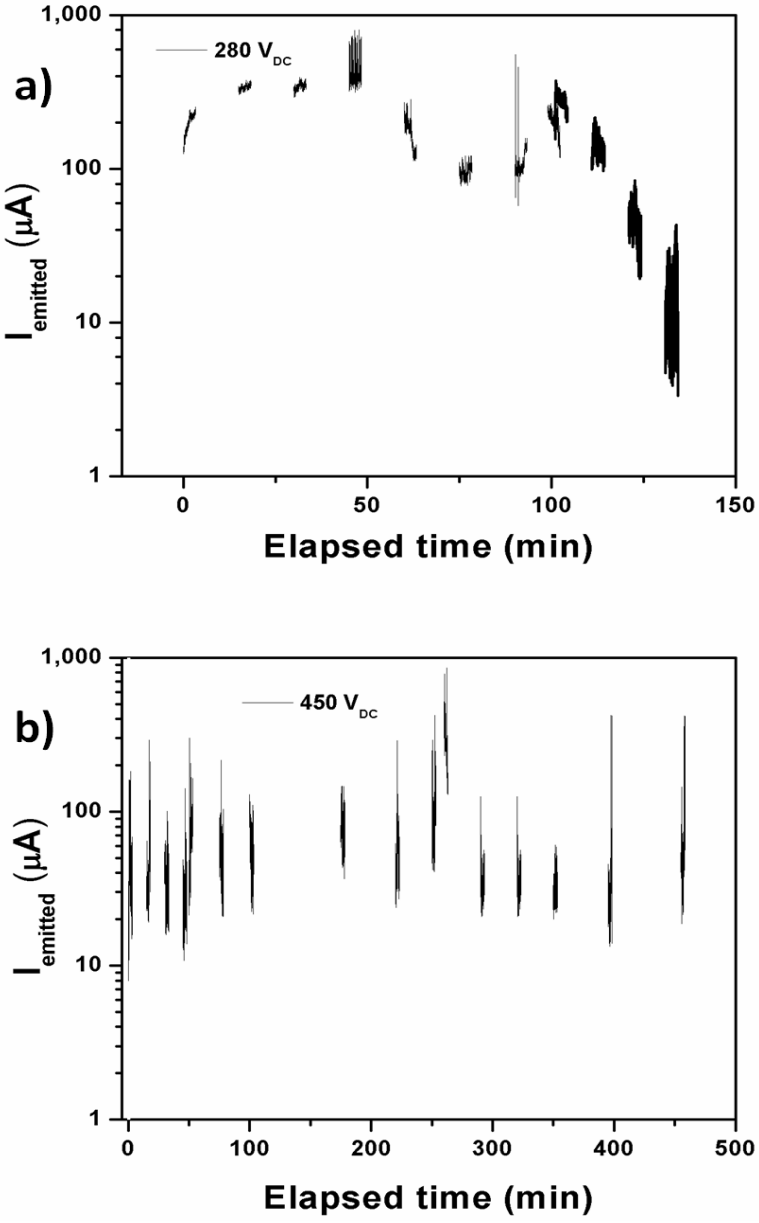

Figure 4.19 Summary of results for xerogel soaked with 300 μL [EMIM][TFSI] ionic liquid. The legend in each figure shows the input DC voltage

4.3.6 Voltage stepping

To determine the current emissions at different input voltages, another experiment was carried out with a patterned xerogel substrate soaked with approximately 1 mL ionic liquid. Unlike prior experiments, the emission testing was not paused and restarted between each voltage increment. The safety constraints on the input voltage were set to 2 mA and 1W. The input voltage source was programmed to increase from 250 V_{DC} to 450 V_{DC} in 8 steps of 10 minutes duration each, for a total of 80 minutes: the first step was 250 V_{DC}, the second at 280 V_{DC}, then 300 V_{DC}, 330 V_{DC}, 350 V_{DC}, 400 V_{DC}, 420 V_{DC}, and finally 450 V_{DC}. The program was repeated in three runs on the same xerogel, with no replenishment of ionic liquid in between runs. The results from the oscilloscope reading are presented in the section and raw data presented in the appendix 2 (Figure 4.20).

The current increases noticeably as the input voltage increases, as expected. For the first run, the emitted current is very low until 300 V_{DC}, increasing abruptly until 350 V_{DC}, then remaining constant or reducing slightly until 450 V_{DC}. For the second run, the emitted current is constant at ~10 µA until 300 V_{DC}, beyond which, it increases gradually with voltage ramping, which is the expected behaviour. In the third run, the emitted current increases with voltage ramping until 300 V_{DC}, where it takes a slight dip until 350 V_{DC}, before increasing gradually as the voltage is ramped to 450 V_{DC} (Figure 4.20).

The emitted current behaviour of the first attempt is anomalous to expected characteristics; one possible explanation is that the emitters on the xerogel surface are being ‘primed’ i.e. the ionic liquid is not available at the emitter surface and hence requires some time before these can be emitted, as seen from the very low current emissions up to 300 V_{DC} and the relatively wide current error bars compared to the second and third runs.

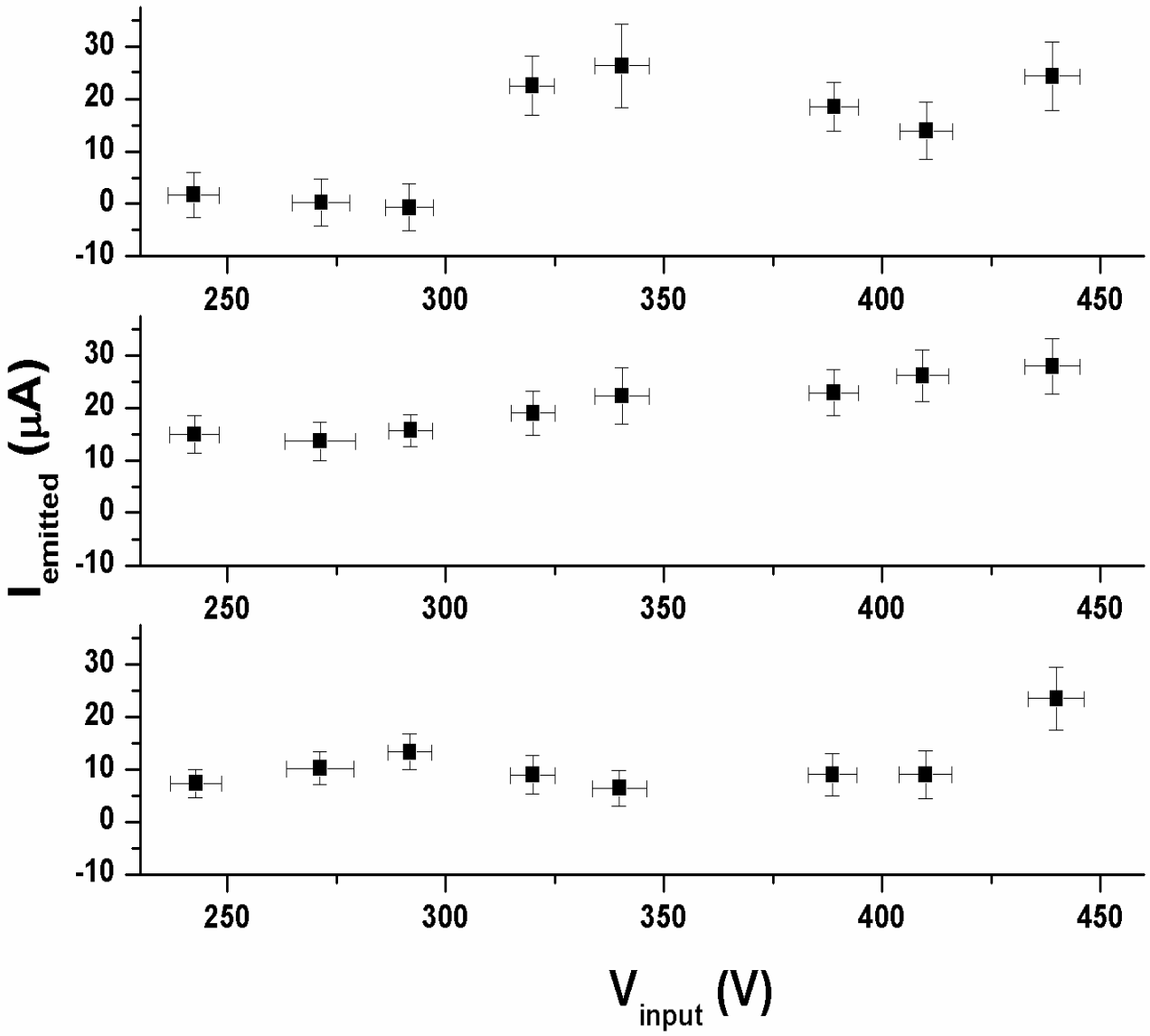

Figure 4.20 IV plots of voltage stepping. Each graph from top to bottom represents respectively the first, second and final runs, each of 80 min duration and performed successively. Data reported as mean ± standard deviation

CHAPTER 5 CONCLUSION AND RECOMMENDATIONS

The work presented in this thesis sought to create an electrospray ion emitter for a miniature-satellite propulsion system; finally, an automatic silicon-wafer dicing machine patterned a carbon xerogel with hundreds of emitter pillars with 150 μm high walls, spaced 250 μm apart. Xerogels were synthesized in the lab by pyrolyzing a resorcinol-formaldehyde gel. The porosity of the xerogel was analyzed with mercury intrusion porosimetry and visualized with SEM imaging; the material was determined to be macroporous. The SEM imaging reveals pores, bounded by scaffold-like carbon walls, which form a cage-like mesh. The 'skin' that results from the surface RF gel heating too quickly due to exposure to air or the mould was also visualized with SEM; it was not as porous as the xerogel bulk and hence must be polished off prior to processing the xerogel further.

Four different micro-patterning methods were examined:

1. Reactive ion etching with and without metal masking: this required 4 hours to etch trenches of 100-150 μm, no commercial resist tested could withstand this. Metal masking with e-beam deposited titanium was also attempted, however, due to the porous nature of the xerogel, the titanium deposited on the pores closest to the surface. Electrical testing was never carried out, as it is uncertain if the metal etchant that eliminates the metal which is optimized for monolithic substrates like glass, silicon and silicon dioxide, could completely remove any residual metal, especially any that deposited into the xerogel surface pores. SEM imaging of the regions where no metal was present revealed charging, high molecular weight material, probably titanium dioxide clinging to the xerogel pore walls.
2. Laser ablation with a green-spectrum femtosecond laser: this method was slow, requiring multiple passes over the ablated trench to achieve 30 μm depth, and as a side-effect fused the pores up which reduces the pore sizes to tens of nanometers, possibly affecting electrospray performance
3. Using an elastomer stamp to pre-pattern the RF gel prior to solidification and then pyrolysis into xerogel: this was unsuccessful because PDMS residues were hard to eliminate, especially from the micro-patterns. While this method preserved the material porosity after a short RIE process to eliminate the surface skin, comparing with the dicing method, this

does not lend any advantages considering the size of the features; in comparison, this method is far slower than dicing. Further development is required to exploit this method, especially with PDMS residue elimination.

4. Adapting an automatic dicing saw to cut trenches into the xerogel surface: in this method, an automatic dicing saw, which uses a blade impregnated with abrasive materials spinning at very high rotation speed which permits cuts in brittle materials like xerogels, and a stage with very accurate stepping motors cumulatively allows repeatability between substrates, cut pillars with 150 μm high walls and spaced 250 μm apart. This method preserves the material porosity, due to the low heat transfer between the blade and the substrate

Hence, the dicing saw was chosen to pattern xerogels. The patterned xerogels, soaked with [EMIM][TFSI] ionic liquid, were subjected to electrical tests to demonstrate electrospray. Initially a bare copper plate was the accelerating electrode and designated as Xerogel Setup A, this was abandoned due to the unstable current emission. A second approach using an unpatterned xerogel with no ionic liquid as the accelerating electrode was adopted and designated as Xerogel Setup B, the current emission was much more stable with lesser ‘noise’ or current emission spikes, which come from ionic liquid hitting the liquid at a higher velocity than the rest of the emitting species. The emission spikes in both tests were compared to emission testing performed on a bare xerogel with no ionic liquid, air breakdown arcs are spikes in the mA range, whereas emission spikes are always in the μA range. Further experiments revealed the presence of electrochemical degradation products on the emitter peaks seen as bright charging regions in the LABE detector in the SEM, the difficulty in testing the charge emitted by a given quantity of ionic liquid in the substrate in ambient air due to limitations in continuing the experiment at higher voltages due to air breakdown, and the increase in current emissions as the input voltage is gradually stepped up.

This work has developed a mask-less, single-step and rapid microfabrication method to pattern both emitter pillars and cones on carbon xerogel surfaces without damaging the pores or changing the chemical makeup. While this is a step toward creating a practical electrospray ion thruster, further work is required:

- Emission testing at input voltages of 800-1200 V_{DC}, is required to measure the total thrust provided by a given quantity of ionic liquid in the xerogel. Endurance testing to determine the durability of the xerogels must also be carried out using expected operating input voltages This is only possible under vacuum, where the possibility of air breakdown arcs is reduced
- Time of Flight spectrometry must be carried out on the emitted electrospray species to determine the composition of these. This is extremely important to optimize the input voltages to obtain the electrospray regime desired, i.e. colloid or ionic.
- To eliminate charge accumulation, the input voltage polarity must be alternated, and emission characteristics obtained.
- Electrochemical breakdown of the ionic liquid must be investigated in greater detail. Degradation of the emitter tips as a result of the electrochemical reactions or their by-products, and the effect of an upstream distal electrode to reduce electrochemical breakdown must be explored systematically.[18]
- The carbon xerogel must be incorporated into a working device, where the device housing encapsulates the ionic liquid-soaked xerogel whose emitter tips are aligned with the openings in a 100 μm thick metal grate which acts as an accelerating electrode, which suspended above an ionic liquid reservoir. The emission characteristics of multiple devices must be tested, prior to space qualification, before the device is ready to be used in the propulsion system.

REFERENCES

[1] I. Levchenko, S. Xu, G. Teel, D. Mariotti, M. L. R. Walker, and M. Keidar, "Recent progress and perspectives of space electric propulsion systems based on smart nanomaterials," *Nat. Commun.*, vol. 9, no. 1, 2018.

[2] Canadian Space Agency, "What is a CubeSat?," 2018.

[3] Canadian Space Agency, "What is a CubeSat?," 2018.

[4] K. Lemmer, "Propulsion for CubeSats," *Acta Astronaut.*, vol. 134, no. September 2016, pp. 231–243, 2017.

[5] D. G. Courtney, "Ionic Liquid Ion Source Emitter Arrays Fabricated on Bulk Porous Substrates for Spacecraft Propulsion," PhD Dissertation, MIT, 2011.

[6] D. Krejci and P. Lozano, "Space Propulsion Technology for Small Spacecraft," *Proc. IEEE*, vol. 106, no. 3, pp. 362–378, 2018.

[7] D. R. Lev, J. Herscovitz, D. Kariv, and I. Mizrachi, "Cold Gas Propulsion System Conceptual Design for the SAMSON NanoSatellite," *J. Small Satell.*, vol. 6, no. 1, pp. 551–564, 2017.

[8] A. R. Tummala, "An Overview of Cube-Satellite Propulsion Technologies and Trends," *Aerospace*, vol. 4, no. 4, p. 58, 2017.

[9] D. T. Schmuland, R. K. Masse, and C. G. Sota, "Hydrazine Propulsion Module for CubeSats," *25th Annu. AIAA/USU Conf. Small Satell.*, 2011.

[10] K. L. Zhang, S. K. Chou, and S. S. Ang, "Development of a solid propellant microthruster with chamber and nozzle etched on a wafer surface," *J. Micromechanics Microengineering*, vol. 14, no. 6, pp. 785–792, 2004.

[11] D. Krejci, F. Mier-Hicks, R. Thomas, T. Haag, and P. Lozano, "Emission Characteristics of Passively Fed Electrospray Microthrusters with Propellant Reservoirs," *J. Spacecr. Rockets*, vol. 54, no. 2, pp. 447–458, Mar. 2017.

[12] National Aeronautics and Space Agency, "Iodine Satellite," *NASA Facts*, 2015.

[13] Busek, "BHT-200 System Technical Specifications," 2019.

[14] D. Krejci, “Electrospray thruster engineering,” 2016. [Online]. Available: http://spl.mit.edu/electrospray-thruster-engineering.

[15] Tethers Unlimited, “Electrodynamic Tethers.” [Online]. Available: http://www.tethers.com/EDTethers.html.

[16] M. Nohmi, “Initial Orbital Performance Result of Nano-Satellite STARS-II.”

[17] J. Zeleny, “The electrical discharge from liquid points, and a hydrostatic method of measuring the electric intensity at their surfaces,” *Phys. Rev.*, vol. 3, no. 2, pp. 69–91, 1914.

[18] I. E. Jivanescu, “Structure and Performance of Carbon Xerogel Molded Emitters for Micropropulsion Applications,” Masters thesis, MIT, 2016.

[19] K. Nakagawa, T. Tsuchiya, and Y. Takao, “Microfabricated emitter array for an ionic liquid electrospray thruster,” *Jpn. J. Appl. Phys.*, vol. 56, no. 6, 2017.

[20] T. Henning, K. Huhn, L. W. Isberner, and P. J. Klar, “Miniaturized Electrospray Thrusters,” pp. 1–5, 2017.

[21] D. G. Courtney, S. Dandavino, and H. R. Shea, “Comparing Direct and Indirect Thrust Measurements from Passively Fed and Highly Ionic Electrospray Thrusters,” *J. Propuls. Power*, vol. 32, no. 2, pp. 392–407, 2015.

[22] Accion Systems, “Ion Electrospray Propulsion,” 2018.

[23] J. Rojas-Herrera, I. Jivanescu, D. Freeman, D. Krejci, C. Fucetola, and P. Lozano, “Porous materials for ion-electrospray spacecraft microengines,” *J. Nanomechanics Micromechanics*, vol. 7, no. 3, pp. 2015–2018, 2017.

[24] Internation Union of Pure and Applied Chemistry, “Gel definition,” *IUPAC Gold B.*

[25] R. Brandt, R. Petricevic, H. Pröbstle, and J. Fricke, “Acetic Acid Catalyzed Carbon Aerogels,” *J. Porous Mater.*, vol. 10, no. 3, pp. 171–178, 2003.

[26] A. M. Elkhatat and S. A. Al-Muhtaseb, “Advances in tailoring resorcinol-formaldehyde organic and carbon gels,” *Adv. Mater.*, vol. 23, no. 26, pp. 2887–2903, 2011.

[27] B. S. a Al-muhtaseb and J. a Ritter, “Preparation and Properties of Resorcinol ± Formaldehyde Organic and Carbon Gels **,” *Adv. Mater.*, no. 2, pp. 101–114, 2003.

[28] S. Mulik, C. Sotiriou-leventis, and N. Leventis, “Time-Efficient Acid-Catalyzed Synthesis of Resorcinol - Formaldehyde Aerogels,” *Chem. Mater.*, vol. 19, no. 1, pp. 6138–6144, 2007.

[29] M. Lawrence and Y. Jiang, *Bio-aggregate-based Building Materials*. 2013.

[30] P. A. Webb, “An Introduction To The Physical Characterization of Materials by Mercury,” *Micromeritics Instrum. Corp.*, no. January, p. 23, 2001.

[31] C. S. Sharma, A. Verma, M. M. Kulkarni, D. K. Upadhyay, and A. Sharma, “Microfabrication of carbon structures by pattern miniaturization in resorcinol-formaldehyde gel,” *ACS Appl. Mater. Interfaces*, vol. 2, no. 8, pp. 2193–2197, 2010.

[32] R. Bhandari, S. Negi, L. Rieth, R. A. Normann, and F. Solzbacher, “A novel method of fabricating convoluted shaped electrode arrays for neural and retinal prosthesis,” *TRANSDUCERS EUROSENSORS ’07 - 4th Int. Conf. Solid-State Sensors, Actuators Microsystems*, vol. 146, pp. 1231–1234, 2007.

[33] C. S. Schwandt, “Characterizing nanometer-scale materials using a low-angle backscattered electron detector,” *American Laboratory*, vol. 42, no. 11. pp. 13–17, 2010.

[34] R. Dahiya, G. Gottardi, and N. Laidani, “PDMS residues-free micro/macrostructures on flexible substrates,” *Microelectron. Eng.*, vol. 136, no. October 2012, pp. 57–62, 2015.

[35] N. Brikner and P. C. Lozano, “The role of upstream distal electrodes in mitigating electrochemical degradation of ionic liquid ion sources,” *Appl. Phys. Lett.*, vol. 101, no. 19, 2012.

APPENDIX A EMISSION CHARACTERISTICS

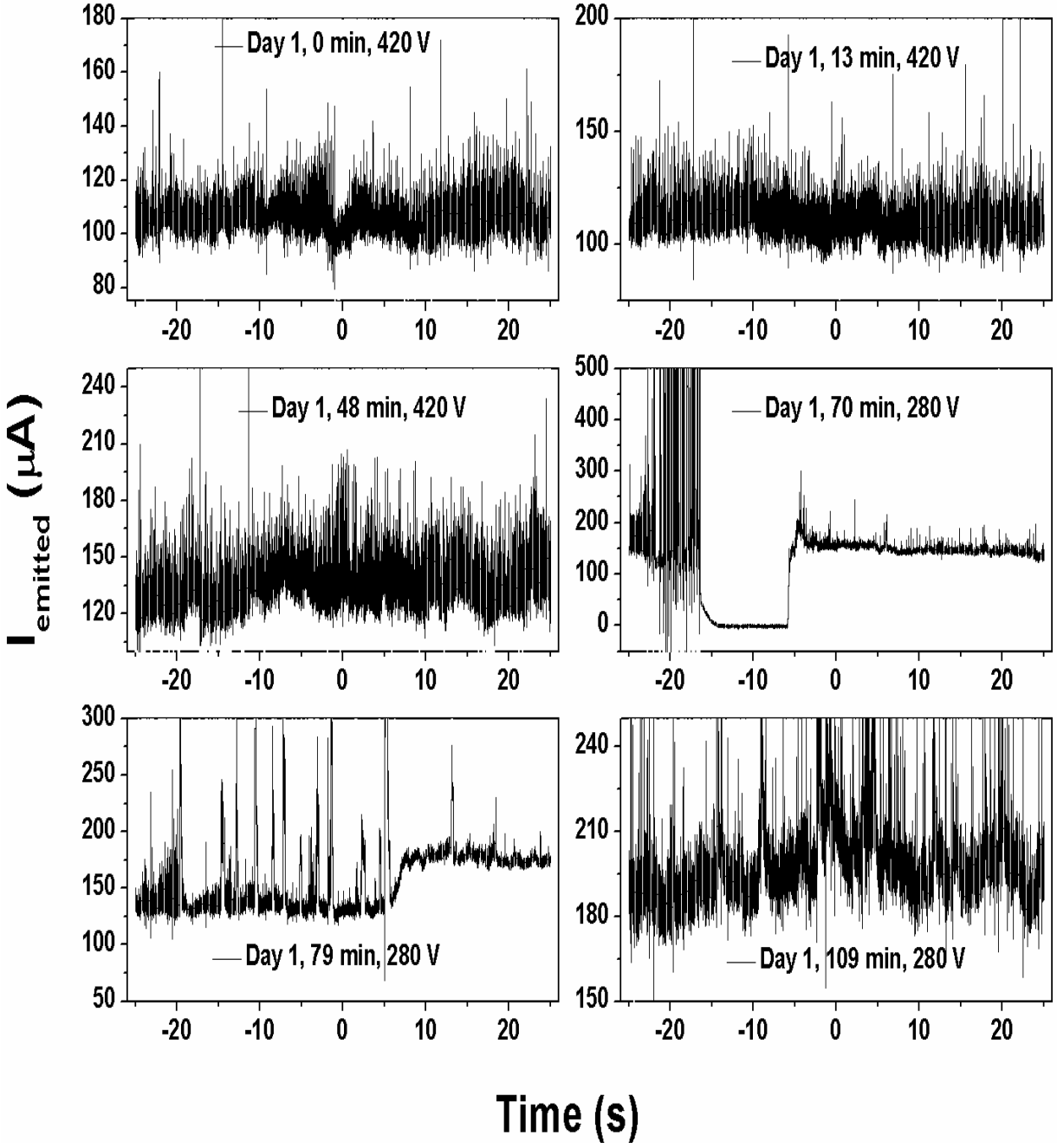

Appendix Figure 1 2-D emission characteristics day 1, the legend in each figure shows the day, time in minutes and input DC voltage

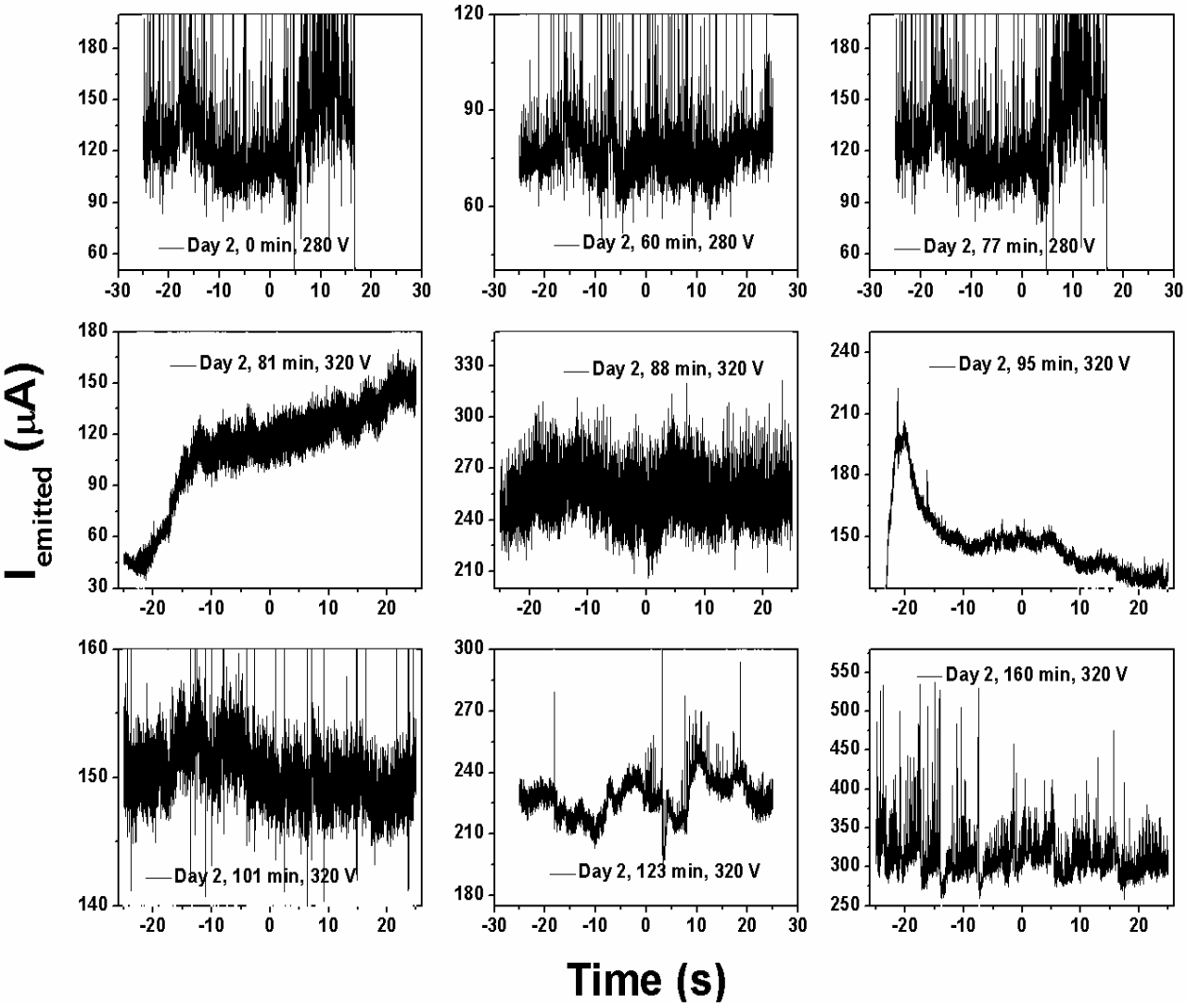

Appendix Figure 2 2-D emission characteristics days 2, the legend in each figure shows the day, time in minutes and input DC voltage

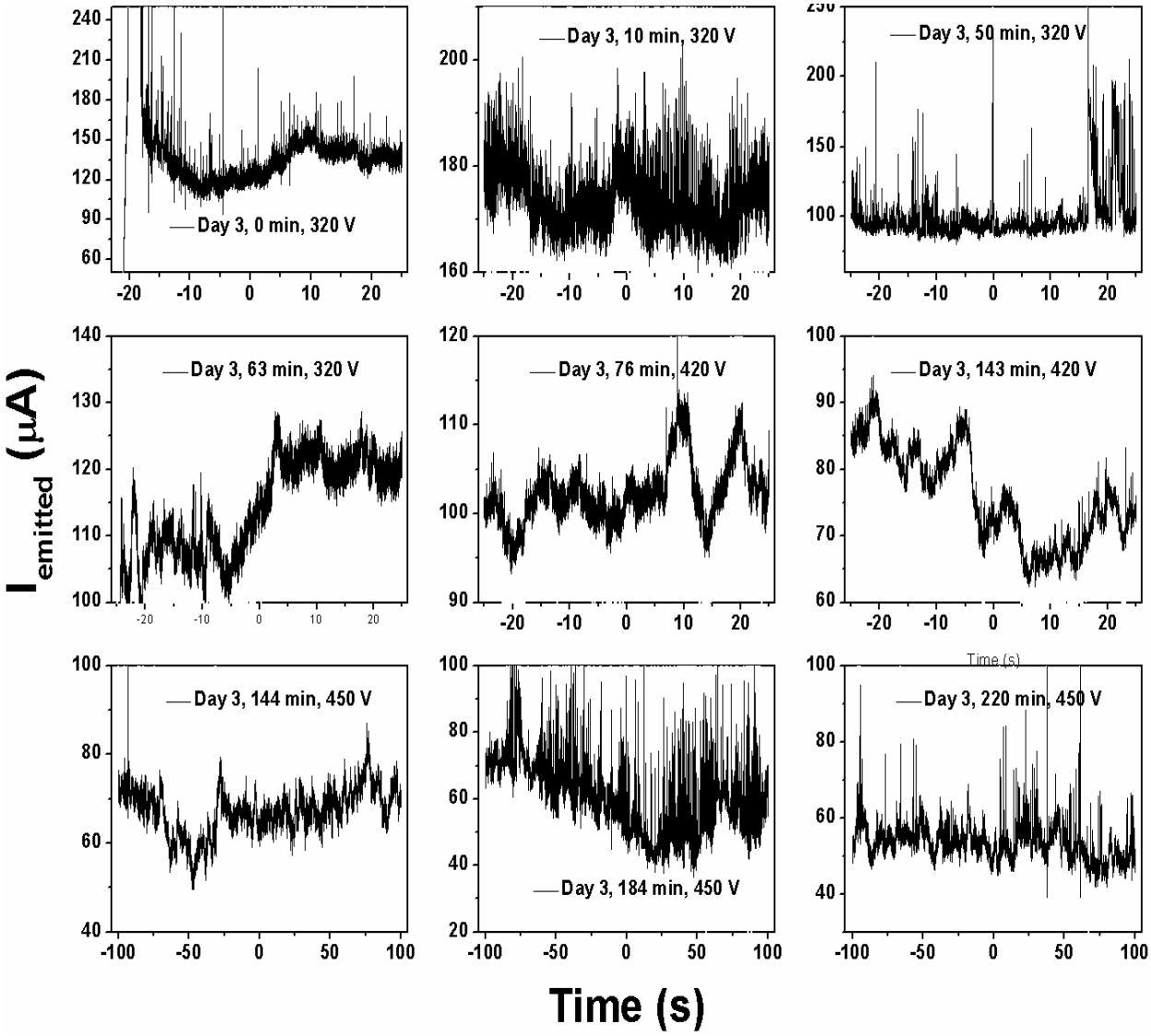

Appendix Figure 3 2-D emission characteristics day 3, the legend in each figure shows the day, time in minutes and input DC voltage

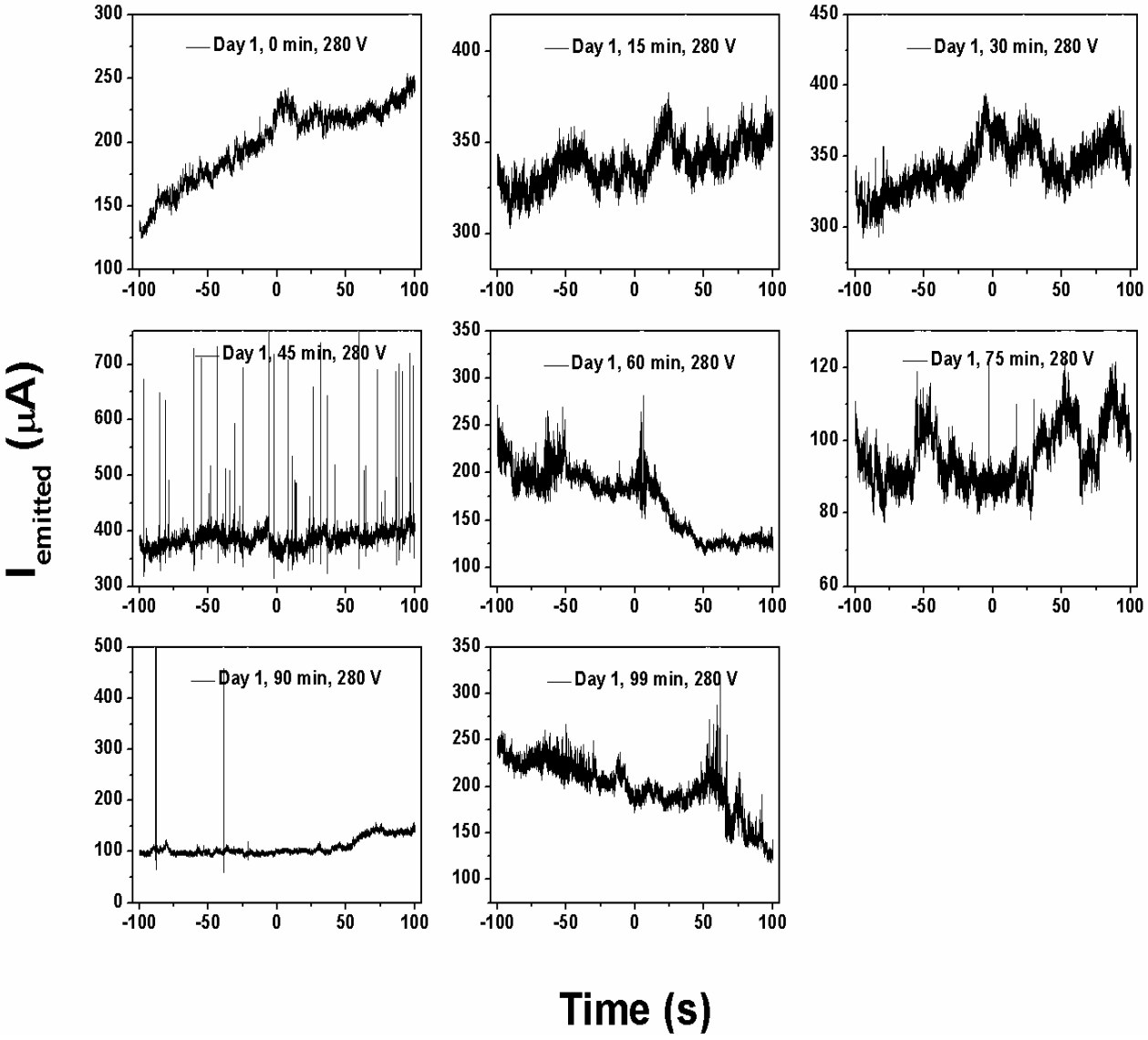

Appendix Figure 4 Limited ionic liquid oscilloscope scans Day 1, the legend in each figure shows the day, time in minutes and input DC voltage

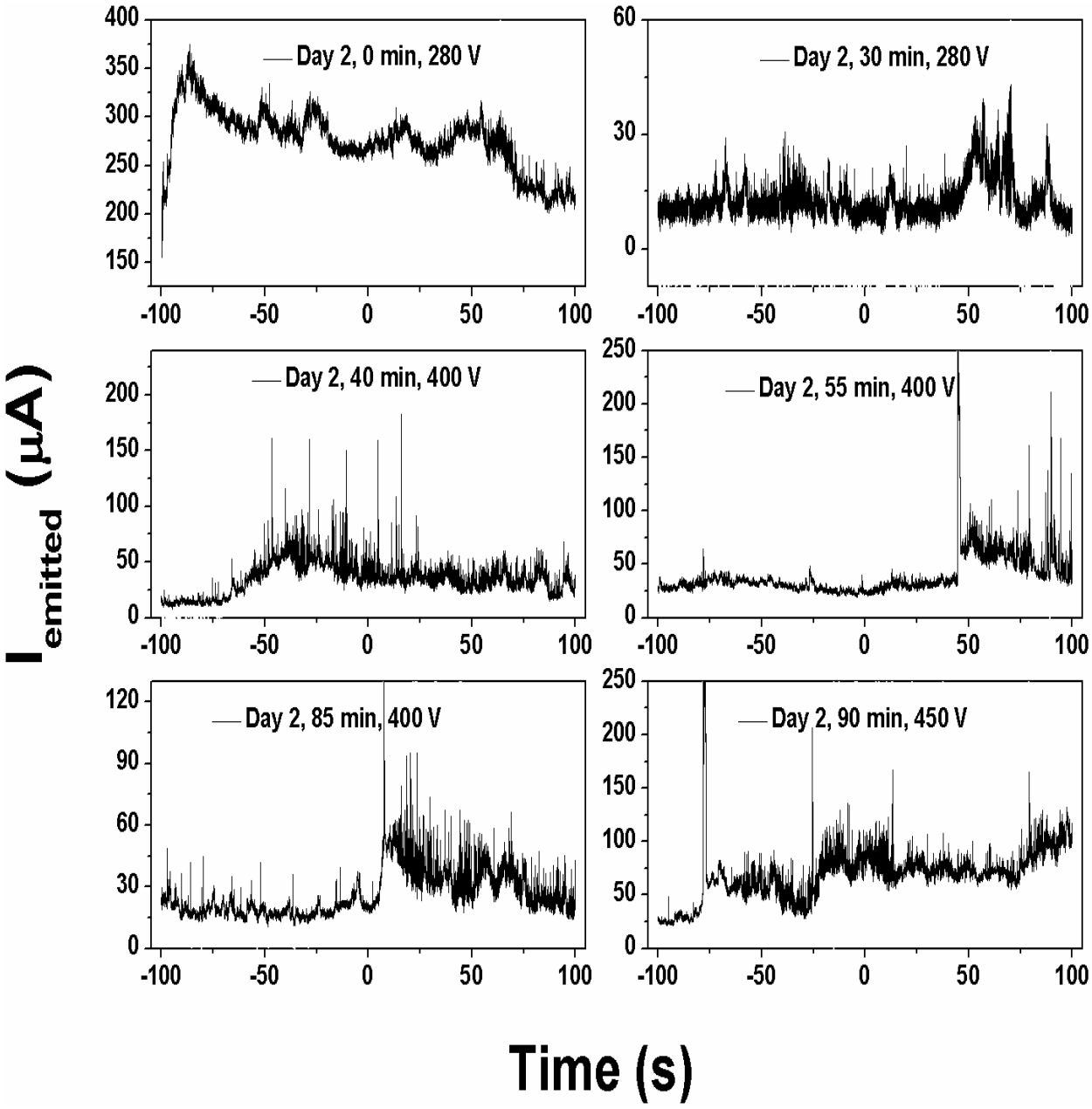

Appendix Figure 5 Limited ionic liquid oscilloscope scans Day 2, the legend in each figure shows the day, time in minutes and input DC voltage

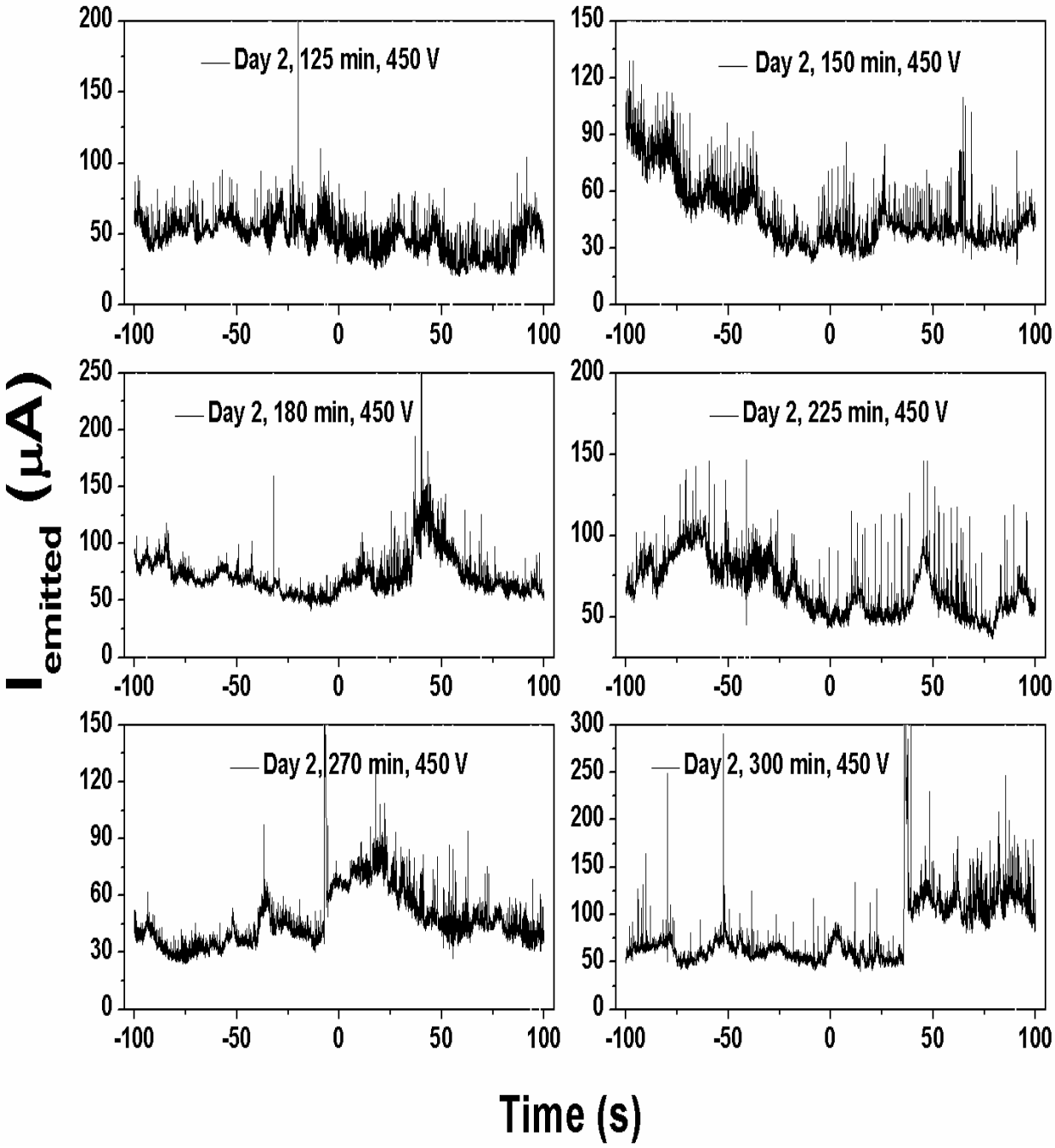

Appendix Figure 6 Limited ionic liquid oscilloscope scans Day 2 contd., the legend in each figure shows the day, time in minutes and input DC voltage

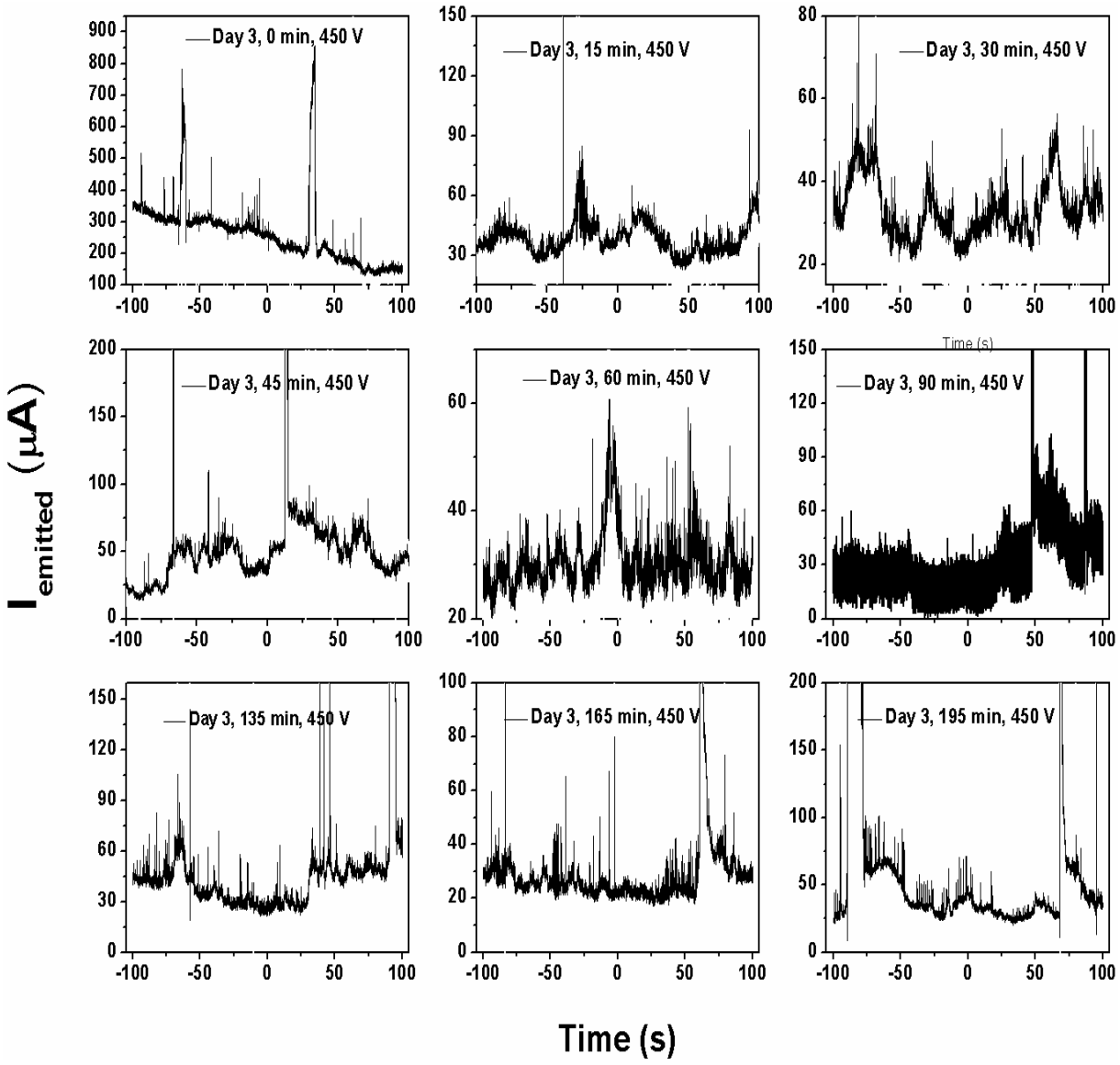

Appendix Figure 7 Limited ionic liquid oscilloscope scans Day 3, the legend in each figure shows the day, time in minutes and input DC voltage

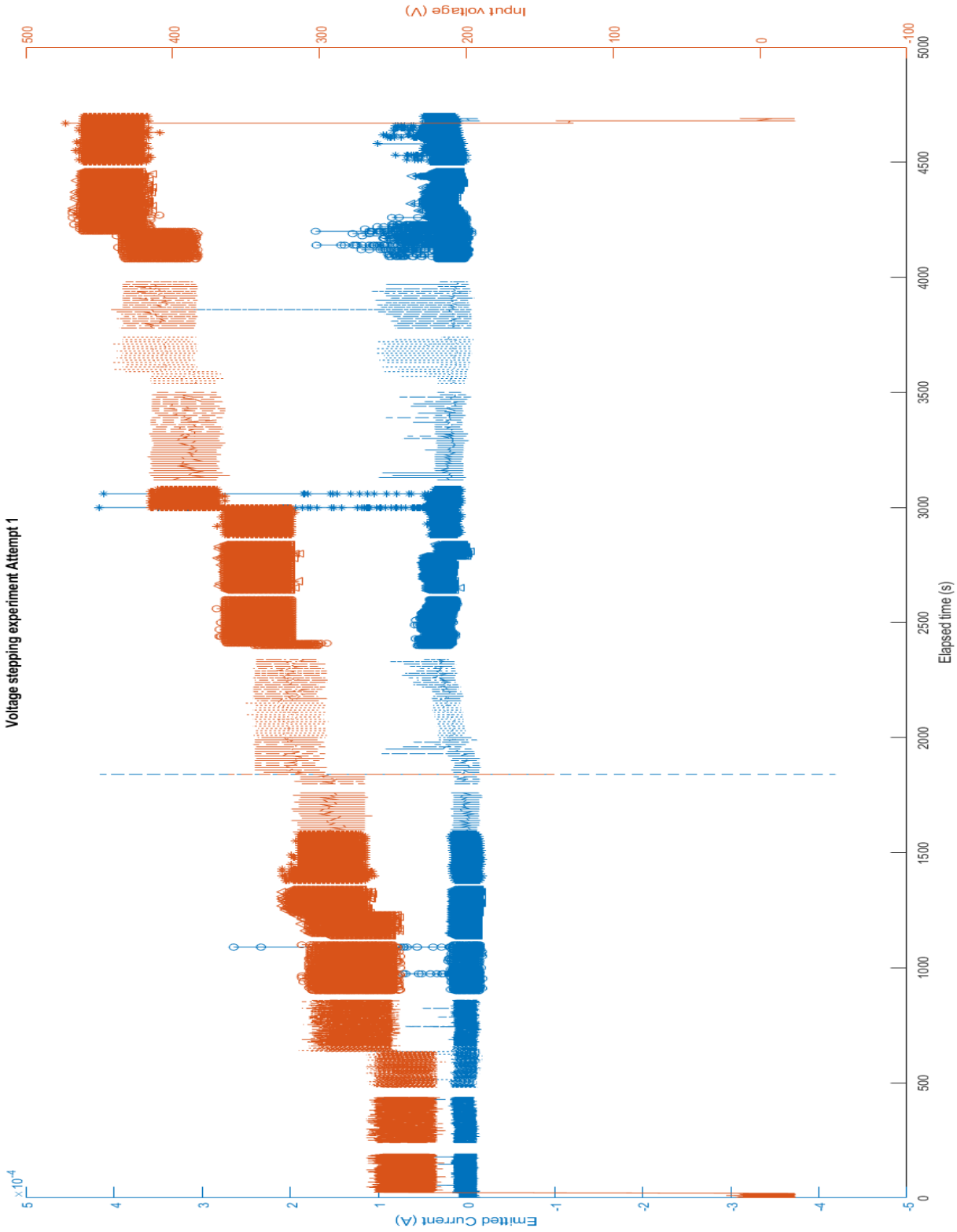

Appendix Figure 8 Raw data for voltage stepping first run

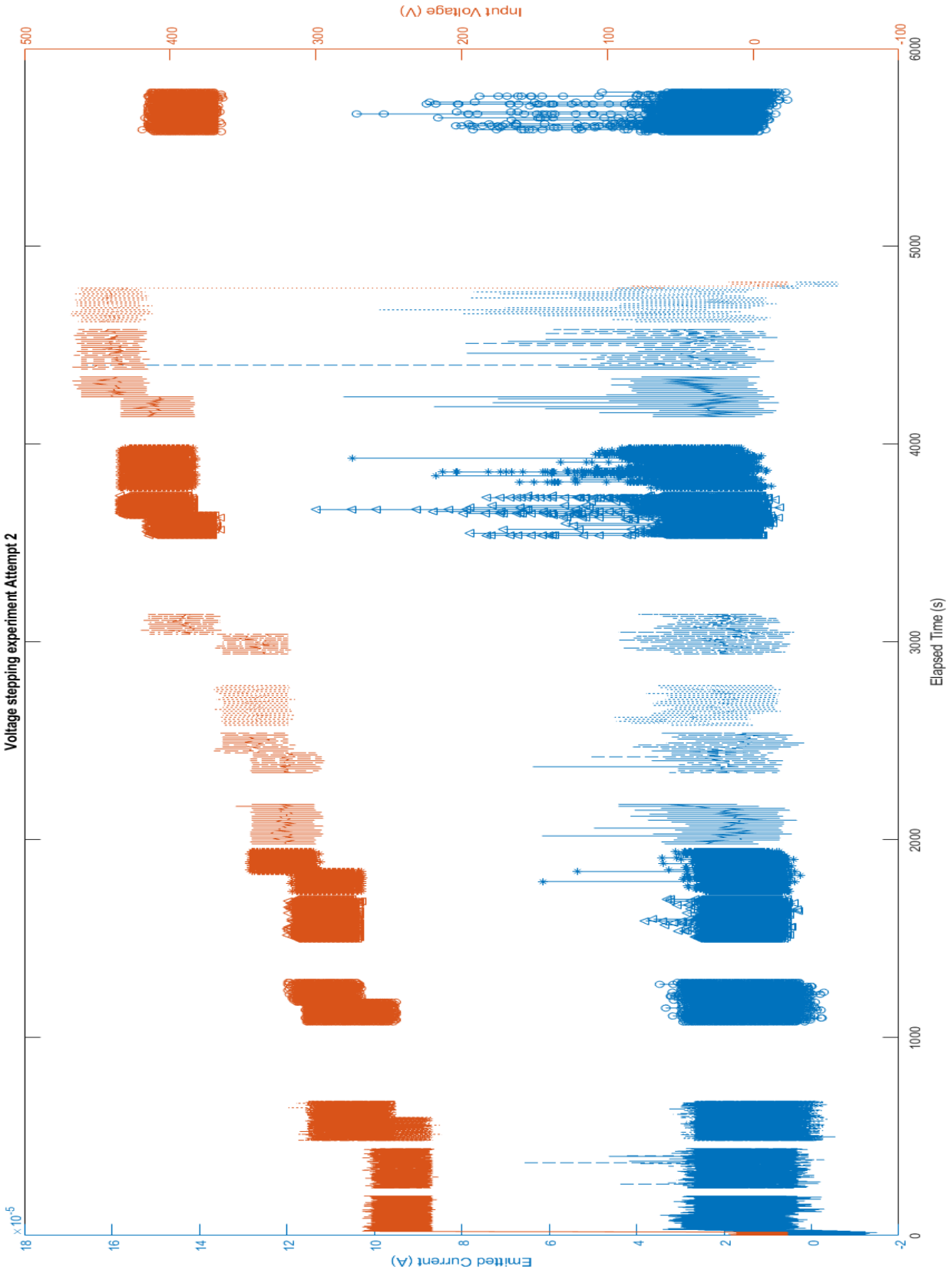

Appendix Figure 9 Raw data for voltage stepping second run

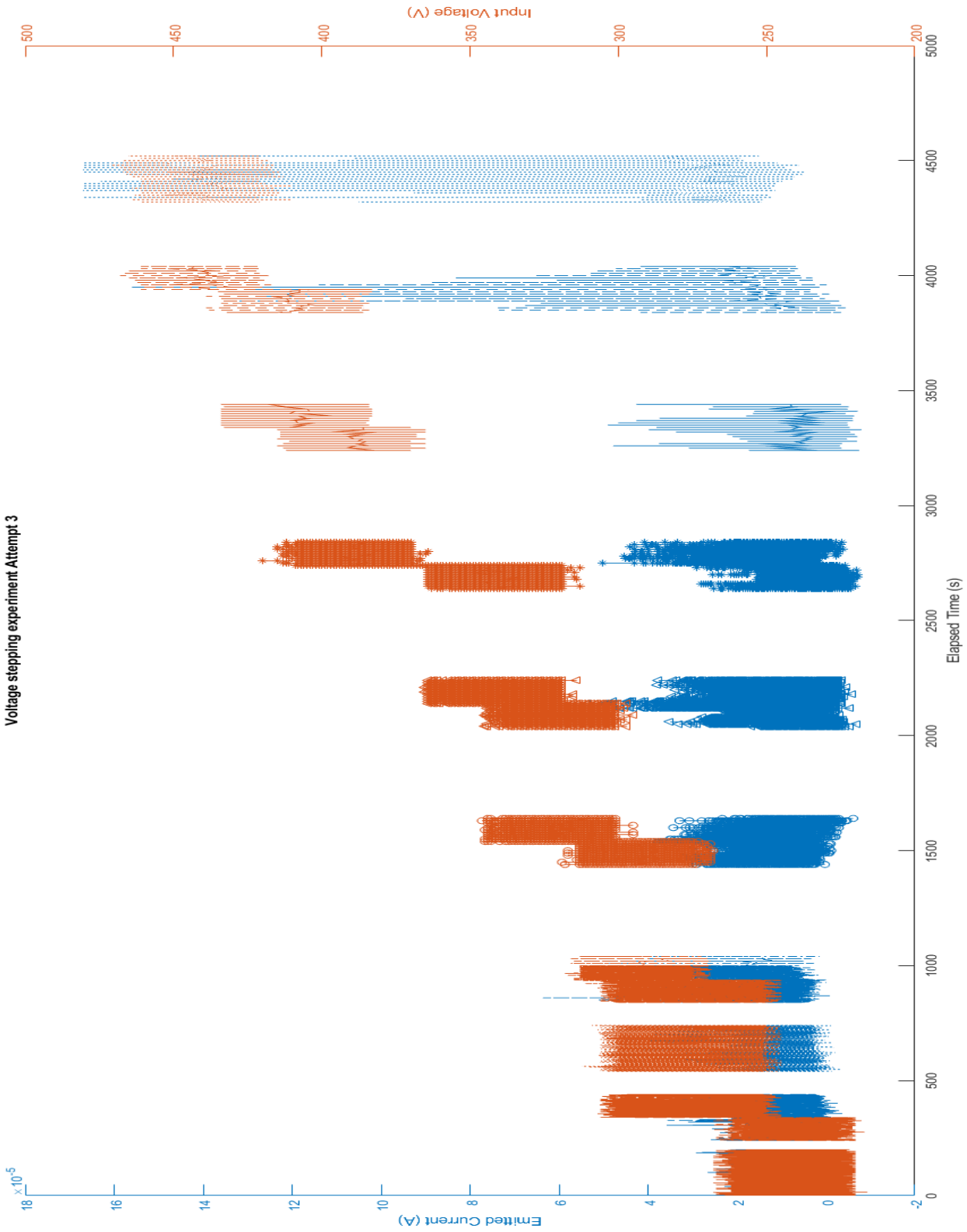

Appendix Figure 10 Raw data for voltage stepping third run

APPENDIX B SEM IMAGES

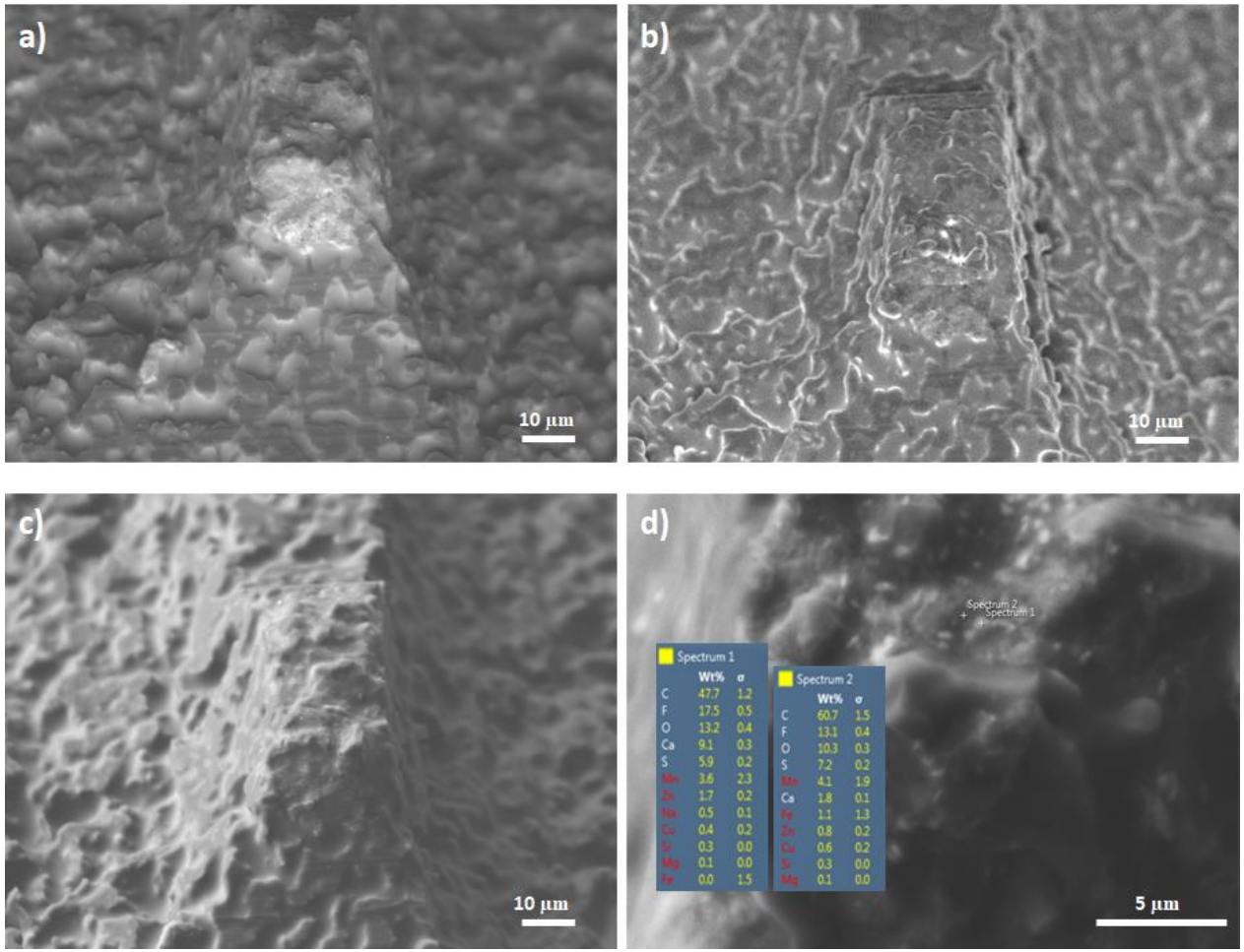

Appendix Figure 11 2-D patterned post-emission SEM, site 2 a) LABE detector (scale bar 10 µm) b) SEI detector (scale bar 10 µm) c) topographical image with LEI detector (scale bar 10 µm) d) EDS chemical analysis (scale bar 5 µm)

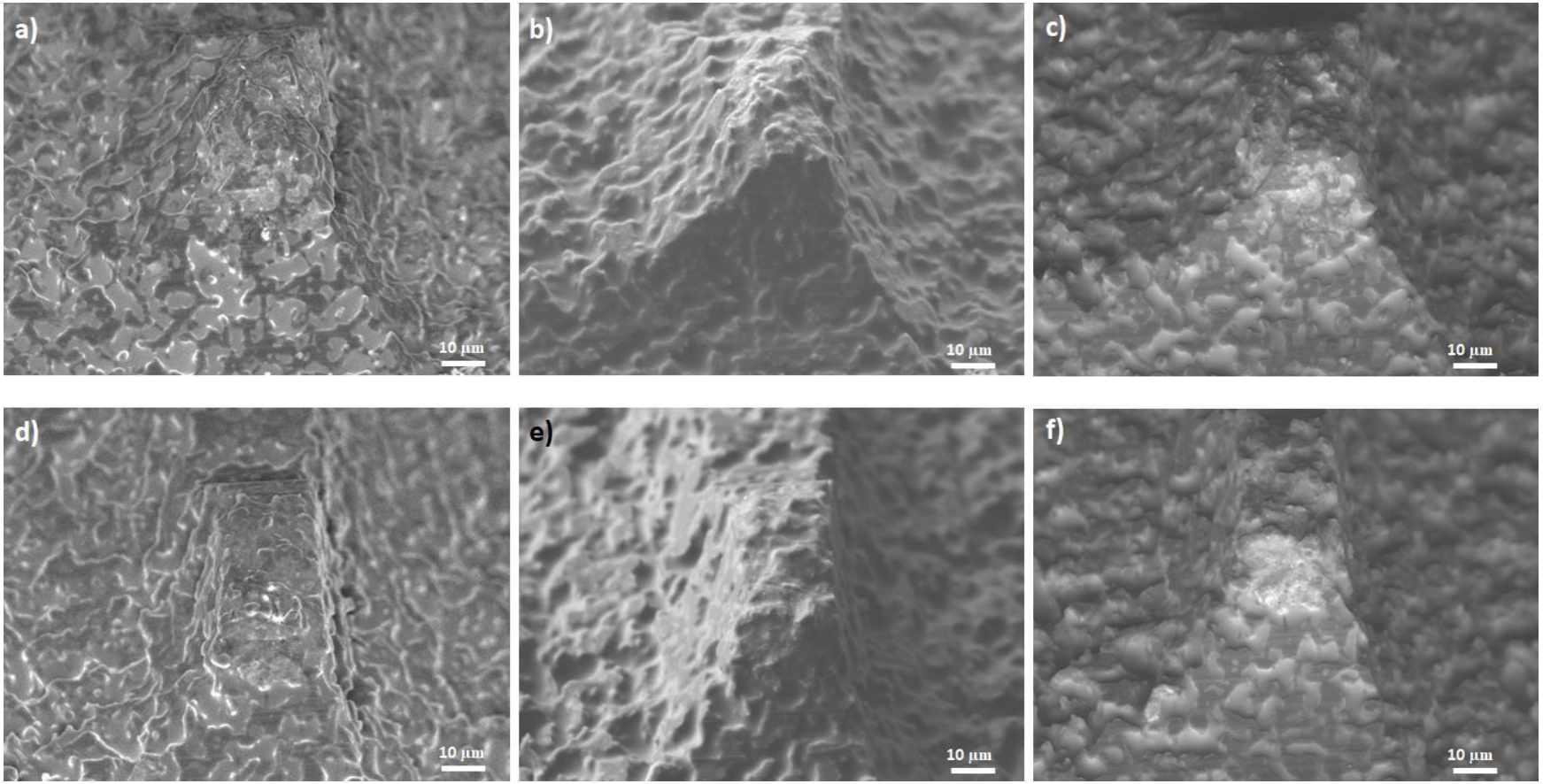

Appendix Figure 12 SEM images of two emitter tips created by 2-D patterning post-emission a), b) and c) are images of the first tip and d), e) and f) are images of the second tip taken with 3 separate detectors; a), d) are SEI images b), e) are LEI topographical images, and c), f) are LABE images